SU-SEL-68-005

Lunar Radar Scattering At 6 And 12 Meter Wavelengths

by
Alan A. Burns

May 1968

Scientific Report No. 25

Prepared under
National Aeronautics and Space
Administration
Grant NsG-377

RADIOSCIENCE LABORATORY
STANFORD ELECTRONICS LABORATORIES
STANFORD UNIVERSITY · STANFORD, CALIFORNIA

SEL-68-005

LUNAR RADAR SCATTERING AT 6 AND 12 METER WAVELENGTHS

by

Alan A. Burns

May 1968

Scientific Report No. 25

Prepared under

National Aeronautics and Space Administration

Grant NsG-377

Radioscience Laboratory

Stanford Electronics Laboratories

Stanford University Stanford, California

PRECEDING PAGE BLANK NOT FILMED.

ABSTRACT

Radar echoes of the moon at wavelengths of 6 and 12 m are analyzed to obtain more knowledge about the scattering properties of the lunar surface. The delay spectra, or reflected power vs range curve, are measured at both wavelengths. At 12 m, the ratio of the expected (i.e., in the same direction as transmitted polarization) linearly polarized component to the depolarized (perpendicular to the transmitted) component is also measured. The range resolution used for these observations was about 20 μs, making the results directly comparable to those from other observations at much shorter wavelengths. This resolution is about an order of magnitude better than that previously obtained at the long wavelengths.

Linear FM pulse compression was used to obtain high range resolution and sensitivity; the bandwidth and duration of the transmitted signal were 100 kHz and 1 sec, respectively. The influences of the ionosphere on this signal are studied, and the Faraday effect, which is the most important here, is shown to modulate the echoes sinusoidally. It is demonstrated that the total Faraday rotation is proportional to the modulation frequency, and that the frequency can be measured directly from the echoes.

The effect of this modulation on the data analysis, which is mainly digital spectral analysis, is expressed in terms of the frequency and phase of the modulation. Since those quantities can be measured from the data, one can then compensate for the Faraday effect. A method for simultaneously compensating for the Faraday effect and estimating the expected and depolarized echo components is presented.

The final results show that the lunar backscattering is nearly independent of wavelength for wavelengths greater than 68 cm. No significant difference could be seen between the 68 cm and 6 m results over the entire 11.6 ms range depth of the moon. Sensitivity limitations precluded making measurements at 12 m over the full lunar range depth, but the 6 and 12 m results were identical over the observable first 6 ms. This hitherto unsuspected result is explained by the sensitivity of the leading edge of the echoes to the position of the subradar point, which varies due to lunar libration. The high resolution measurements

made here on two different days when the subradar points were well separated showed a 5 dB difference in the strength of the leading edge echoes at both wavelengths. When results at different wavelengths but with subradar points near one another are compared, they are found to match very closely.

CONTENTS

TABLES

ILLUSTRATIONS

ILLUSTRATIONS (cont)

ILLUSTRATIONS (cont)

ACKNOWLEDGMENT

I would like to express my appreciation to Professor Allen M. Peterson, the principal adviser for this research, for his patience and encouragement. Thanks are also extended to Professors Bruce B. Lusignan and Von R. Eshleman for their advice on several occasions. Similarly appreciated is the assistance of Mr. H. Taylor Howard, who directed the data collecting part of this work, and Drs. John E. Ohlson, Robert Nowak, and G. Leonard Tyler, with whom many profitable discussions were held.

Chapter I

INTRODUCTION

A. Background and Aims of This Study

Measurements of the moon's radio scattering properties have been made many times since the first radar detections were accomplished in 1946 [Bay, 1946; De Witt and Stodola, 1949]. The moon has also been used often as a passive reflector of radio signals for measuring the characteristics of the ionosphere and the ionized regions beyond it ever since Browne et al [1956] showed that the columnar electron content in the ionosphere could be obtained by measuring the Faraday rotation of the signals. The measurements presented here are actually the by-product of a study concerned with measuring the cislunar electron content using the moon as a passive reflector.

The previous lunar radar work is well summarized in several articles [Evans, 1962; Evans and Pettengill, 1963; Evans, 1965]. Much of it, particularly the early work, is mainly qualitative, with only the total radar cross section being measured. This was mainly due to equipment limitations, which sometimes required pulse lengths much longer than the 11.6 ms range depth of the moon for adequate received energy. Although 1 ms pulses were used fairly early [Kerr and Shain, 1951], and 12 μs pulses somewhat later [Trexler, 1958], the first really quantitative measurements of echo power vs range are more recent [Pettengill, 1958)].

The purpose of this work is to measure the short-pulse backscattering behavior of the moon at the long wavelength end of the spectrum with a range resolution equal to that of the shorter wavelength studies. Table 1 lists the quantitative short-pulse studies and shows the relationship of this study to the previous work.

The rapid fading of the long-pulse and CW echoes was attributed to the apparent rotation of the moon, or libration [Kerr, Shain, and Higgins, 1949], although the slow fading was not correctly identified as being caused by the Faraday effect until later [Murray and Hargreaves, 1954]. Since then, circular polarization has often been used to overcome this

Table 1

QUANTITATIVE SHORT-PULSE RADAR STUDIES OF THE MOON

Wavelength	Reference	Approximate Range Resolutions (μs)	Polarization	Range Interval Observed (ms)	Depolarized Component Studies?
3.6 cm	Evans & Pettengill [1963]	50	Linear	0 - 10	No
10 cm	Hughes [1961]	25	Linear	0 - 0.4	No
23 cm	Evans & Hagfors [1966]	Many, from 20 to 1000	Circular and Linear	0 - 11.6	Yes
68 cm	Evans & Pettengill [1963]	Many, from 22 to 300	Circular	0 - 11.6	Yes
6 m	Klemperer [1965]	100	Circular	0 - 11.6	No
6 m	This study	20,200	Linear	0 - 6	Yes
11.3 m	Davis & Rohlfs [1964]	250	Linear	0.4	No
12 m	This study	22,200	Linear	0.6	Yes

effect. The libration causes the reflected signals from different parts of the lunar surface to have different doppler shifts. The projected contours of constant frequency shift are parallel to the libration axis and the shift is proportional to the projected distance from the axis [Browne et al, 1956]. Figure 1 illustrates these contours plus those of constant range delay. Thus spectral analysis of a CW or a long-pulse

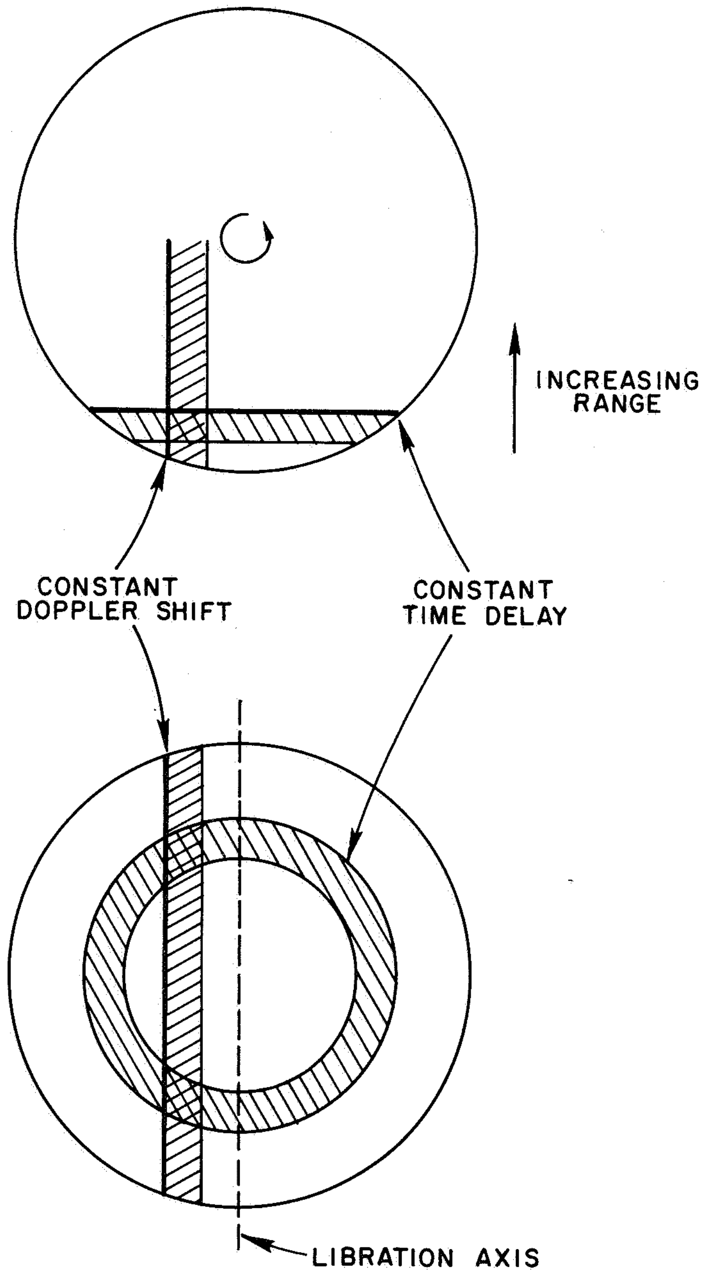

Fig. 1. CONTOURS OF CONSTANT TIME DELAY AND CONSTANT DOPPLER SHIFT.

echo would give one measure of the distribution of scatterers. Use of a train of coherent pulses allows range and doppler resolution, so that the resolved area is the two intersections of the bands of Fig. 1 [Pettengill, 1958]. The use of narrowbeam antennas can remove the ambiguity [Thompson and Dyce, 1966].

The autocorrelation function of the echoes has been measured and shown to be directly related to the libration rate, and the correlations between the signals from spaced antennas and between closely spaced frequencies have also been computed [Evans, 1957]. All these methods give information about the scattering behavior of the moon, and therefore presumably about the physical nature of the lunar surface. The problem of the relationship of the surface to the scattering behavior has not yet been entirely solved although much theoretical work has been done. The short-pulse and the simultaneous range-doppler resolution methods have yielded better measurements than the CW methods, the former giving an easily interpreted average angular backscattering law and the latter allowing a high-resolution radar map of the surface.

Several of the planets, mainly Venus, have been detected and studied by radar [Eshleman, 1967], and the study of the radio reflecting properties of the moon helps in understanding echoes from other rough bodies. Since close range photographs have been made of the lunar surface, the exploration program's needs for information about it (such as rms slopes) are no longer urgent, but the general rough surface radio scattering problem remains. Actually, the capability to compare the lunar surface to its scattering properties is useful, and present and future measurements on the surface will resolve some of the current difficulties in interpreting the scattering results.

No earth-based radar measurement can completely specify the scattering behavior since only the backscatter situation--where the angle of incidence is equal to the angle of reflection--is really available for study. However, the backscatter situation is more tractable mathematically for the theoretical studies, so comparisons between theory and experiment are more easily made. The recent possibility of artificial satellite measurements of the general scattering behavior is being exploited for both the moon and the planets [Fjeldbo, 1964; Tyler, 1967].

Most of this report is concerned with the measurement techniques, sources, and effects of error and distortions of the signals from the propagating media. The exact nature of the latter of fundamental importance to these measurements and much effort has been made to measure and compensate for them. The most important of the ionosphere effects is the Faraday rotation, which is discussed in Chapter III, where it is shown that it can be measured directly from these data. In Chapter IV the effect of the Faraday rotation on the data analysis is considered, and a simple method for using it to separate the expected (i.e., the transmitted) polarized component of the echoes from the depolarized (sometimes called the "cross-polarized") component.

Some basic properties and results of short-pulse studies are presented in Section B of the present chapter. The physical equipment and the waveforms used are described in Chapter II, along with the preliminary data processing method. Preliminary results are also presented there. In Chapter V the results of the overall analysis are presented and discussed.

B. Angular and Short-Pulse Power Spectra

The geometry of short-pulse backscattering from a smooth sphere appears in Fig. 2. The total amount of surface area illuminated by a pulse of length τ is independent of delay and is given by $2\pi ac\tau$, where a is the radius of the moon and c is the free space velocity of light. If the pulse is short compared to the total range depth, the angle of incidence of the radiation is nearly constant over the illuminated annulus and is given by

$$\theta = \cos^{-1}\left(1 - \frac{ct}{2a}\right) \tag{1.1}$$

The projected area of the illuminated annulus does vary with t, and falls as $\cos\theta$, so

$$A_{proj} = 2\pi ac\tau\left(1 - \frac{ct}{2a}\right) \tag{1.2}$$

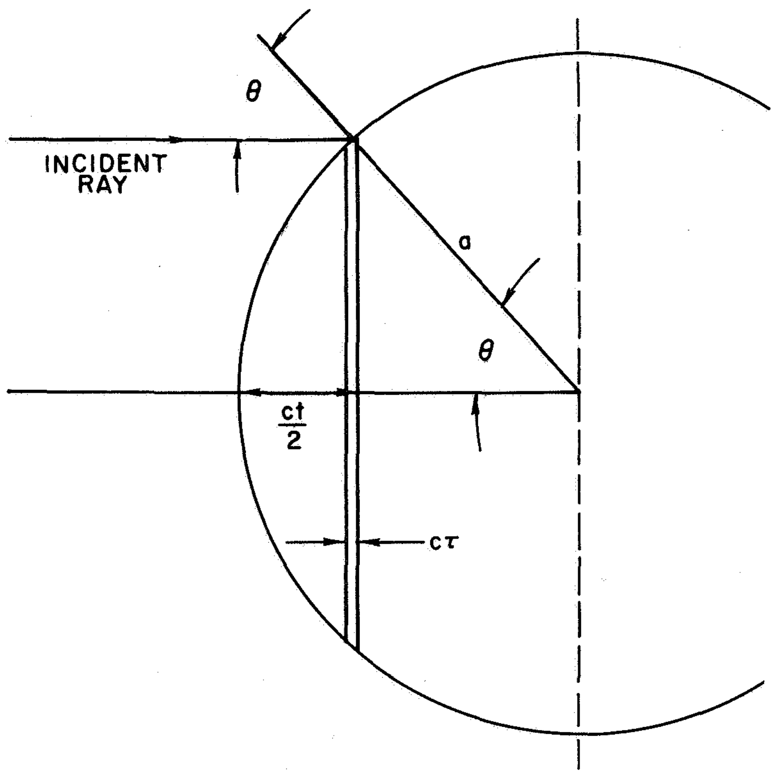

Fig. 2. GEOMETRY OF SHORT-PULSE BACKSCATTERING.

It is the direct relationship between the nearly constant angle of incidence over the illuminated annuli and the delay time which allows the average echo power as a function of delay, $P(t)$, to be interpreted as power as a function of the angle of incidence, $P(\theta)$. This is done to compare $P(t)$ to the angular scattering behavior of various types of surfaces, such as one that follows Lambert's law, where the brightness B is proportional to the projected area and therefore varies as $\cos\theta$, or one that is uniformly bright. Since the radar cross section per unit area is proportional to $B\cos\theta$, $P(\theta)$ is proportional to $\cos^2\theta$ and $\cos\theta$, respectively, for the two cases.

The comparison between $P(t)$ and $P(\theta)$ is facilitated by the constancy of the illuminated area, and is made using Eq. (1.1) [Evans, 1965]. The reflecting characteristics of the lunar surface must be assumed to be statistically uniform over all annuli at different ranges, a reasonable assumption since their areas are so large (a 20 μs pulse illuminates an area of 6.6×10^4 km^2) and all types of lunar terrain would be expected to be included in any annulus. For a rough sphere like the moon, the mean surface is used as the reference between delay and angle.

There are a number of difficulties, however, in interpreting $P(t)$ in terms of the angle of incidence. Only for a smooth sphere and an infinitesimal pulse width does $P(t)$ accurately specify the angular scattering behavior. Thus $P(\theta)$ might be defined as the "impulse response" of the sphere; however, the notation will be changed here such that the impulse response, or "delay spectrum," will be written as $D(t)$ to make the time variation more explicit. Because an impulse contains all frequencies, the spectrum of the impulse response has to be specified over a wide range of incident wavelengths. When a real pulse is used to determine $P(t)$, its spectral extent is limited to a region about its carrier frequency f_o, so $P(t)$ is actually $P(t;f_o,T)$, where T is the pulse length. Thus any practical measurement only estimates $D(t)$ in a small part of its spectral extent. When $P(\theta)$ is interpreted as the angular scattering law for monochromatic waves from a flat surface, as it often is for theoretical studies [Beckmann, 1965; Hagfors, 1964], it is clearly only an approximate procedure because of the finite and perhaps large spectral extent of the real signals. The assumption must be that the scattering properties, at least on the average, are independent of frequency over the range of interest, which is reasonable since observations indicate they do not change very rapidly for the moon.

Before further considering the relation between delay and angle spectra for any rough sphere, let us consider the relation between $P(t)$ and $D(t)$ more carefully. Hagfors [1961] showed that the average (over an ensemble of realizations of a motionless rough reflector) power response, $\bar{P}(t)$, to a signal $s(t)$ is

$$\bar{P}(t) = \overline{|r(t)|^2}$$

$$= \left(\frac{1}{2\pi}\right)^2 \iint_{-\infty}^{\infty} R(\triangle\omega)\ S^*(\omega)\ S(\omega + \triangle\omega)\ e^{j\triangle\omega t}\ d\omega\ d\triangle\omega \tag{1.3}$$

where

$$r(t) = \int_{-\infty}^{\infty} S(\omega)\ H(\omega)\ e^{j\omega t}\ df = \text{response to } s(t)$$

$$S(\omega) = \int_{-\infty}^{\infty} s(t)\ e^{-j\omega t}\ dt$$

$$H(\omega) = \int_{-\infty}^{\infty} h(t)\ e^{-j\omega t}\ dt$$

$h(t)$ = impulse response of moon

$$R(\Delta\omega) \triangleq \overline{H^*(\omega)\ H(\omega + \Delta\omega)} = R(\Delta\omega)$$

The important assumption is that the statistical properties of $H(\omega)$ are independent of frequency. Thus $\overline{|H(\omega)|^2}$ is a constant. $D(t)$ is given by the expression

$$D(t) = \int_{-\infty}^{\infty} R(\Delta\omega)\ e^{j\Delta\omega t}\ df \tag{1.4}$$

Now, Eq. (1.3) can be written as

$$\bar{P}(t) = \int_{-\infty}^{\infty} R(\Delta\omega) \left[\int_{-\infty}^{\infty} S^*(\omega)\ S(\omega + \Delta\omega)\ d\omega\right] e^{j\Delta\omega t}\ d\Delta f$$

$$= \int_{-\infty}^{\infty} R(\Delta\omega)\ R_s(\Delta\omega)\ e^{j\Delta\omega t}\ d\Delta f \tag{1.5}$$

It can be easily shown that

$$\int_{-\infty}^{\infty} R_s(\Delta\omega)\ e^{j\Delta\omega t}\ d\Delta f = s^2(t) \tag{1.6}$$

so

$$\bar{P}(t) = D(t) * s^2(t) \tag{1.7}$$

Therefore, if $s(t)$ is a narrow pulse, then $\bar{P}(t) \cong D(t)$ is in agreement with Hagfor's result.

Because $S(\omega)$ is a bandlimited function for the radar pulses normally used, and, for practical frequencies and pulse lengths used for lunar work, is usually a very narrow band signal, $\overline{H^*(\omega)\ H(\omega + \Delta\omega)}$ doesn't change rapidly over the bandwidth of $S(\omega)$, and an approximation to it which is only close in that range would be expected to give accurate results in Eq. (1.5) or (1.7). We can define a frequency-dependent correlation function $R(\Delta\omega; \omega_o)$, which is nevertheless only strongly dependent on $\Delta\omega$ in the bandwidth around ω_o occupied by $s(t)$, and assume that it holds over all frequencies. Thus $D(t) \rightarrow D(t;\omega_o)$ and Eq. (1.7) becomes

$$\bar{P}(t;\omega_o) = D(t;\omega_o) \cdot s^2(t)$$

This expression shows that if $D(t;\omega_o)$ doesn't change significantly in the width of the pulse $s(t)$, then $\bar{P}(t;\omega_o) \cong D(t;\omega_o)$ holds and the correspondence between delay and angle can be accurately made. Clearly this correspondence cannot be at the leading edge of the return because $D(t;\omega_o)$ changes abruptly. Therefore very short pulses would be needed to explore $P(\theta)$ at small values of θ. Also, comparisons between $\bar{P}(t;\omega_o)$ at different ω_o's can only be accurately made when the same pulse length is used.

For a rough sphere there is some further difficulty. Because of the height of the surface features, power at some particular delay can come from several features separated in angular position and thus Eq. (1.1) does not hold. For instance, 10 μs of delay corresponds to 1.5 km, which is smaller than many large scale features; and indeed, the moon's surface deviates several kilometers from a sphere over very large areas. This effect is largest for very short pulse lengths and at the subradar point, for at bigger ranges the angle varies very little between adjacent annuli. Nevertheless, the identification between delay and angle is almost invariably made--even though it is very approximate at the leading edge--and is useful for studying the scattering behavior.

The general result of the short-pulse studies is that the moon is a limb dark scatterer. Most of the returned power comes in the first millisecond or so of the echo, as the power drops rapidly with increasing range in this region and then more slowly until the last 2 ms before the limb, where it decreases rapidly again. The leading edge spike becomes narrower and stronger as the wavelength is increased, and there is some evidence that its area increases also, since the total radar cross section apparently increases at the long wavelength limit of lunar studies [Davis et al, 1965]. This leading-edge spike is termed the "quasi-specular" component of the echo since it apparently comes from favorably oriented, nearly flat areas on the moon's surface. The remaining part of the echo is called the "diffuse" component, and although a number of possible mechanisms have been proposed to explain its generation, it is generally considered to arise from reflection from the small scale structure (i.e., dimensions comparable to the wavelength) on the surface. The diffuse component is considerably depolarized, while the quasi-specular theoretically is only slightly depolarized [Beckmann, 1968]. The depolarized component of the echoes does not have a spike at the leading edge, and actually appears uniformly bright, $P(\theta)$ varying as $\cos\theta$, at least at 23 and 68 cm [Evans and Hagfors, 1966]. There is some controversy over the origin of the depolarized component, whether from multiple scattering, surface layers, small scale structure, or inherent in a gently undulating, quasi-specular scattering surface.

The total scattered field from the moon's surface is the linear sum of the contributions from all the elemental scatterers on the surface. Even for a monochromatic incident wave the total field would be expected to be very complex, with its exact nature at any instant specified by the relative disposition of the elemental scatterers and their properties. The libration causes their apparent relative positions to change, and the echoes to fade. The fading is deeper and slower at the leading edge of the echoes than it is at greater ranges. Therefore, it is necessary to average a number of echoes together to get the mean scattered power. While this procedure is certainly not the same as averaging over an ensemble of realizations of the moon's surface because the rotation of the moon is very small during the averaging period, it has been shown that the error is small [Ruffine, 1967]. That study was limited to CW signals, but the result should apply to pulse signals equally well.

Chapter II

EXPERIMENTAL METHOD

A. Choice of Operating Parameters

The choice of operating parameters, such as the effective pulse length and operating frequencies, for this experiment was determined by its primary goal, which was to measure the electron density in the cislunar medium by observing the increase in delay time of lunar radar echoes over its free space value of about 2.5 sec [Howard et al, 1965]. This measurement requires simultaneous transmission on two frequencies (one of them in the HF range), a very short effective pulse length, and sufficient sensitivity to obtain strong echoes, all three requirements necessarily having to be compromised with the available equipment. Since the extra group delay is an inverse-square function of the operating frequency, a low frequency makes the delay measurement both easy to perform and accurate; but the requirement that the signals penetrate the ionosphere sets a lower limit in the 20 to 30 MHz range. At 25 MHz, the extra delay is on the order of 100 μs, which means that the pulse length should not be larger than 10 μs and that the free space delay must be known to better than 1 part in 10^6. The second requirement can be eliminated by measuring the difference in propagation times between pulses of two different frequencies [Eshleman et al, 1960].

Because the available transmitters are CW types, some kind of pulse compression technique is necessary to obtain both good range resolution and sufficient sensitivity. For this work a linear constant-amplitude frequency sweep, or "chirp," was used, and the development at Stanford of a digitally synthesized frequency sweep allowed the transmission of signals with time-bandwidth products of greater than 10^5, an improvement of more than an order of magnitude over previous capabilities [Fenwick and Barry, 1965]. A time-bandwidth product of 10^5 was used for the lunar measurement, with simultaneous transmission of 100 kHz width, 1 sec duration sweeps in the ranges of 24.9 to 25.0 MHz and 49.8 to 49.9 MHz. Although the instantaneous frequency of the sweeps did not change smoothly, but rather in discrete steps, the error in considering it to be continuous is negligibly small as will be shown below.

The equipment was operated for about a 2 hr period around lunar meridian transit for a few days in December 1964, and then later through July and August 1965, and the columnar electron content was obtained for two lunations [Howard, 1967]. Only the relative group delay between the strong leading edge of the echoes at the two frequencies was measured, although the analysis showed the expected decay in strength beyond the leading edges in a qualitative way. This present study uses the data recorded for the cislunar density study to make quantitative measurements of the scattering behavior of the moon.

B. Equipment and Signal Description

The antennas used were the 48-element log-periodic array [Howard, 1965] on 12 m and the steerable 150 ft paraboloid on 6 m, which are located near each other at Stanford. Although they have approximately equal gains referred to their respective operating frequencies, the LPA has a fan beam approximately 2° thick in elevation and 30° in azimuth, while the 6 m antenna produces a pencil beam. Before a run was begun, the LPA was aimed in elevation by adjusting the phasing of the elements, and was typically adjusted once during the run to keep the target in the beam. Since the 3 dB beamwidth of the individual antennas is 60° and they are aimed at a 60° elevation angle, the array performance falls off by 3 dB at 30° and 90° elevation angles. The 150 ft dish was constantly kept aimed at the target by a digital computer. The same antennas were used for both transmitting and receiving.

The parameters of the two radars are summarized in Table 2. The gain of the LPA was measured by comparing the strength of lunar echoes using the LPA to that of a dipole above a ground screen. During a frequency sweep the variation in transmitted power was held to less than 1 dB and probably was less than 0.2 dB.

Approximately two and one-half of the 100 kHz width, 1 sec duration sweeps were transmitted on both frequencies simultaneously, after which the receivers were connected to the antennas for the next 2.5 sec, the

Table 2

RADAR PARAMETERS

Wavelength (m)	12	6
Frequency sweep (MHz)	24.9-25.0	49.9-49.8
Antenna	48-element LPA	150 ft paraboloid
Antenna gain (dB)	25.3 + 1,-2	24 ± 1
Polarization	Linear	Linear
Feed losses (dB)	0.6	< 0.4
Transmitted power (kW)	250 ± 50	45 ± 5

actual length of time chosen being the computed round-trip time on the particular day. This process was then repeated, giving a 50 percent duty cycle (Fig. 3). The fact that the 50 MHz frequency sweep was actually "backwards" has no fundamental importance. Much more importantly, the

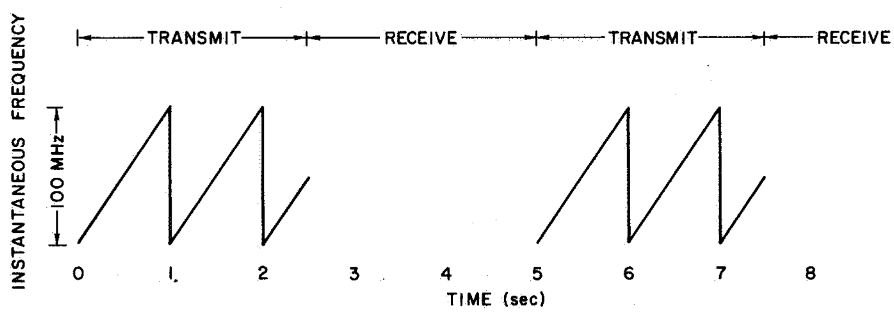

Fig. 3. FREQUENCY-TIME TRACKS OF TRANSMITTED SIGNAL.

transmit-receive switching time required was about 0.5 sec, so that the beginning half of the first sweep was neither transmitted nor received, thus making the second sweep the only full one. No coherence was maintained between sweeps.

A block diagram of the system is shown in Fig. 4. All the signals used in the system were derived from a crystal standard having a stability of 5 parts in 10^{10} per day. Following a delay of about the round-trip time after the transmitted sweeps were begun, another sweep from the

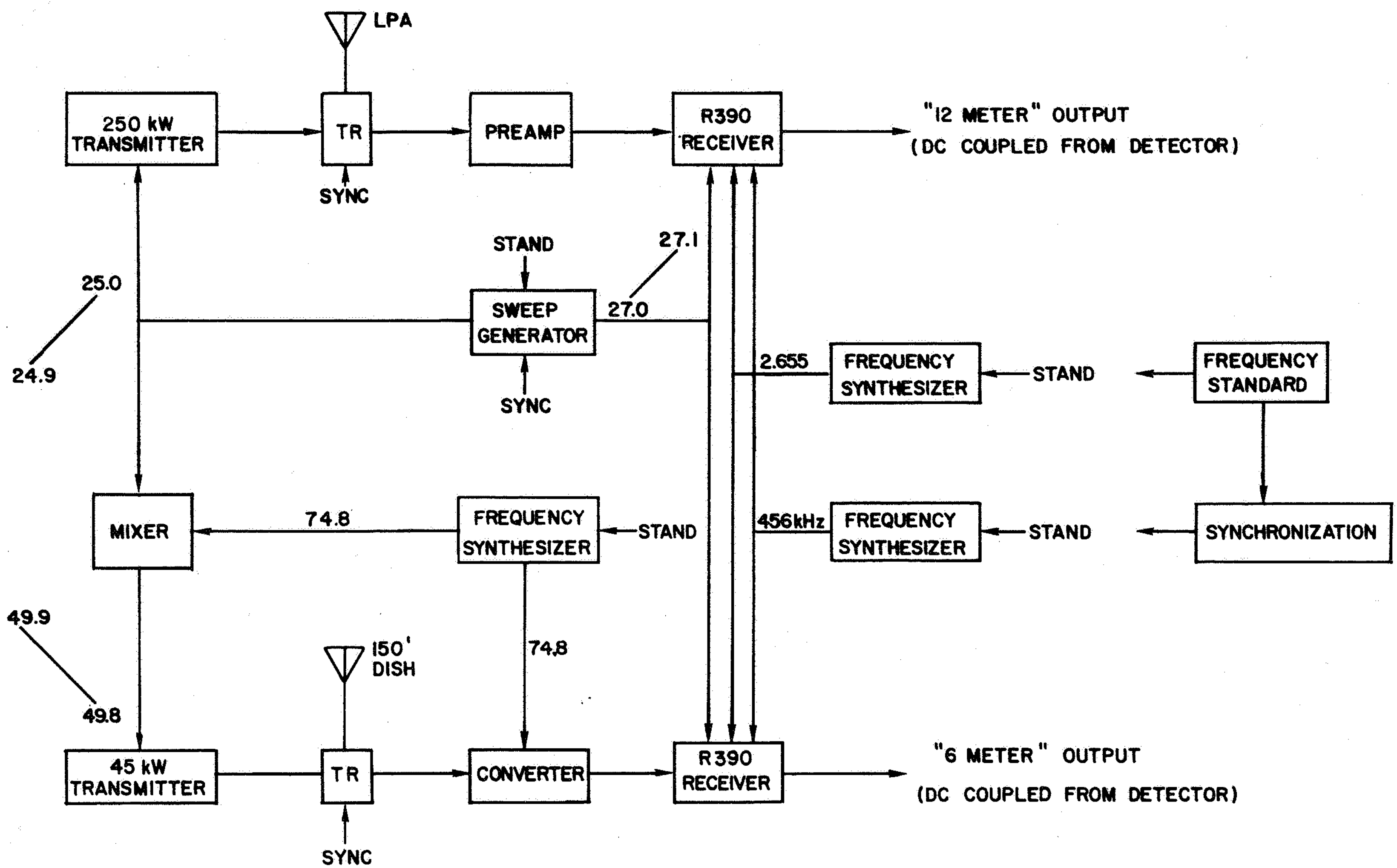

Fig. 4. BLOCK DIAGRAM OF MOON-CHIRP SYSTEM.

same generator but with a different starting point was started and mixed with the incoming signals in the R390 receivers. The resulting signals were then heterodyned first to the center of the IF bandwidth and then at the detector to the audio-frequency range with signals from two frequency synthesizers, and these final output signals were recorded on magnetic tape. The IF bandwidths--which have a very flat characteristic--of the R390 receivers were set to 2 kHz. A rough measurement showed that the overall response of the receiving system was flat to within 0.5 dB, and quite likely it was much better than that.

The approximations to a linear sweep were generated by making the frequency increase in small equal steps (Fig. 5) and maintaining phase

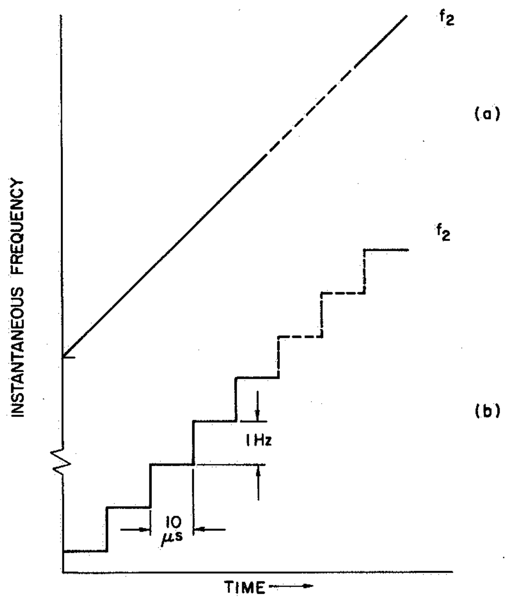

Fig. 5. APPROXIMATION TO LINEAR SWEEP. (a) Ideal; (b) approximate linear sweep.

phase continuity between steps [Fenwick and Barry, 1965]; the step size for the moon radar experiment was 1 Hz every 10 μs. A Hewlett-Packard 5100A-5110A frequency synthesizer was modified to allow rapid switching, and special equipment was built to generate the switching signals in order to produce the required sweep (Fig. 6).

The frequency and phase errors that occur in approximating a linear sweep in this way are shown in Fig. 7 along with the piecewise sweep and

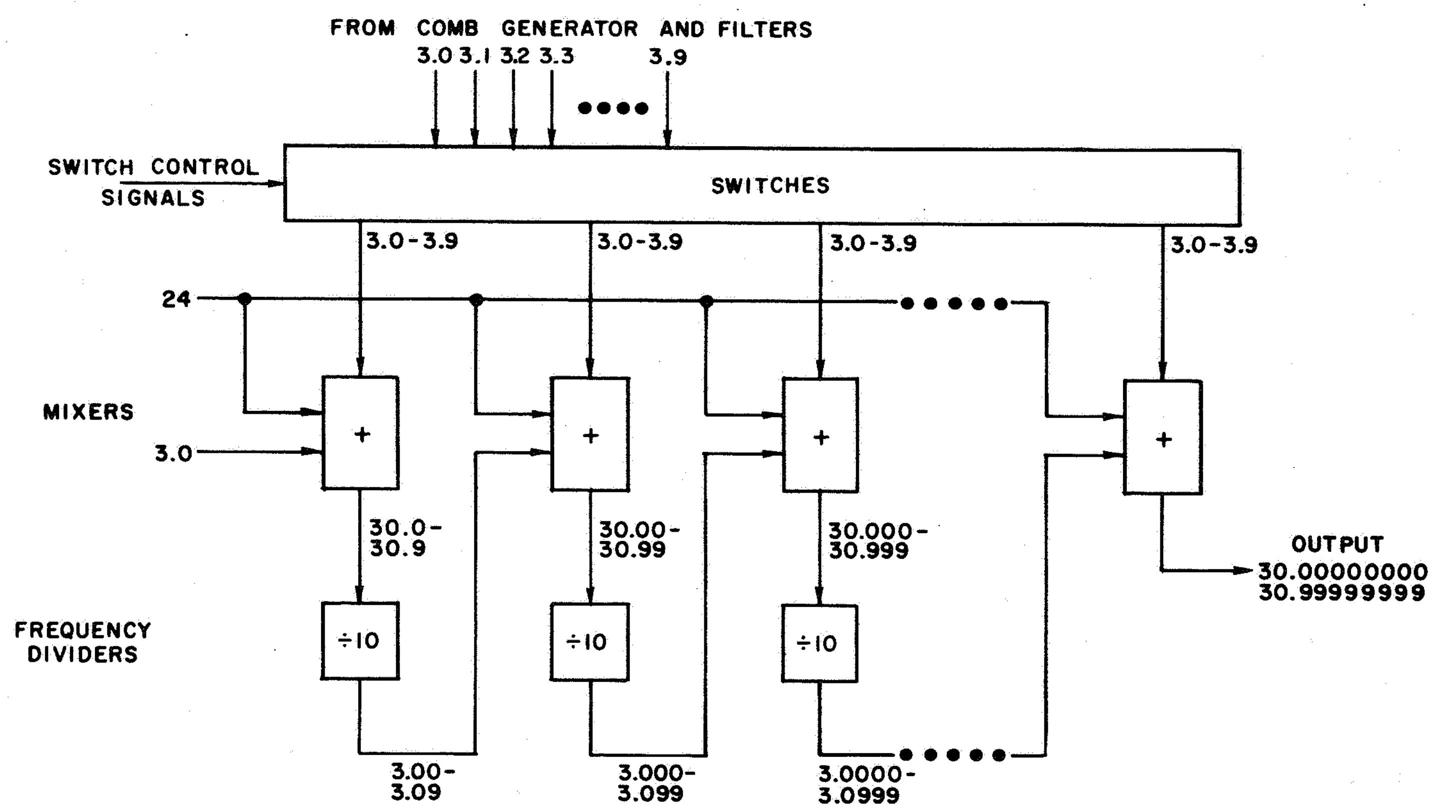

Fig. 6. SIMPLIFIED BLOCK DIAGRAM OF SWEEP SYNTHESIZER. (All frequencies in MHz.)

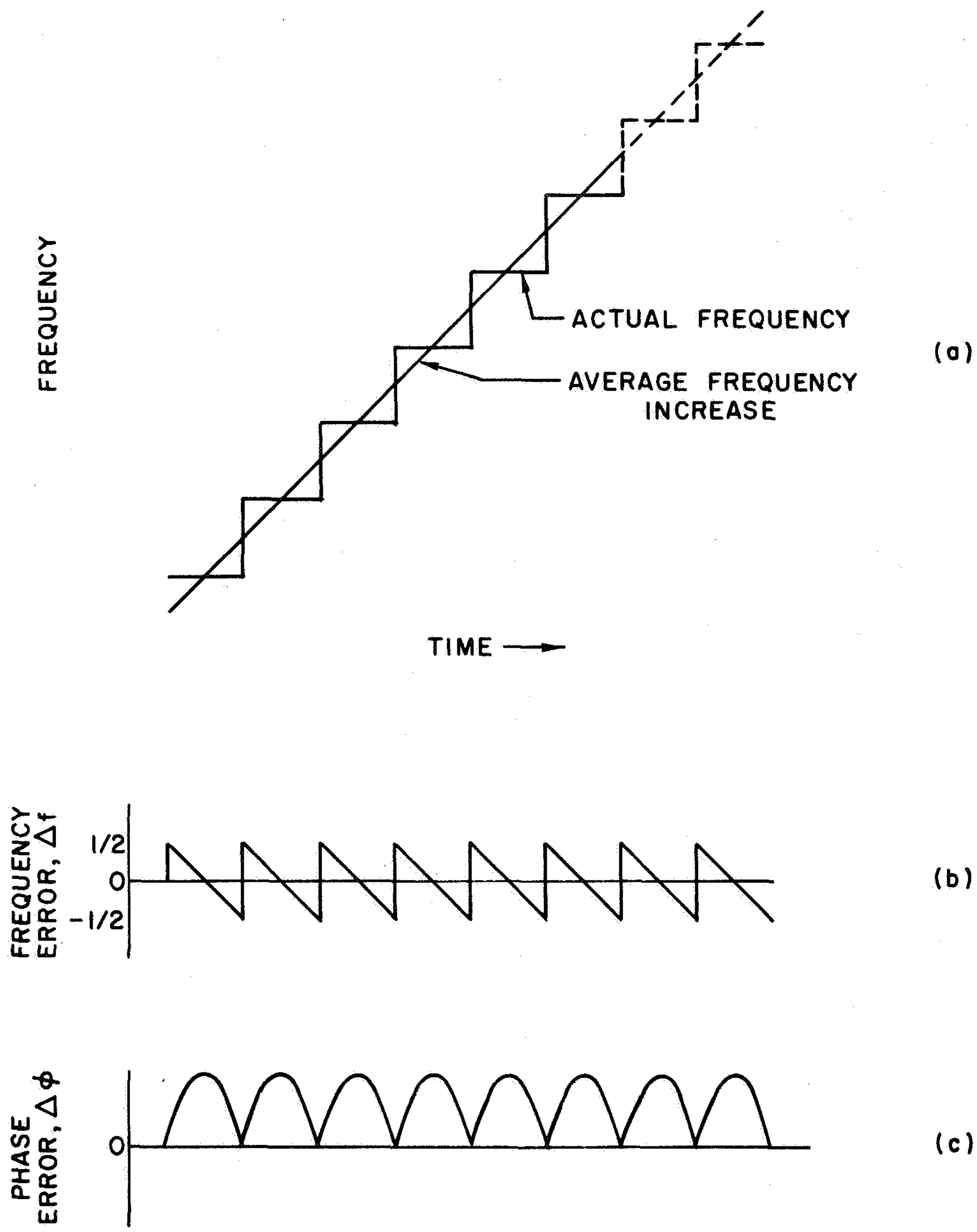

Fig. 7. FREQUENCY AND PHASE ERRORS IN PIECEWISE APPROXIMATION TO LINEAR FREQUENCY SWEEP. (a) Ideal and actual sweeps; (b) frequency error; (c) phase error.

the sweep it approximates; the latter is defined as the one for which there is no progressive phase error. Since the steps are 1 Hz high, the frequency error, $\Delta f(t)$ is a zero-average sawtooth with a maximum amplitude of 0.5 Hz; and because the phase is the integral of the instantaneous frequency, the phase error $\Delta\phi(t)$ is parabolic in shape with a maximum value of 7.85×10^{-6} radian. There is also another source of phase error: the lack of perfect phase continuity as the frequency is stepped.

The continuity is controlled by the phase relationships between the 10 frequency inputs to the switches in the synthesizer (Fig. 6). Their relative phase relationships are preserved at multiples of a 10 μs interval (the step length) since in that time the 3.0 MHz signal would have completed 30 cycles, the 3.1 MHz 31 cycles, and so on. Thus if they have no relative phase difference at one switching time, they will be in phase at all the rest, and any phase errors will repeat sequentially for every digit position in the output frequency. However, since the frequency dividers also divide the phase jumps, the errors get smaller proportionally to the frequency steps: the largest ones happening in the 10 kHz position, one-tenth as much in the 1 kHz position, etc. The phases are random after the machine is turned on, and are adjusted for as small errors as possible by interrupting the drive to the dividers that produce the 3.0 to 3.9 MHz signals.

It is important to determine how accurately the stepwise chirp approximates an ideal one. The ideal chirp can be written as

$$c(t) = \cos \phi(t) = \cos (\xi t^2 + \omega_o t + \phi_o) \tag{2.1}$$

where $f_o = \omega_o/2\pi$ = "starting" frequency. The initial phase ϕ_o is unimportant and will be set to zero for convenience. Since instantaneous frequency is the rate of change of phase,

$$f(t) = \frac{1}{2\pi} \frac{d}{dt} \phi(t) = 2\psi t + f_o \tag{2.2}$$

where $\psi = \xi/2\pi = \pm 5 \times 10^4$ for the 100 kHz wide, 1 sec duration chirps. The phase of the stepwise chirp can be written as the sum of the phase of an ideal chirp plus the error terms, which are summed together as $\Delta\phi(t)$, so that

$$s(t) = \cos [\xi t^2 + \omega_o t + \Delta\phi(t)] \tag{2.3}$$

By an elementary trigonometric expansion, this becomes

$$s(t) = \cos \Delta\phi(t) \cos (\xi t^2 + \omega_o t) - \sin \Delta\phi(t) \sin (\xi t^2 + \omega_o t)$$

and since $\Delta\phi(t)$ is a small quantity,

$$s(t) \cong \cos (\xi t^2 + \omega_o t) - \Delta\phi(t) \sin (\xi t^2 + \omega_o t) \tag{2.4}$$

The contribution to the second term from the parabolic phase error component of Fig. 7 is clearly negligible since it has a maximum value of 7.85×10^{-6} radian and furthermore has a wide spectrum due to its 100 kHz repetition rate. When $\Delta\phi(t)$ is a repetitive function the second term can be interpreted as a series of parallel sweeps with different starting frequencies spaced as the frequency components of $\Delta\phi(t)$ and centered at the ideal sweep.

The most important of the continuity phase errors are the ones that occur when the 10 kHz digit changes, both because they are the largest and because their spectral extent is smallest due to their 10 Hz basic repetition rate. However, the actual nature of the spectrum of this component of $\Delta\phi(t)$ depends on the particular configuration of the phase errors; an example of one such configuration is shown in Fig. 8. Although $\Delta\phi(t)$ is random in that the phase jumps cannot be specified completely, but only minimized in their maximum extent, it is deterministic in the sense that once it has been set it is repetitive thereafter.

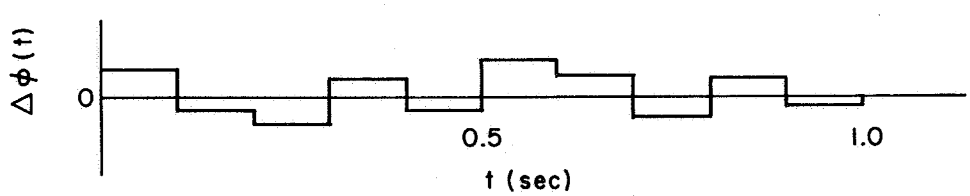

Fig. 8. "TYPICAL" CONTINUITY PHASE ERROR (FOR 10 kHz DIGIT).

The magnitude of $\Delta\phi(t)$ could only be set less than 18°, which is a very serious amount, although $\Delta\phi(t)$ was probably somewhat smaller than that. Fortunately, the same sweep generator is used in the receiving process, and therefore, except for the small misalignments in delay between the echoes and the receiver sweep, the phase errors cancel in the receiver output signal. During the early series of runs two separate sweep generators were used so this cancellation did not occur, and sidebands separated by 10 Hz from the main signal were easily observed. Because the magnitude of the more rapidly changing components of $\Delta\phi(t)$ decrease rapidly, the strongest nonideal sweep components are closely spaced around the ideal sweep; and the important quantities concerning the transmitted signal, such as the frequency-dependent propagation parameters, are adequately described when Eqs. (2.1) and (2.2) are used.

C. Characteristics of the Receiver Output Signal

The real-time processing of the reflected signals in the receiving system is easily recognized as at least the beginning of a crosscorrelation detection scheme because the incoming signals are multiplied by an almost perfect duplicate, in the sense of its phase modulation, of the transmitted signal. However, the output signal is not really a correlation and it is important to determine exactly what it represents. In the next section it will be seen that the total processing of this signal can be considered to be a completion of the correlation process, but it is much more convenient at this point to consider the output signal separately.

Suppose that there is a discrete stationary target at about the range of the moon. Then the reflected signal will have the same phase behavior as the transmitted signal--assuming that its reflective properties are not dependent on the instantaneous frequency over the span of the sweep--but will be delayed in time by T_o. At that time another sweep is begun in the receiver and mixed with the reflected sweep, the difference term being a constant frequency signal whose magnitude is proportional to that of the reflected signal and whose frequency can be set arbitrarily by the two frequency synthesizers supplying the other mixing signals in the receiver (Fig. 4). If this frequency is set to zero but the target had a delay T_d instead of T_o (Fig. 9), the receiver output signal would have a constant frequency f_d over most of the duration of the sweep

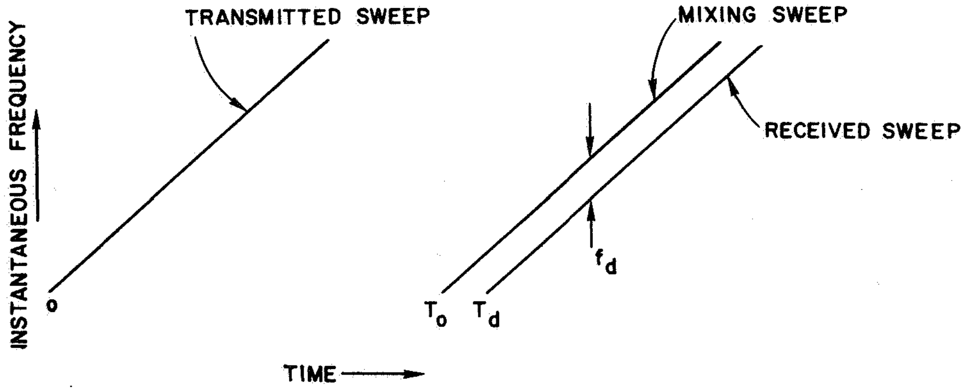

Fig. 9. RELATIONSHIP BETWEEN TRANSMITTED, RECEIVED, AND MIXING SWEEPS.

which would be proportional to the difference in delay time $T_d - T_o$. For the 100 kHz wide, 1 sec length sweeps, 10 μs of delay corresponds to 1 Hz.

When there are a number of discrete targets as in Fig. 10, the output is the sum of the individual signals from the targets, each having

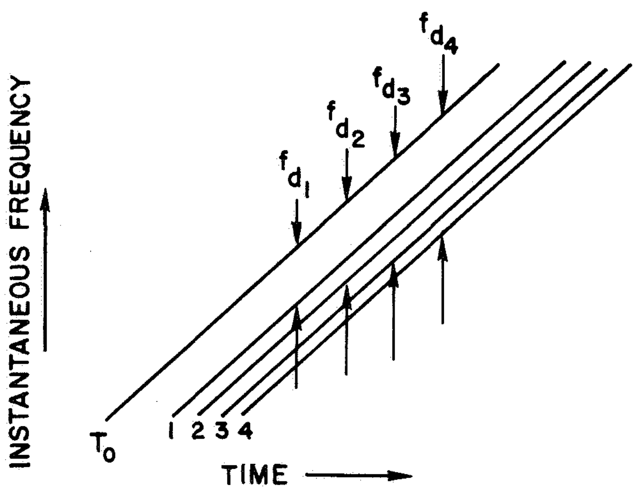

Fig. 10. MIXING AND RECEIVED SWEEPS FOR SEVERAL DISCRETE TARGETS.

its own specific frequency corresponding to its particular range. The reflected signal from each differential surface element of a large extended target like the moon similarly corresponds to a particular frequency, so the receiver output signal from the entire target is a continuum of frequencies. Thus one is led immediately to the idea of some kind of spectral analysis to separate the contribution to the overall scattering from different ranges. This was the method used to resolve the leading edges of the echoes to measure the delay time difference between 25 and 50 MHz [Howard et al, 1965]. For this study, digital spectral analysis is used because of its greater accuracy and flexibility. Each echo is independently Fourier analyzed and its energy spectral density computed from the squared magnitude of the Fourier transform.

The time delay T_o and the other mixing frequencies supplied to the receivers were adjusted to place the output frequency corresponding to the leading edges at some low frequency, usually between 0 and 100 Hz. Therefore the equivalent frequency of the limb is about 1200 Hz, and since this corresponds to a delay of 12 ms, the received and mixing sweeps fail to coincide in time by only about 1 percent at most. Except for the small periods equal to the delay between the mixing and received sweeps, the phase discontinuities discussed about subtract out in the mixing process; and since the strongest components of the echoes have the smallest delay, the nonideal sweep components are further reduced in the output. Therefore the output signal can be accurately considered to be the result of heterodyning perfect sweeps even though that is not the real situation.

The moon is not a stationary target, of course, and to an observer on the surface of the earth both its range and range rate appear to change; it has a varying amount of apparent rotation caused by its real motion in its eccentric orbit and by the rotation of the earth. During the ±1 hr periods around lunar meridian transit when the radars were operated, the apparent gross motion of the moon is first toward the observer, then momentarily stationary, and finally away from him. Over this interval the apparent range is very accurately parabolic and the range rate is a linear function of time; the apparent rotation is nearly constant. The subradar point on the surface moves only slightly during a run because the apparent rotation is small. All these quantities vary from day to day, with the apparent rotation and its axis, and the position of the subradar point showing the largest variation, and all were calculated for each run from a computerized ephemeris which was also used to point the 50 MHz antenna.

To first order, the range differences and the range rate cause the same effect in the receiver output signal--a shift in frequency. This is a familiar effect in chirp-radar systems where certain combinations of target range and velocity cannot be resolved, as described by the ambiguity function [Berkowitz, 1965]. Here there is only one target, whose range rate is well known; and since only relative ranges between parts of the target are of interest, only compensation for the motion on the output signal needs to be considered. The linear change of range rate, $\dot{R}$, causes a linear change in doppler shift which goes through zero some time near transit at a rate of about -4×10^{-3} Hz/s at 50 MHz, as shown in Fig. 11. At any particular time the frequency-time tracks of the echoes

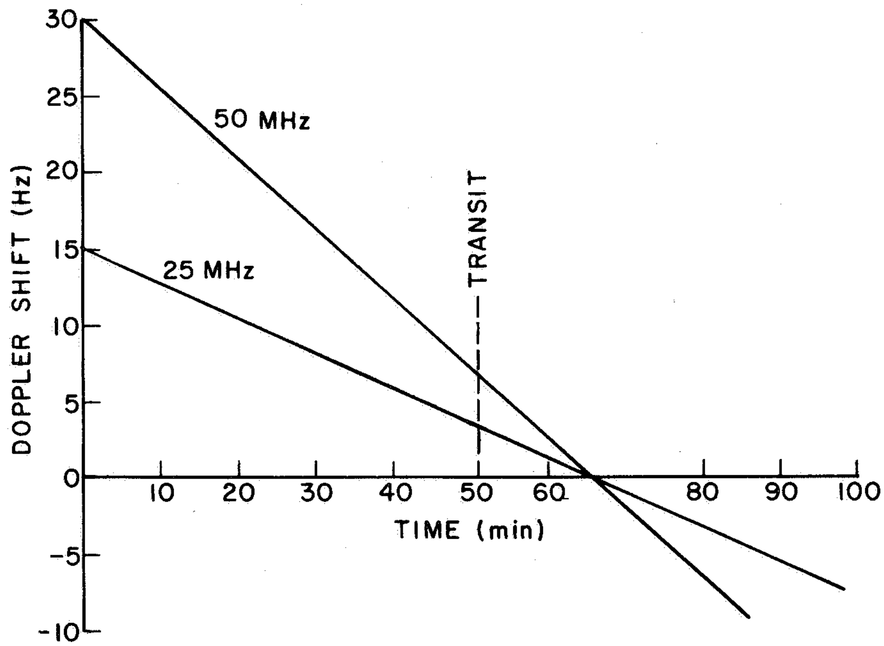

Fig. 11. DOPPLER SHIFT NEAR TRANSIT FOR 24 AUGUST 1965.

are displaced by the amount of doppler shift and are slightly skewed because the shift is different at the ends of the sweep (Fig. 12). Note that the displacement is toward smaller ranges at 25 MHz but toward greater ranges at 50 MHz since that sweep is backwards. The amount of skewedness is the same for both frequencies and is less than 0.05 Hz in the 1 hr period around transit.

The constant apparent radial acceleration of the moon causes the range R to have a parabolic time variation, which can be added to the

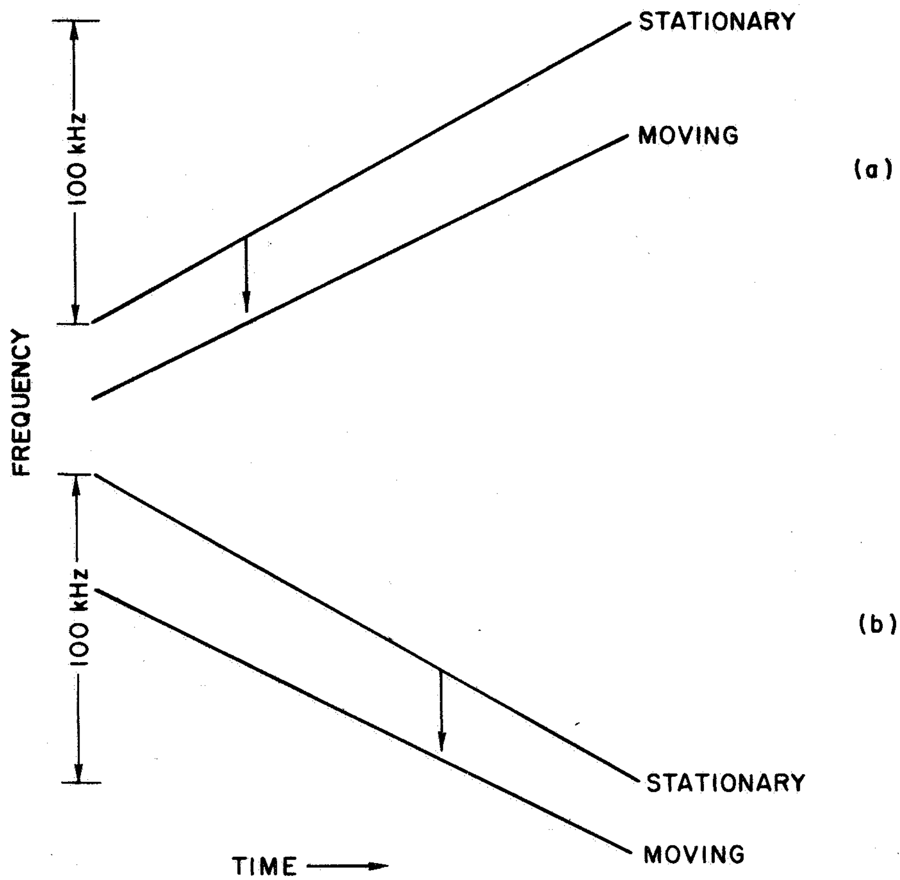

Fig. 12. FREQUENCY-TIME TRACKS FROM A RECEDING TARGET (CONSIDERABLY EXAGGERATED) COMPARED TO STATIONARY TARGET AT THE SAME RANGE. (a) 25 MHz; (b) 50 MHz.

doppler to get the entire long-term time variation of the receiver output signal. Because $R = \int \dot{R}\, dt$, this changing frequency due to the changing range in the output can be easily related to the varying doppler shift. The skewednesses in the individual echoes from the frequency dependence of the doppler shift and from the finite change of range during the 1 sec pulse length cause the receiver output signal from any element of the target to be phase-modulated instead of having a constant frequency, but since it can only shift 0.05 Hz at most, the effect is much smaller than the available resolution of the spectral analysis and therefore is negligible.

Since it was not necessary for the cislunar electron content measurement to make an accurate quantitative study of the scattering but rather just to quickly and accurately measure the range difference, the recorded receiver output signal was analyzed by a Spectran spectrum analyzer. The output of the analyzer was then used to intensity-modulate a cathode ray tube and the display was photographed by a moving film. Figure 13 is an example of these spectral analyses with the 25 and 50 MHz signals superimposed. The parabolic shapes due to the motion can easily be seen; the

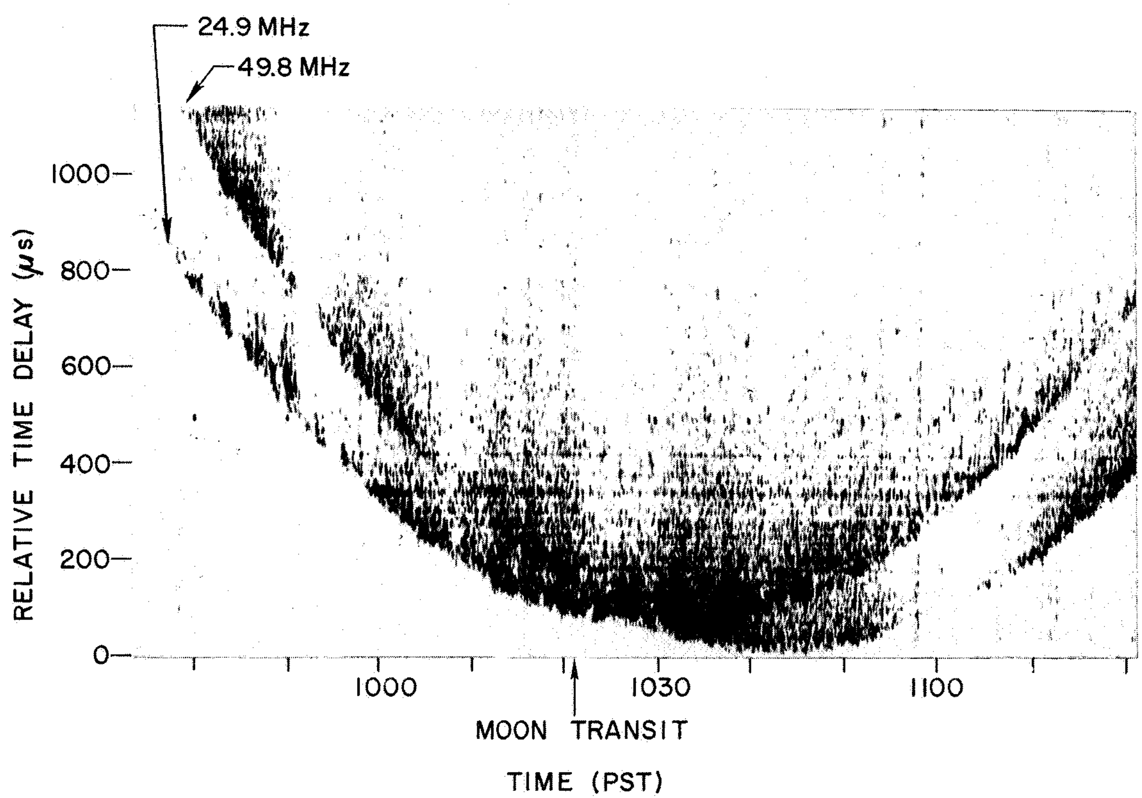

Fig. 13. SPECTRUM ANALYZER OUTPUT OF THE 25 and 50 MHz ECHOES SUPERIMPOSED. Run of 24 August 1965.

lack of a perfect match between the two is due to the different doppler shifts and to the differential group delay time. The slow fading is caused by the changing amount of Faraday rotation, and the rapid fading is due to the apparent rotation of the moon.

Because the frequency of the output signal from an elementary scattering area depends on both its range and range rate, the moon's apparent rotation, or libration, prevents the regions that lie in a small band of frequencies from corresponding exactly to the constant range annuli of the short-pulse studies discussed in Chapter I. The rotational doppler shift is directly proportional to the projected distance from the libration axis and has a maximum value at the limb of about ±0.4 Hz at 12 m and ±0.8 Hz at 6 m [Browne et al, 1956]. Thus the region of the moon corresponding to a small frequency interval in the receiver output signal is still an annulus, but is no longer perpendicular to the observer's line of sight (Fig. 14). This effect is small for annuli closest to the subradar point, but the result that the angle of incidence of the radiation

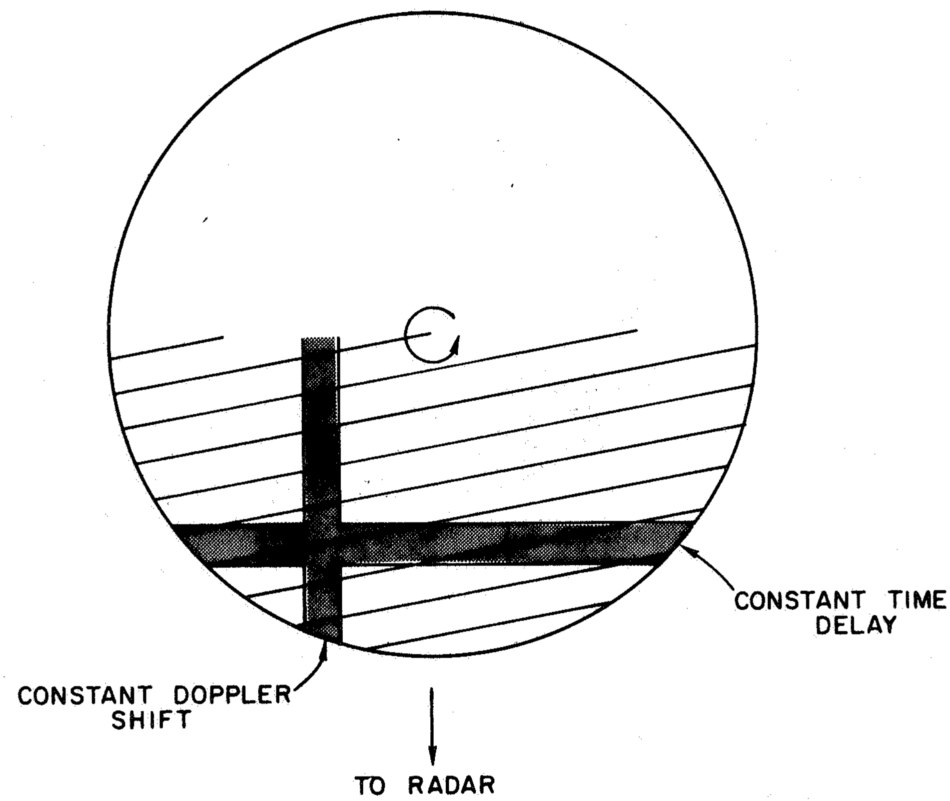

Fig. 14. DISTORTION OF CONTOURS OF CONSTANT RECEIVER OUTPUT FREQUENCY CAUSED BY THE MOON'S LIBRATION.

to the mean surface is constant over an annulus becomes more and more inaccurate with increasing ranges. Even so, its magnitude is only sufficient to cause at most a change of one resolvable range interval at 50 MHz and is therefore completely negligible here, particularly since a much coarser range resolution than is available with this signal is used to study the returns from the greater ranges. The rapid fading of the echoes, which is caused by the relative motions of the elementary scattering regions, is very sensitive to the libration rate, of course, and more rapid fading is expected from range intervals nearer the limb since the relative velocities are greater there.

The noise component of the receiver output signal was mostly due to the galactic noise, whose brightness temperature is about 6000°K at 50 MHz and 30,000°K at 25 MHz. Excess receiver noise was negligible in comparison; and except for interference from the vestigial sideband of a local television station on the 50 MHz echoes and power line noise at both frequencies, there was usually little noise or interference from other sources. Thus most of the input noise can be described as white gaussian noise; the other sources of noise tend to be wideband also, but their statistics are unknown and appear to be very nonstationary.

There are two ways of considering the effect of the noise. First, one could consider the entire system, the physical receiver plus the numerical analysis, as an entire linear operation (which turns out to be very close to matched filtering) on the input signals. Alternatively, the characteristics of the receiver output voltage might be determined, and then the well-developed techniques of spectral analysis applied to the rest of the problem. Mainly because there is no longer any control over the receiver output signal which is recorded on magnetic tape, the latter approach is the most reasonable, although the nature of the entire processing of the echoes is also interesting.

Because the energy spectrum of each echo is computed, it is the most important characteristic of the noise passed through the receiver in determining the effect of noise on the measurement of the echoes. The energy rather than the power spectral density is the appropriate quantity here because the receiver is "on" only for the duration of mixing sweep and the Fourier analysis only extends over a finite time limited to the length of the transmitted signal. The energy spectrum of the noise passed through the receiver is also a random quantity which depends on the particular configuration of the input noise during the receiving interval, and changes from pulse to pulse. The echoes and noise are independent so their energy spectra can be computed separately and then summed.

In computing the energy spectrum of the receiver output noise, the details of the operation of the receiving system must be carefully considered. Two frequency translations besides the heterodyning with the delayed chirp are accomplished, and the mixing frequency for the second one is centered in the 2-kHz-wide IF band. The passbands of the preamplifiers or converters used before mixing with the delayed chirp were greater than 1 MHz and thus much larger than the spectrum of the chirps. Since the latter is confined very closely to the 100 kHz sweep width, one intuitively expects the characteristics of the noise passed through a narrow filter after this mixing to be invariant across the sweep time interval.

Because we are dealing with narrowband signals and frequency translations, the "analytic signal" formulation in terms of complex envelopes [Helstrom, 1960; Berkowitz, 1965] is very convenient here. Using this concept, a real signal $s(t)$ can be written as

$$s(t) = \text{Re}\ S(t)\ \exp(j\omega_o t)$$

where Re indicates "the real part of." The complex envelope $S(t)$ is the transform of twice the positive frequency part of the Fourier spectrum of $s(t)$, $S(f)$, shifted from ω_o to zero frequency. The choice of ω_o is arbitrary, but it is usually chosen in the band occupied by the real signal. $\tilde{S}(f)$ is the transform of $S(t)$; and if the spectral extent of $\tilde{S}(f)$ is much smaller than ω_o, $S(t)$ varies slowly compared to $\exp(j\omega_o t)$, so it behaves like an envelope. The same development can be made for filters, and a complex-envelope impulse response and a narrowband frequency response can be defined in the same way. Going further, for narrowband noise signals the complex envelope for the autocorrelation function, $\tilde{R}(\tau)$, is related to the real autocorrelation by $R(\tau) = \text{Re}\ \tilde{R}(t)\ \exp(j\omega_o\tau)$ and to the narrowband power spectrum by

$$\tilde{\Phi}(\omega) = \frac{1}{2}\int_{-\infty}^{\infty} \tilde{R}(\tau)\ e^{-j\omega\tau}\ d\tau$$

First consider the heterodyning of the input with the delayed chirp, $m(t) = \cos(\xi t^2 + \omega_1 t + \emptyset)$ for $0 < t < T$, and zero otherwise. The complex envelope of $m(t)$ based on ω_1 is

$$M(t) = \begin{cases} \exp[j(\xi t^2 + \emptyset)] & 0 < t < T \\ 0 & \text{otherwise} \end{cases} \tag{2.5}$$

Similarly, the input noise, which is in a band centered at ω_o, is written in terms of its complex envelope $N(t)$, where $\overline{\frac{1}{2}N(t)\ N^*(t+\tau)} = \tilde{R}_n(\tau)$ is the complex envelope of the autocorrelation function $R_n(\tau)$.

The output of the mixer is $z(t) = M(t) \times n(t)$, so the complex envelope of the difference frequency (with a "carrier" at $\omega_1 - \omega_o$) component of $z(t)$ is

$$Z_\triangle(t) = \frac{1}{2}M(t)\ N^*(t) \tag{2.6}$$

and its narrowband spectrum is

$$\tilde{Z}_\triangle(f) = \frac{1}{2}\int_0^T M(t)\ N^*(t)\ e^{-j\omega t}\ dt \tag{2.7}$$

The energy spectral density of the complex envelope is therefore

$$|\tilde{Z}_\triangle(f)|^2 = \frac{1}{4}\int_0^T M(\sigma)\ N^*(\sigma)\ e^{-j\omega\sigma}\ d\sigma \times \int_0^T M^*(\rho)\ N(\rho)\ e^{j\omega\rho}\ d\rho$$

$$= \frac{1}{4}\iint_0^T M(\sigma)\ M^*(\rho)\ N(\rho)\ N^*(\sigma)\ \exp[-j\omega(\sigma - \rho)]\ d\sigma\ d\rho \tag{2.8}$$

Taking the mean value,

$$\overline{|\tilde{Z}_\triangle(f)|^2} = \frac{1}{4}\iint_0^T \exp[j\xi(\sigma^2 - \rho^2)]\ \overline{N(\rho)\ N^*(\sigma)}\ \exp[-j\omega(\sigma - \rho)]\ d\sigma\ d\rho \tag{2.9}$$

Now, $\overline{N(\rho)\, N^*(\sigma)} = 2\widetilde{R}_n(\rho-\sigma)$ [Helstrom, 1965]. Since the bandwidth of the noise is much wider than that of $M(t)$, $\widetilde{R}_n(\rho-\sigma)$ is very narrow compared to the interval required for a significant change in the exponential term of Eq. (2.9), so the contribution to the integral is confined to a very small range around $\sigma - \rho = 0$. Therefore, with only a small error at the lower frequencies, we can reasonably assume that the noise is white with power spectral density $N_o/2$, so $\widetilde{R}_n(\tau) = N_o\delta(\tau)$. Equation (2.9) then becomes

$$\overline{|\widetilde{Z}_\triangle(f)|^2} \cong \frac{1}{2} \iint_0^T \exp[j\xi(\sigma^2 - \rho^2)]\, \exp[-j\omega(\sigma - \rho)]\, N_o\delta(\sigma - \rho)\, d\sigma\, d\rho$$

$$= \frac{N_o}{2} \int_0^T d\sigma = \frac{N_o}{2}\, T \tag{2.10}$$

and therefore the average energy spectral density of the complex envelope of the mixer output is also white. This result is only accurate for frequencies somewhat less than the spectral extent of $\widetilde{\Phi}_n(f)$, but since the mixer output is then passed through the 2-kHz-wide IF centered at the difference carrier $\omega_1 - \omega_o$, only a very small range of $\overline{|\widetilde{Z}_\triangle(f)|^2}$ near $f = 0$ is important, so it can accurately be considered flat across the IF bandwidth.

From this mixing process the signals are translated to the 456 kHz IF, which has a narrowband transfer function $H(\omega)$. The frequency translation does not affect the complex envelope, but $H(\omega)$ does; and at the IF output, the average energy spectral density is

$$\overline{|\widetilde{Y}(f)|^2} = |\widetilde{H}(f)|^2 \times \overline{|\widetilde{Z}_\triangle(f)|^2}$$

$$= \frac{N_o}{2}\, T\, |\widetilde{H}(f)|^2 \tag{2.11}$$

At this point the signal is mixed with another signal whose frequency is the same as the center frequency of the IF. The average energy spectral densities of the echoes and noise are depicted in Fig. 15 both before this final mixing (in the receiver IF) and after (at the receiver output) .

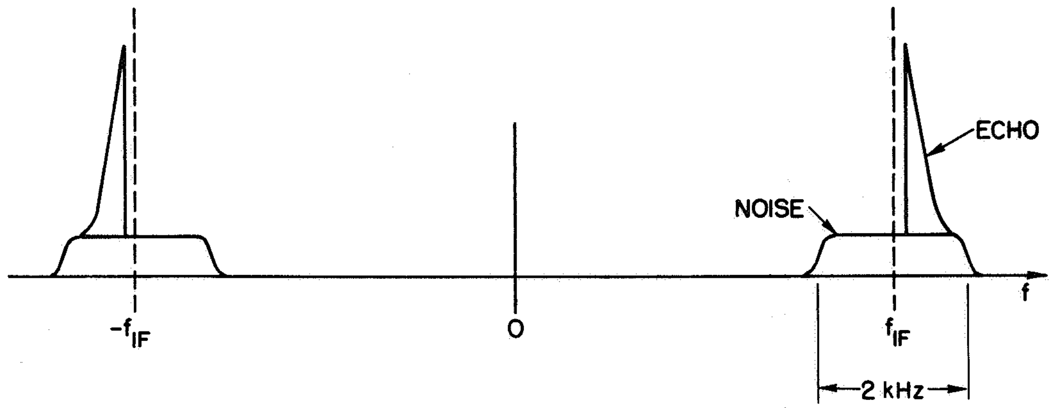

a. In the receiver IF

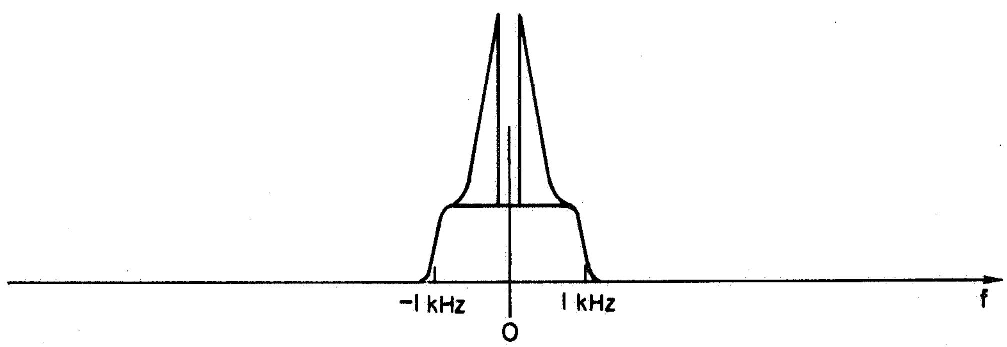

b. At the receiver output

Fig. 15. SPECTRUM OF ECHOES PLUS NOISE.

The echo is considerably exaggerated in width and reduced in amplitude, and the noise does not actually have such a flat spectrum. Unfortunately, the particular choice of the various mixing frequencies and the position of the echo in the IF passband cost 3 dB in signal-to-noise ratio at the output, because the noise energy spectral density is doubled. It would have been much better to place both the echo and the final mixing frequency at the edge of the IF passband.

D. Preliminary Data Processing--Spectral Analysis

The receiver output signals, which are bandlimited by the IF response to frequencies less than 1 kHz or so, were recorded along with several timing signals on 7-track magnetic tape at 3.75 ips. Both direct and FM recording modes were used for the 25 and 50 MHz channels, the FM mode to give better low-frequency performance and the direct mode for greater range depth (the 11.6 ms total range depth of the moon corresponds to 1.16 kHz, and at 3.75 ips the FM bandwidth is specified only to 625 Hz). The advantage of the FM mode was partially removed by the necessity for capacitive coupling to block the dc level of the receiver output, but the cutoff frequency was low enough to hardly affect the echoes at all. Although the response in the FM mode is only specified to 625 Hz, it is really a tolerance guarantee, and the actual response is much wider. Because the FM mode has a better characteristic than the direct one over the frequencies of greatest interest (the lower frequencies since the echo rapidly disappears into the noise with increasing range), all the data reduction was done on the FM recorded signals. A simple measurement of the spectral extent of FM recorded signals using a highpass filter showed that it cut off sharply at about 1.2 kHz, which is a strong indication that the frequency response of the receiver IF was the limiting process, and not the recording. The response of the entire system is easily determined from the measured output noise spectrum since the noise spectrum is known to be flat at the input.

Three timing signals were recorded. The most important was a square wave from the sweep timing synchronizer which changed levels when the approximately two and one-half transmit sweeps began and ended. Its length was the delay between the transmit and mixing sweeps and was adjusted for each run to about the expected minimum range delay to the leading edge of the echo. A short tone every 10 min and WWV signals were the other timing signals.

For the total electron content measurements, this recorded data was reduced by an analog spectral analyzer, whose output was filmed. Thus an easily interpreted record of every day's run was available, and particular runs could be carefully selected for more intensive analysis.

The selection was subjective, but was based on the general criteria of low "noisiness" and a strong signal near the zero doppler time, a minimum range neither too far nor too close to zero frequency, and regular Faraday fading. The run selected was that of 24 August 1965; but since the subradar point was computed to be in a mountainous region (about 5°S 1.5°W, between the craters Herschel and Spörer), the run of 20 August 1965--when the subradar point was in a relatively flat area near the crater Sömmering (1°N 7°W)--was also chosen to determine how much effect the topographical difference has on the leading edge of the echoes. There is a difference of several resolution cells between the ranges of the two positions, which have about the same altitude above the reference sphere.

The recorded signals were digitized using an analog-to-digital converting system consisting of a Packard-Bell M-2 Multiverter connected to an IBM 1620 computer, and the resulting three-decimal-digit samples were recorded on digital tape. Each receiving period became an individual record, which was written on the digital tape during the transmit period, the timing being controlled by the transmit-receive square wave recorded on the data tape. The effective sampling rate was derived from 1 and 10 kHz standard frequencies generated by a counter built into the A-D converter system, and could be adjusted somewhat by changing tape speeds and dividing the 10 kHz by 2 or 4. Two effective sampling rates were used: 1000 samples per second and 2500 samples per second. The first sampling rate was used to study the leading edge of the echoes with narrow range resolution, and the second was used to study the entire echo with less resolution.

Because the signals were bandlimited to frequencies below about 1.2 kHz, the 2.5 kHz sampling rate insures that there will be little difficulty with aliasing because it is above the Nyquist rate. With the 1 kHz sampling rate, however, a lowpass filter set at about 300 Hz had to be used to eliminate this problem. Above 500 Hz, the response of this filter is more than 30 dB below the dc level, and falls at a rate of -18 dB per octave.

The next step in the processing is the spectral analysis. This was done initially on the Stanford Computation Center's IBM 7090 computer, and later, on its replacement, an IBM 360/67 system, using the "fast Fourier transform" (FFT) algorithm.† The FFT is a rapid computational procedure for calculating the finite Fourier transform of a time series. When the time series is composed of sample values of a continuous function, the finite Fourier transform and the Fourier transform of the continuous function are closely related.

The finite Fourier transform X_n of the series x_k of length N is defined by

$$X_n = \frac{1}{N} \sum_{k=0}^{N-1} x_k \exp\left(-j \frac{2\pi}{N} nk\right) \tag{2.12}$$

and the FFT yields N values of X_n If the time series is the sample (at spacing $\Delta t = 1/F$ values of the aliased version of $x(t)$ in the interval $0 < t < T$ defined by

$$x_p(t) = \sum_{\ell=-\infty}^{\infty} x(t + \ell T)$$

and the sampled (at spacing $\Delta f = 1/T$) aliased version of the Fourier transform of $x(t)$ is

$$X_p(n\Delta f) = \sum_{m=-\infty}^{\infty} X(n\Delta f + mF)$$

then $X_p(n\Delta f)$ is the finite Fourier transform of $Tx_p(k\Delta t)$ [Cooley et al, 1967]. Therefore, if $X_p(f)$ is equal to $X(f)$ in the range $-F/_2 < f < F/2$, the finite Fourier transform yields accurate sample values of $X(f)$. This requires that $X(f)$ be bandlimited at $F/2$, as illustrated in Fig. 16. The FFT computes values of $X_p(f)$ between zero and F, but it is clear that the positive frequency part of $X(f)$ lies in the range $0 < f < F/2$ and the negative part in $F > f > F/2$.

† See special issue of IEEE Transactions on Audio and Electroacoustics, AU-15, 2, Jun 1967.

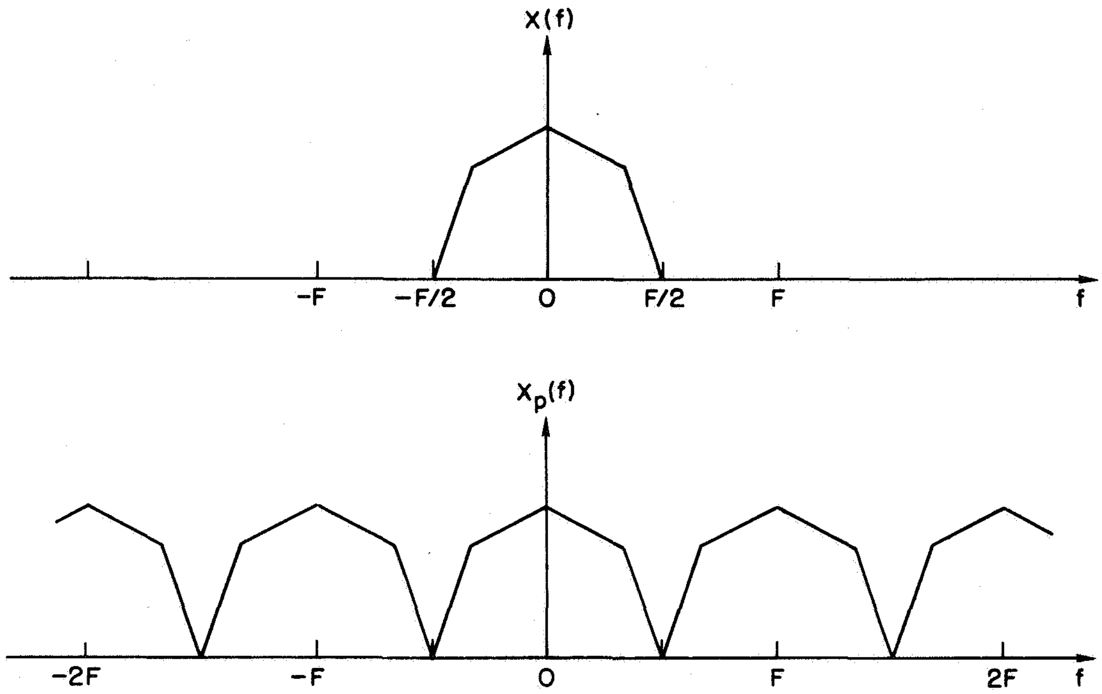

Fig. 16. RELATIONSHIP BETWEEN THE SPECTRUM OF A BANDLIMITED FUNCTION, $X(f)$, AND ITS ALIASED VERSION, $X_p(f)$, WHEN SAMPLING IS DONE AT THE NYQUIST RATE.

The spacing Δf of the $X_p(f)$ samples can easily be controlled when $x_p(k\Delta t)$ is formed by adjusting the parameter $T = N\Delta t$. It is not necessary that $N\Delta t$ just encompass the nonzero extent of $x(k\Delta t)$. If it is made larger by adding zeros to the series, the spacing will be less than it would be if only the nonzero extent is used, which would result in a spacing exactly at the "Nyquist rate" for spectra. To use the FFT, N should be an integral power of 2, so zeros were added to the lunar echo data analyzed here to obtain a proper value of N. For the narrow range resolution study, enough zeros were added to reduce the interval to less than half the ordinary spacing in order to resolve the leading edge spike more accurately.

Use of the FFT on each echo leads directly to an estimate of the energy spectral density $|X(f)|^2$ of the echo's particular combination of noise and echo signals, and averaging many echos will presumably be a close estimate of the power vs range curve of the lunar backscattering.

This is essentially the same problem as trying to estimate the power spectral density of a continuous signal when the maximum record length T that can be analyzed is limited. It makes no difference that the records are not contiguous. The basic assumption made here is that the statistics of the scattering behavior are stationary; this is the same assumption made in the estimation of a power spectrum, so the finite duration echo can be considered to be a piece of a signal which possesses a power spectrum. This is not to say that the sweep has an infinite duration, but rather, that the average scattering characteristics are frequency independent and the receiver output signal can be considered as a sample of a stationary process.

Power spectra can be estimated from the periodogram, $P = (1/T)|X(f)|^2$ (or a modified version of it). Even in the limit as $T \rightarrow \infty$, P is generally a very badly behaved function, with a variance often approximately equal to the square of its expectation. Its ensemble average, $(1/T)\overline{|X(f)|^2}$, however, is well behaved and does equal the power spectral density $\Phi(f)$.

It makes no difference computationally whether the spectral estimates are called "energy spectra" or "power spectra," but for ease in comparing estimates with different values of T, and to conform with other lunar radar studies, the "power" terminology will be used.

Because it is impossible to measure a power spectral density from a finite length of data, the best one can do is to obtain a weighted average of the spectrum over a finite bandwidth around the frequency where it is being estimated [Blackman and Tukey, 1958]. The weighting function, called a "spectral window," can be controlled by modifying the data with a "data window."

Let the data window be $w(t)$, which is zero outside the interval 0 to T. Then the modified periodogram is computed from the weighted sampled data, $w(k\Delta t)\ x(k\Delta t)$, through the finite Fourier transform

$$X_f(n\Delta f) = \frac{1}{T} X_p(n\Delta f) = \frac{1}{N} \sum_{k=0}^{N-1} [w(k\Delta t)\ x(k\Delta t)]_p \exp\left(-j\,\frac{2\pi}{N}\,kn\right) \qquad (2.13)$$

The modified periodogram, which is the estimator of the power spectrum of x, $\Phi(f)$, is

$$\hat{P}(n\Delta f) = \frac{T}{U} \left| X_f(n\Delta f) \right|^2 = \frac{1}{TU} \left| X_p(n\Delta f) \right|^2 \tag{2.14}$$

where $T = N\Delta t$ = record length, and U is a normalizing constant. Then the expected value of $\hat{P}(n\Delta f)$ can be shown to be (see Appendix A)

$$\overline{\hat{P}(n\Delta f)} = \int_{-\infty}^{\infty} \frac{1}{TU} \left| W_p(f') \right|^2 \Phi(n\Delta f - f')\, df'$$

$$= \int_{-\infty}^{\infty} H(f')\, \Phi(n\Delta f - f')\, df' \tag{2.15}$$

$H(f)$ is the spectral window and is aliased at an interval of $F = 1/\Delta t$:

$$H(f) = \frac{1}{TU} \left| W_p(f) \right|^2 = \frac{1}{TU} \left| \sum_{\ell = -\infty}^{\infty} W(f + \ell F) \right|^2 \tag{2.16}$$

There are two general criteria for choosing a particular form for $w(t)$. The area under $|W(f)|^2$ should be concentrated in a narrow mainlobe around $f = 0$; and the sidelobes, which are impossible to eliminate since $w(t)$ is truncated, should be small and decrease with frequency. Three commonly used spectral windows are shown in Fig. 17a-c, plotted in decibel power response as a function of $f \times T$. The first is the "do nothing" window,

$$w(t) = 1 \quad \text{and} \quad W(f) \sim \text{sinc}^2\, (\pi f T)$$

Because the sidelobes are so high, this is not a very useful window, even though it has a very narrow mainlobe. The other two examples are more practical. That of Fig. 17b is the triangular data window,

$$w(t) = \frac{1 - 2\, |t - T/2|}{T} \quad \text{and} \quad W(f) \sim \text{sinc}^4 \left(\frac{\pi f T}{2}\right)$$

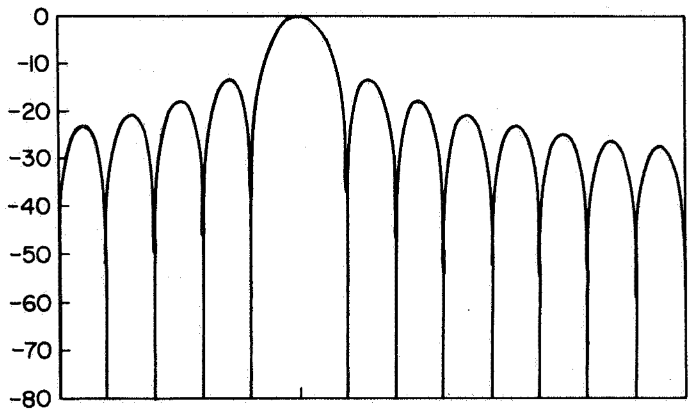

a. "Do nothing" window--$|W(f)|^2 \sim \mathrm{sinc}^2\ (\pi fT)$

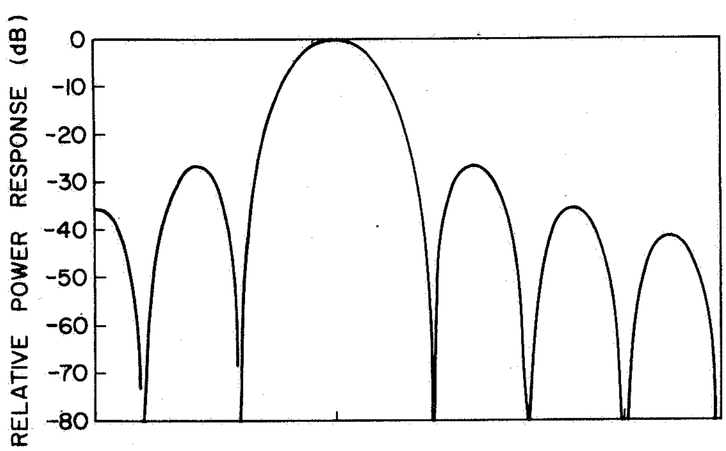

b. Triangular data window--$|W(f)|^2 \sim \mathrm{sinc}^4\ (\pi fT/2)$

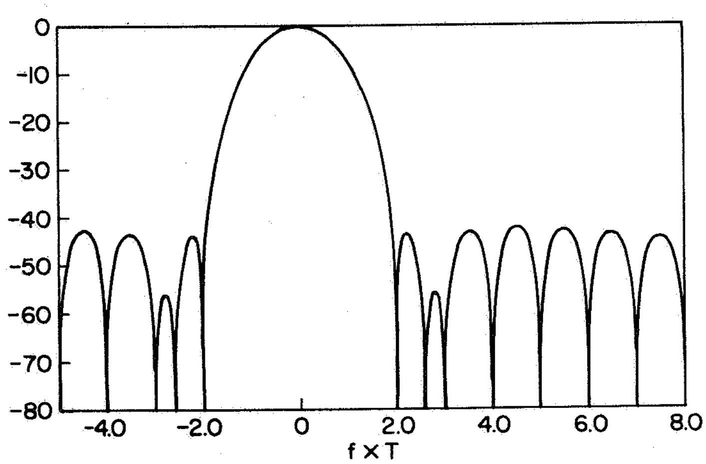

c. "Hamming window"

Fig. 17. SPECTRAL WINDOWS.

The last example is the "hamming" window [Blackman and Tukey, 1958],

$$w(t) = 0.544 - 0.456 \cos\left(\frac{2\pi t}{T}\right)$$

Another useful window is the "hanning" window,

$$w(t) = 0.5 - 0.5 \cos\left(\frac{2\pi t}{T}\right)$$

which is very similar to the hamming window except that the sidelobes decrease more rapidly although the largest sidelobe is bigger. Both the hamming and hanning windows were used here, the former for the high resolution extended-range analysis.

For useful windows, the width of the mainlobe is about 2/T, and since the aliasing period in $H(f)$ is $F = N/T$, the shape of the mainlobe of $H(f)$ is only very slightly different from that of $|W(f)|^2$ since $N \gg 2$.

When $\Phi(f)$ is bandlimited to $|f| < F/2$, only the first lobe of $H(f)$ contributes to $\overline{\hat{P}(n\Delta f)}$ in Eq. (2.15), thus

$$\overline{\hat{P}(n\Delta f)} = \int_{-F/2}^{F/2} H(f') \, \Phi(n\Delta f - f') \, df' \tag{2.17}$$

The normalizing factor U is chosen to make $\overline{\hat{P}(n\Delta f)} = \Phi(n\Delta f)$ when $\Phi(f)$ is a constant, so

$$U = \frac{1}{T} \int_{-F/2}^{F/2} |W_p(f)|^2 \, df = \frac{1}{N} \sum_{k=0}^{N-1} w^2(k\Delta t)$$

and

$$\int_{-F/2}^{F/2} H(f) \, df = 1$$

but U is unimportant when relative power density estimates are all that is desired and the normalization can be ignored.

The variance of the estimate $\hat{P}(f)$ is generally very high; for a gaussian process where $\Phi(f)$ is flat over the passband of the estimator,

$$\frac{\mathrm{Var}\,\{\hat{P}(f)\}}{\overline{\hat{P}(f)}^2} = 1$$

However, if the estimate is made by the average of K modified periodograms formed from different sections of the data,

$$\hat{P}_a(n\Delta f) = \frac{1}{K} \sum_{k=1}^{K} \hat{P}_k(n\Delta f)$$

The estimate is more stable, with [Welch, 1967]

$$\frac{\mathrm{Var}\,\{\hat{P}_a(f)\}}{\overline{\hat{P}_a(f)}^2} = \frac{1}{K} \tag{2.18}$$

When there are several discrete stationary targets with no range depth, the equivalent $\Phi(f)$ will consist of δ-functions, which can be resolved only if their spacing is sufficiently large. Since the response to two such targets at f and $f + \delta f$ is just $H(f)$ and $H(f + \delta f)$ according to Eq. (2.15), we choose the integral of the squared difference of the responses as a measure of the resolution, so

$$\epsilon = \int_{-\infty}^{\infty} [H(f) - H(f + \delta f)]^2 \, df$$

$$= 2 \int_{-\infty}^{\infty} H^2(f) \, df - 2 \int_{-\infty}^{\infty} H(f) \, H(f + \delta f) \, df \tag{2.19}$$

The first term is a constant so we want to minimize the second to maximize ϵ, so

$$\Gamma(\delta f) = \int_{-\infty}^{\infty} H(f)\ H(f + \delta f)\ df$$

$$= \int_{-\infty}^{\infty} W(f)\ W^*(f + \delta f)\ W^*(f)\ W(f + \delta f)\ df \qquad (2.20)$$

is the measure of resolution. Now, $\Gamma(\delta f)$ behaves like the ambiguity function of radar signals [Berkowitz, 1965], with a peak at $\delta f = 0$; and in the region where it is large, resolution is poor. The width ΔF of a rectangle of height $\Gamma(0)$ and area equal to that of $\Gamma(\delta f)$ is a measure of the extent of this region, and can be expressed by

$$\Delta F = \frac{\int_{-\infty}^{\infty} \Gamma(\delta f)\ d(\delta f)}{\Gamma(0)} \qquad (2.21)$$

From Eq. (2.20),

$$\int_{-\infty}^{\infty} \Gamma(\delta f)\ d(\delta f) = \int_{-\infty}^{\infty} |R(\delta f)|^2\ d(\delta f) \qquad (2.22)$$

where

$$R(\delta f) = \int_{-\infty}^{\infty} W(f)\ W^*(f + \delta f)\ df$$

$$= \int_{-\infty}^{\infty} w^2(t)\ e^{-j\delta\omega}\ dt$$

After a little manipulation,

$$\Delta F = \frac{\int_{-\infty}^{\infty} |R(\delta f)|^2 \, d(\delta f)}{|R(0)|^2}$$

$$= \frac{\int_{-\infty}^{\infty} w^4(t) \, dt}{\left[\int_{-\infty}^{\infty} w^2(t) \, dt\right]^2} = \frac{1}{T_e} \tag{2.23}$$

where T_e is the "effective length" of the record. For the hamming and hanning windows, T_e is 0.61 T and 0.55 T, respectively, so the maximum available range resolutions (when T = 1 sec) are 18.1 and 19.4 μs, remembering that 1 Hz is equivalent to 10 μs of range delay.

The signals are actually a combination of background noise and the expected and depolarized components of the echo, whose spectra simply add if the two echo components are assumed to be uncorrelated (this assumption will be discussed later). Thus the effect of these three signals on the estimates can be considered separately.

The resolution of the estimates can be easily adjusted by varying the window parameter T and splitting each 1 sec echo into several pieces. This adjustment reduces the variance-squared mean ratio of all three parts of the estimates by the same amount, which is the number of pieces according to Eq. (2.18), if the number of echoes analyzed remains constant. The processing time will be slightly less, however, and would be considerably less if the variance-squared mean ratio is kept constant by analyzing fewer echoes.

Figure 18 shows a typical sequence of echo spectra at maximum resolution. The high variability can easily be seen. Thirty minutes of these spectra (about 400 for each wavelength) are plotted in Fig. 19a,b, where the relative amplitudes, in decibels, of the spectra are denoted by a range of spot sizes. These figures can be directly compared to Fig. 13, which presents the analog spectral analysis output in essentially the same way, since all are from the run of 24 August 1965.

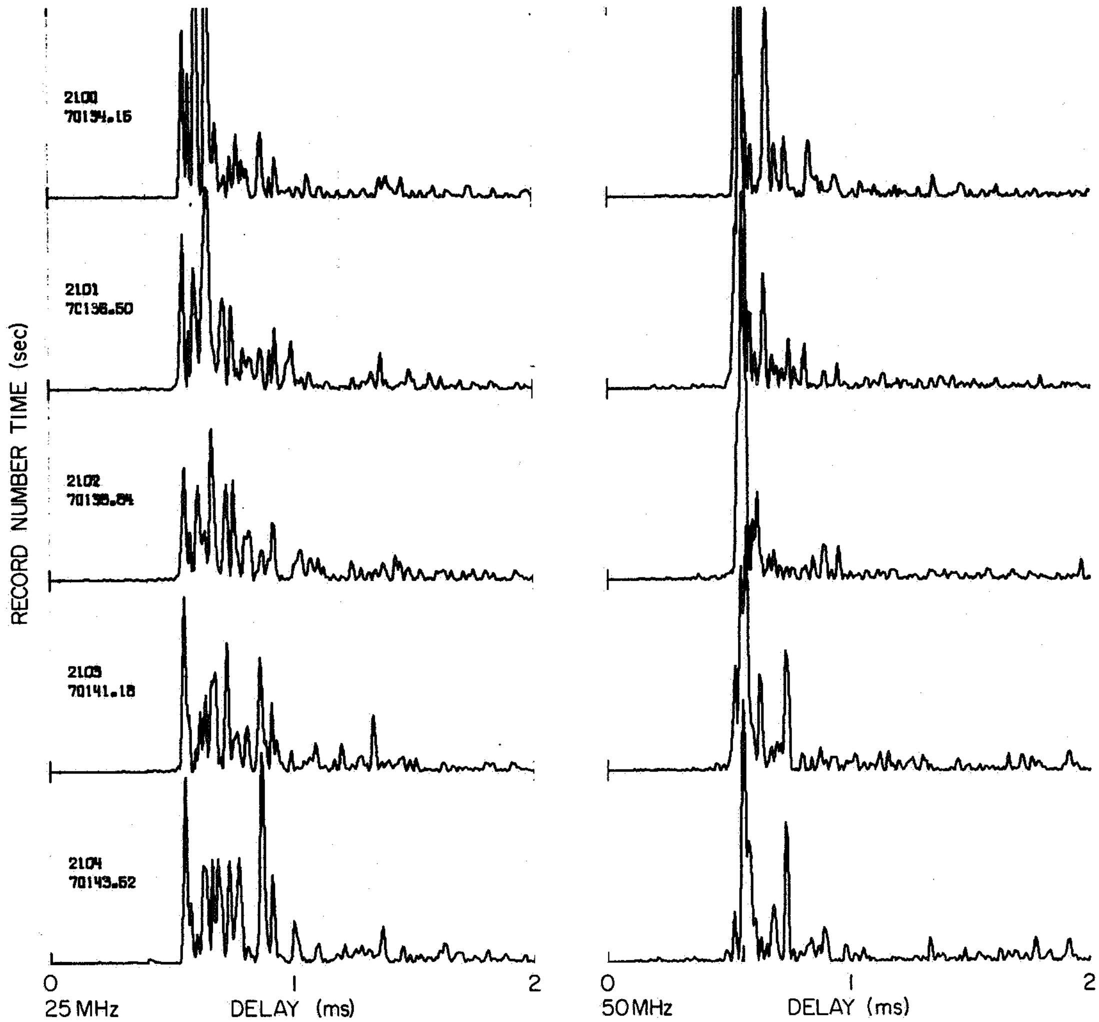

Fig. 18. A TYPICAL SEQUENCE OF ECHO SPECTRA. Maximum resolution; 2 ms range delay intervals; 25 MHz echoes on left, 50 MHz echoes on right.

Only the second of the two and one-half transmitted chirps was used for analysis since it was the only complete sweep and therefore the only one that could give the maximum resolution. It was isolated by placing the data window on the second 1 sec interval of the digitized records.
one that could give the maximum resolution. It was isolated by placing
was not exactly the transmitting time interval, and because passing the signals through the various filters spreads them out in time so some part of the adjacent half sweeps corrupts the output from the center one. The error between the delay time and the transmitting time interval is very

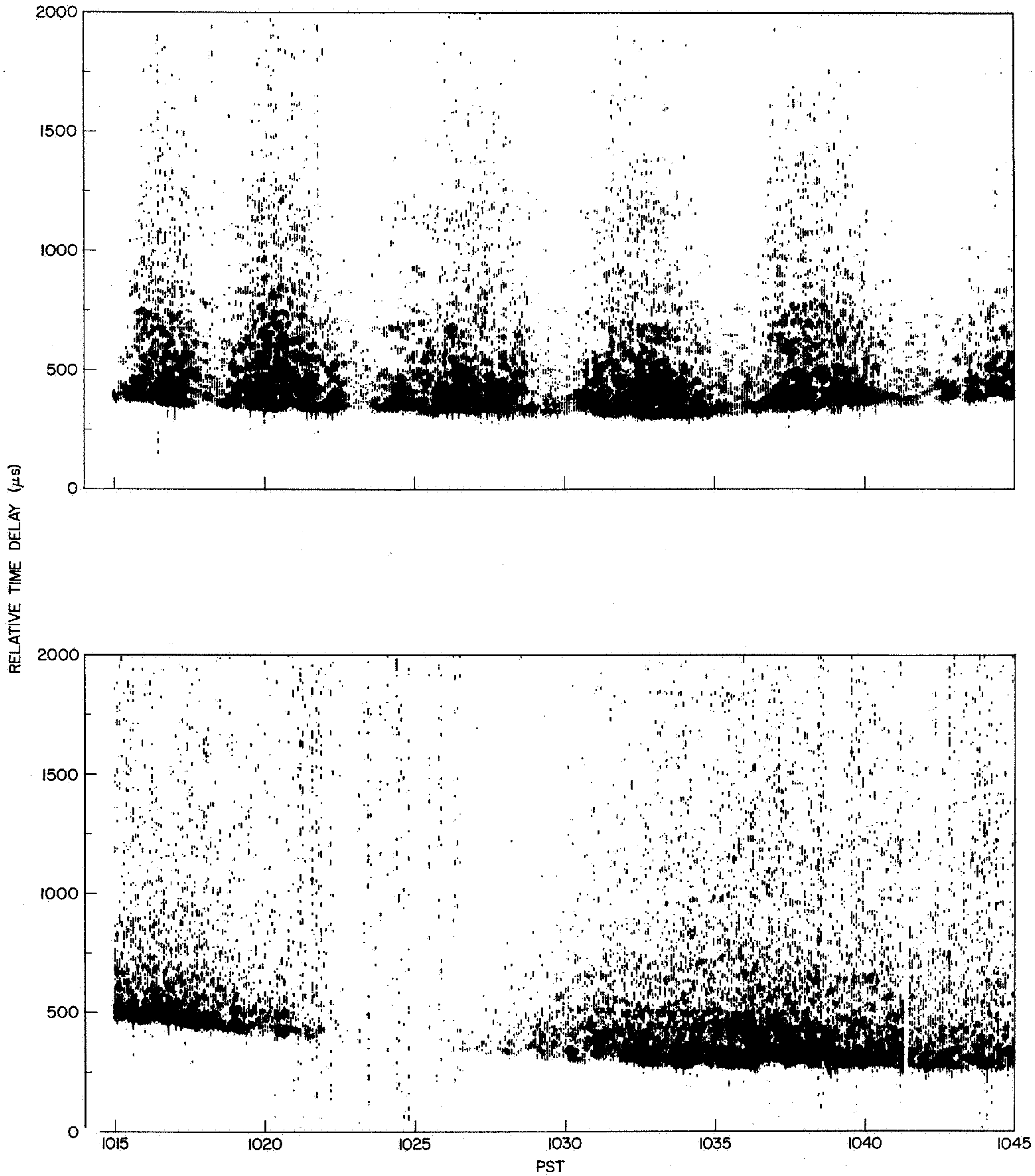

Fig. 19. ECHO POWER VS RANGE AS A FUNCTION OF TIME WITH MAXIMUM RESOLUTION AND 2.25 ms RANGE DELAY INTERVAL. (a) 25 MHz data; (b) 50 MHz data.

small, no more than 10 ms out of the 1 sec sweep duration. The time spreading from the filters is also small because the filter bandwidths are much larger than the inverse of the sweep lengths; this error is further reduced by the low values of the data window at its edges.

Figure 20 is the same as Fig. 19 except that the range and range-rate changes of the moon have been removed by shifting the spectra according to the curve computed from the ephemeris. Also, the range interval is much smaller in order to expand the detail at the leading edge. The irregular libration fading is clearly slower and deeper near the leading edge, and appears to be twice as fast at 6 m than at 12, as expected. The notched appearance of the leading edge is also due to libration fading, and occasionally returns can be seen 30 μs ahead of the "peak," which is reasonable considering the roughness of the region around the subradar point. The subradar point was near the crater Herschel which has a range depth of 26 μs from rim to floor.

The Faraday fading makes it impossible to simply average the spectra and get the mean scattering behavior. After the Faraday effects are carefully measured, however, they can be compensated for and a more complicated form of the averaging performed. The method and results will be presented in Chapter IV after the ionospheric effects are considered.

Because of the equivalence between frequency and time delay, the combination of mixing the received echoes with a chirp and then spectrally analyzing the result is very similar mathematically to correlating the echoes with a series of delayed chirps, when the envelope of the correlation is obtained. The total range of equivalent delays is very small compared to the signal duration so the comparison is accurate when the doubling of the spectral density of the background noise due to the various frequency translations is included.

E. Range Resolution--Comparison to Regular Short-Pulse Studies

The range resolution capabilities of a transmitted radar waveform are generally specified by the ambiguity function, which is the squared magnitude of the combined (both time and frequency shifts) correlation function of the transmitted signal's complex envelope [Berkowitz, 1965].

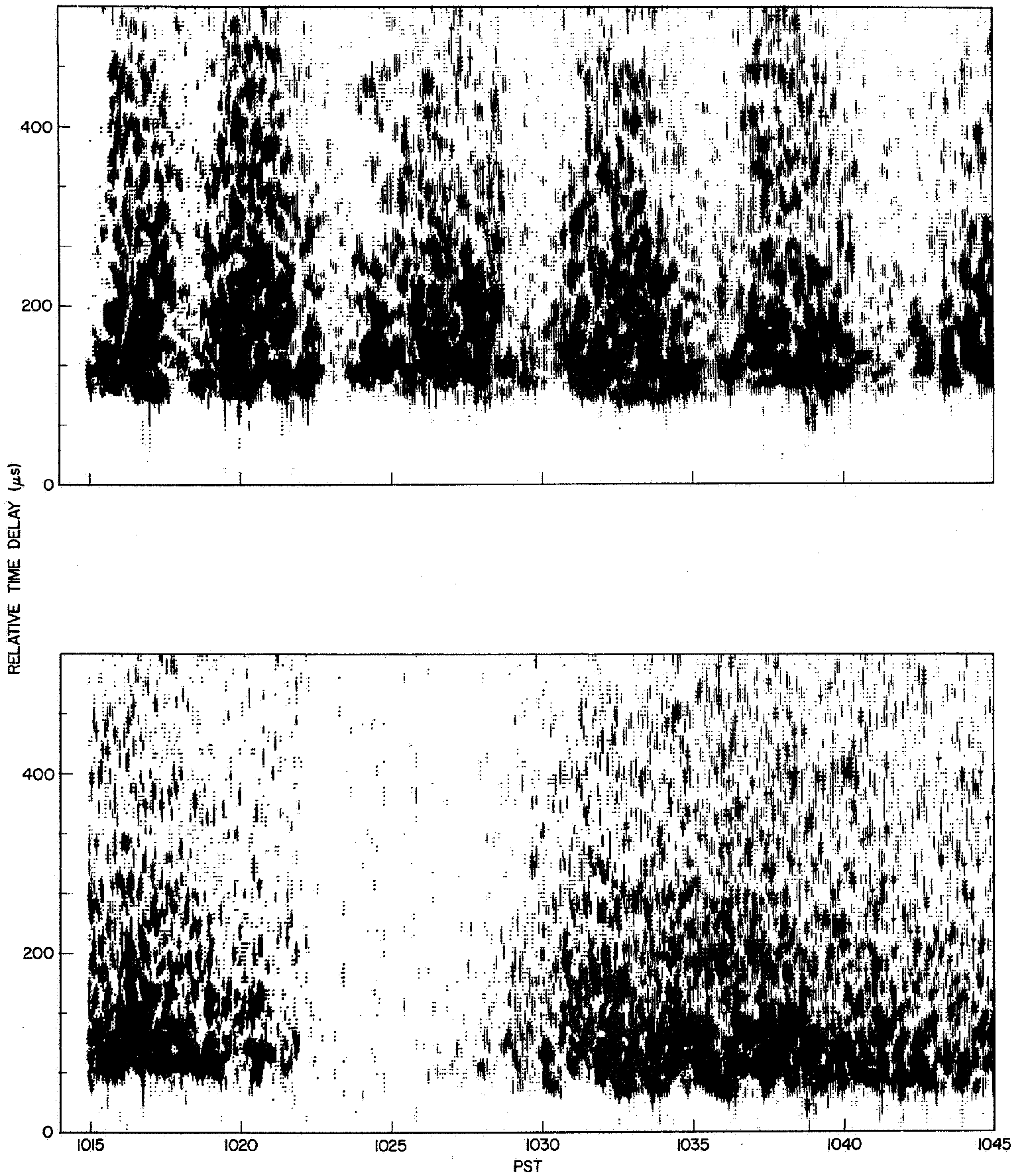

Fig. 20. ECHO POWER VS RANGE AS A FUNCTION OF TIME WITH MAXIMUM RESOLUTION AND 600 ms RANGE DELAY INTERVAL. (a) 25 MHz data; (b) 50 MHz data.

A delay resolution constant $\Delta\tau$ can be defined from the squared magnitude of the ambiguity function in the same way that ΔF was specified from $H(f)$ in the preceding section. Indeed, ΔF was purposely specified in that way so it would be exactly equivalent to $\Delta\tau$ when interpreted as a range interval.

This comparison is justified because $H(f)$ and the squared magnitude of the ambiguity function both state, in terms of power response, how well echoes at slightly different ranges can be distinguished. Since the short-pulse observations of the moon have usually been made by taking the square of the output of a matched filter, whose squared envelope is equal to the ambiguity function (actually, of the complex-envelope's autocorrelation function, which is a cross section through it at zero frequency shift), this is the proper way to view resolution for comparison purposes. Exact matched filtering was not used here because it leads to high sidelobes in the response. The "do nothing" spectral window corresponds exactly to the matched filter for chirp signals, so its $H(f)$ is the ambiguity function along the range axis. At the cost of slightly less resolution and sensitivity, the echoes were modified by $w(t)$, which is nearly the same as using a slightly mismatched filter designed to reduce the sidelobes, a common chirp-radar technique [Berkowitz, 1965].

Except at 3.6 cm where an FM pulse compression ratio of 10 was used, rectangular envelope pulses were used for the previous lunar radar studies. The autocorrelation function of this envelope is triangular in shape, and $\Delta\tau$ is equal to the pulse length. A wide variety of pulse lengths have been used, as can be seen from Table 1. Matched filtering was not used with all pulse lengths in those studies, but the filters were generally wider than the pulse bandwidth, so the inherent resolution of the pulse was preserved. For most of the studies, the echoes were range gated and integrated before sampling, which changes the resolution to approximately the sum of the pulse length and the gate width. Only at 23 and 600 cm was the matched filter output directly sampled. The various combinations of pulse lengths, filter bandwidths, and range gate widths are summarized in Table 1, along with the maximum resolution.

The maximum resolution which could have been obtained here by using the "do nothing" window is equal to that of the 10 μs pulse width at

23 cm. Actually, this resolution could not have been obtained because of ionospheric effects which tend to broaden the spectral window. The measurements made here using the windows with better sidelobe behavior have nearly the same maximum resolution (20 μs) as the 10 and 68 cm work. Maximum resolution processing was done on the data sampled at the lower rate, and a resolution of about 200 μs was used on the full range depth analysis. This figure was chosen as a compromise between range resolution, variance, processing time, and ionospheric effects, which are discussed in the next chapter. It was obtained by using the hanning window and splitting each echo into 10 sections. The entire angular spectrum can be obtained by combining the high and low resolution results, and a comparison to the other work at different pulse lengths can be made by suitably averaging the high resolution data over range intervals near the leading edge of the echo.

Chapter III

EFFECTS OF THE IONIZED REGIONS

A. Introduction and Elements of the Magnetoionic Theory

While both the ionsophere and the cislunar medium have about the same columnar electron content [Howard, 1966], the ionosphere has a much more significant effect on the propagation of the lunar radar signals. It also has a much higher concentration of electrons than the regions farther away from the earth--which makes dispersive and refractive effects important there--and it also is birefringent due to the geomagnetic field. This latter characteristic is responsible for the Faraday rotation of a linearly polarized wave, which is the most important effect of the media on the radar signals studied here. The other effects [Lawrence et al, 1964], such as group delay, attenuation, refraction, scintillation, dispersion, and doppler excess, are potentially important; however, our analysis will show that they are either unimportant or otherwise easily accounted for. The most difficult to deal with are the attenuation and irregular refraction and scintillation properties because they cannot be measured from these data; however, the former only affects the total radar-cross-section measurement which already has poor accuracy, and the latter can be minimized by choosing data carefully.

Ionospheric effects, especially Faraday rotation, have made lunar radio studies difficult, particularly at decametric wavelengths. For this reason the effect of Faraday rotation on a wideband signal in a dispersive medium will be considered very carefully here. To overcome the Faraday effect, investigators have often used circular polarization (see Table 1); but when only linear polarization was available or desirable, measurements were limited to the peak periods of the Faraday fading cycle [Davis and Rohlfs, 1964], or at the shorter wavelengths where it would be feasible, the polarization plane of the receiving antenna was rotated to match that of the incoming signal [Evans and Hagfors, 1966]. Scintillation effects are usually minimized by choosing quiet days; and refractive effects, which are important at large zenith angles, can be adjusted for by antenna steering.

After the slow fading of lunar radar echoes was shown to be caused by the Faraday effect [Murray and Hargreaves, 1954], much use has been made of the phenomenon to measure the electron content of the ionosphere that contributes most of the effect [Evans, 1957; Millman, 1964]. Artificial satellite radio signals have been used in the same way [Garriott, 1960]. Other distortions of lunar radar echoes due to the ionized regions [Eshleman et al, 1960] between the observer and the moon have been used to measure the characteristics of those regions [Yoh et al, 1966]. Indeed, the use of lunar radar echoes for measuring the electron content was the primary motivation for collecting the data used in this study.

In the discussion of the results of the magnetoionic theory applied to the ionosphere and the regions beyond, the following symbols will be used:

n = refractive index

μ = real part of n

$X = (\omega_N/\omega)^2$

$Y_L = (\omega_H/\omega) \cos\theta$

$Y_T = (\omega_H/\omega \sin\theta$

$Z = \nu/\omega$

$\omega = 2\pi f$ = angular frequency of wave

$k = 2\pi/\lambda = \omega n/c$ = wave number

$\omega_N = 2\omega f_N$ = angular plasma frequency $= \sqrt{Ne^2/\epsilon_o m}$

$\omega_H = 2\pi f_H$ = angular electron gyrofrequency $(\mu_o H_o |e|)/m$

ν = effective collision frequency between electrons and heavy particles

N = electron density, electrons/m^3

H_o = geomagnetic field intensity, amperes/m

θ = angle between wave normal and $\vec{H}_o$

e = electronic charge $= -1.602 \times 10^{-19}$ coulomb

m = mass of electron = 9.109×10^{-31} kg

ϵ_o = permittivity of free space = 8.85×10^{-12} farad/m

μ_o = permeability of free space = $4\pi \times 10^{-7}$ henry/m

The complete Appleton-Hartree formula for the complex refractive index of an ionized region permeated by a static magnetic field is given by [Ratcliffe, 1959]

$$n^2 = 1 - \left\{ 1 - iZ - \frac{Y_T^2}{2(1 - X - iZ)} \pm \left[\frac{Y_T^4}{4(1 - X - iZ)^2} + Y_L^2 \right]^{1/2} \right\}^{-1} \qquad (3.1)$$

Each of the two values for n corresponds to a plane "characteristic wave," which propagates with no change in polarization, defined for the z-axis along the wave normal by

$$R = \frac{E_x}{E_y} = \frac{-i}{1/L} \left[\frac{Y_T^2}{2(1 - X - iZ)} = \left(\frac{Y_T^4}{4(1 - X - iZ)^2} + Y_L^2 \right)^{1/2} \right] \qquad (3.2)$$

The polarization is elliptical in general, but when the wave normal is parallel to the magnetic field, $Y_T = 0$ and $R = \pm i$, so the two characteristic waves are oppositely circularly polarized. If the wave frequency is sufficiently high, this result is approximately true even if Y_T is finite and the wave normal is not too near to being perpendicular to the magnetic field.

For the ionospheric conditions encountered and for the frequencies used in lunar radar studies at Stanford, the so-called "high-frequency, quasi-longitudinal" approximation is valid since in the worst case Z is negligibly small ($< 10^{-5}$) and X and Y are small quantities ($< 10^{-1}$) [Yoh, 1965]. Also, it is necessary that $Y_L^2 \gg Y_T^4/[4(1 - X - iZ)^2]$, which requires that $\theta < 88°$, a condition very easily fulfilled since the propagation is nearly longitudinal (Fig. 21). Under this approximation Eq. (3.1) reduces to

$$n^2 \cong 1 - \frac{X}{1 \pm Y_L} \tag{3.3}$$

and Eq. (3.2) becomes $R \cong \mp i$ which shows that the two characteristic waves are nearly circularly polarized. Since Y_L and X are much less than unity, Eq. (3.3) leads to

$$n_{\pm} = \mu_{\pm} \cong 1 - \frac{1}{2}X(1 \mp Y_L) \tag{3.4}$$

with the upper sign corresponding to the "ordinary" characteristic wave and the lower to the "extraordinary" wave. Note that under the high-frequency,

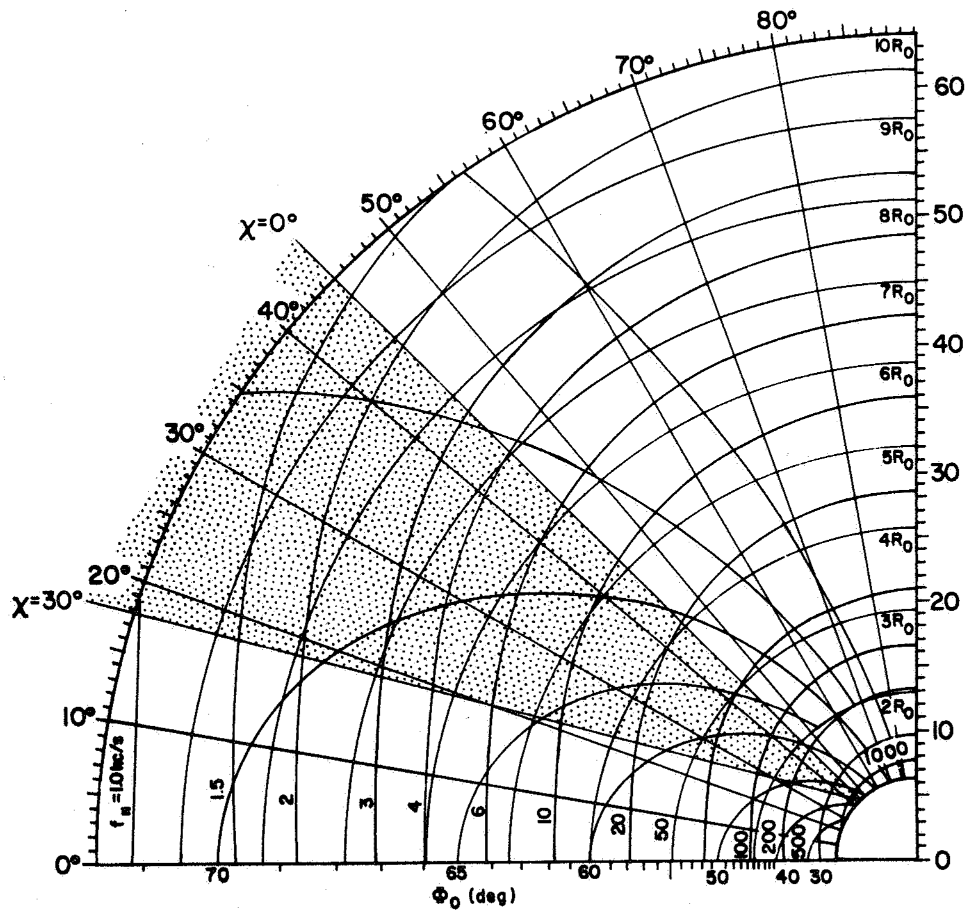

Fig. 21. GEOMAGNETIC FIELD LINES AND CONTOURS OF CONSTANT GYROFREQUENCY. Shaded area denotes range of zenith angles between 0° and 30° at Stanford. [From Mlodnosky and Helliwell, 1962.]

quasi-longitudinal approximation n is real for both characteristic waves. Actually, there is a very small imaginary part which typically corresponds to about 1 dB of attenuation of the wave at 25 MHz during the day and one-tenth that at night. Beyond the ionosphere, as the geomagnetic field intensity decreases, the polarizations of the two characteristic waves are unchanged but the two refractive indices approach the same value. Since any polarization can be resolved into two components having opposite-sense circular polarization, this means that all polarizations are preserved when the static magnetic field is absent.

A linearly polarized wave resolves into equal-strength circularly polarized waves that propagate at different velocities according to Eq. (3.4) but are otherwise unchanged. Thus the resultant wave at any point is still linearly polarized but, because of the phase shift between the components, the plane of polarization rotates as a function of distance. This is the familiar phenomenon of Faraday rotation. Its magnitude is found from the total phase difference between the two components along the path, and, when Eq. (3.4) applies, is given by

$$\Omega = \frac{k}{f^2} \int_0^d H_o \cos\theta \, N \, d\ell \qquad \text{radians} \tag{3.5}$$

where

$$k = \frac{e^3 \mu_o}{(2\pi)^2 \, 2cm^2 \epsilon_o} = 2.97 \times 10^{-3} \qquad \text{(MKS)}$$

This expression is correct when the raypaths for the two magnetoionic components are sufficiently coincident that H_oN is essentially the same for both components, and when they are circularly polarized. The low degree of refraction associated with high elevation angles tends to assure that the error is small. When the direction of propagation is reversed, Ω is unchanged, so for a two-way transmission such as to the moon and back, the total rotation is twice the one-way amount.

Because both the electron density in the ionosphere and the path change with time, Ω can vary over more than two orders of magnitude. At 25 MHz and with a columnar content $\int_o^d N \, d\ell$ of 10^{17} m^{-2}, a typical value of Ω is about 100 rad. When the electron content is changing rapidly, as in the morning hours, Ω can have rates of change of 1 rad/min or more.

A changing columnar electron content also causes a frequency shift in the wave similar to a doppler shift because the phase-path length changes with time. The amount of this frequency shift, called doppler excess, is given by

$$\Delta f = \frac{e^2}{4\pi\omega c \epsilon_o m} \frac{d}{dt}\left(\int_0^d N \, d\ell\right)$$

$$= - \frac{1.35 \times 10^{-7}}{f} \frac{d}{dt}\left(\int_0^d N \, d\ell\right) \quad \text{hertz} \qquad (3.6)$$

As a result of the frequency-range equivalence of the mixed received signal, this effect causes a change in the apparent range, but this is nearly always negligible. A typical large value for the rate of change of the columnar content is 10^{17} electrons/m^2/hr, which at 25 MHz gives a magnitude of 0.15 Hz for Δf. This is more than an order of magnitude smaller than the resolution available and is completely negligible. On some occasions, however, very rapid changes in content may occur, and this effect would limit the range resolution.

The refraction caused by the spherical stratification of the ionosphere is considerably less than the beamwidths of the antennas used when the vertical incidence critical frequency is not too large or the elevation angle is not too small [Howard, 1965]. The refraction at 25 MHz as a function of the critical frequency with the elevation angle as a parameter is shown in Fig. 22, compared to the smaller dimension of beamwidth of the antenna used. At 50 MHz the refraction is four times smaller and the beamwidth of the antenna is considerably larger so there is practically no effect. The irregular component of the refraction is considerably larger than the spherical component, and rough estimates of its magnitude at 25 and 50 MHz are given in Fig. 23 [Lawrence et al, 1964]. It is clear that on 25 MHz this could begin to cause difficulties with measurements when the elevation angle goes below 50°.

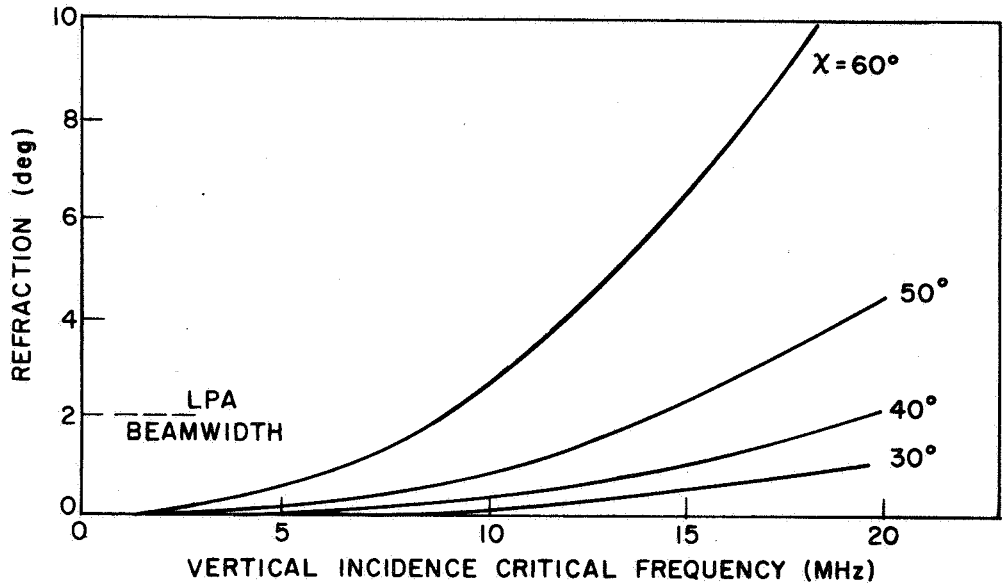

Fig. 22. SPHERICAL REFRACTION AT 25 MHz VS VERTICAL INCIDENCE CRITICAL FREQUENCY FOR ZENITH ANGLES BETWEEN 30° AND 60°.

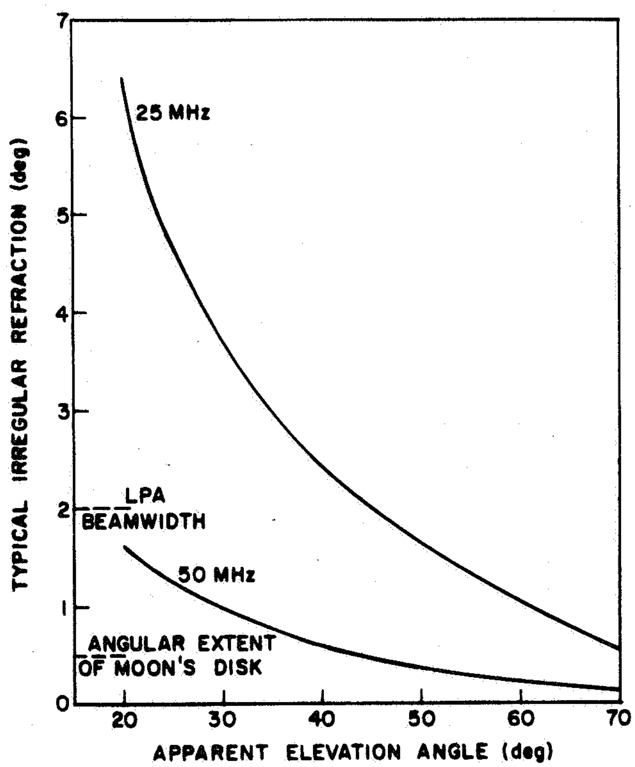

Fig. 23. TYPICAL IRREGULAR IONOSPHERIC REFRACTION VS ELEVATION ANGLE AT 25 AND 50 MHz.

B. Dispersive Effects on the FM Signal

The results presented above are only valid for monochromatic waves; and when a signal with a finite extent in spectrum is transmitted, the effects are much more complicated since each of the signal's frequency components travels at its own phase velocity. Furthermore, since the medium is not just dispersive but is birefrigent also, two waves of different phase velocity are excited for every component. Not only the familiar effects of group velocity and pulse dispersion have to be considered here; the question of the polarization of the signal has to be carefully considered when the original polarization was not that of one of the two characteristic waves. The general question of the distortion of signals passing through the ionosphere will not be investigated since only the linear FM signal used is of interest here.

If the spectrum of the signal is not too broad and the refractive index does not vary too rapidly with frequency, the signal travels nearly undistorted in shape at the group velocity given by

$$\nu_g = \frac{d\omega}{dk} = \frac{c}{\mu + \omega \frac{d\mu}{d\omega}} = \frac{c}{\mu'} \tag{3.7}$$

where $\mu' = \mu + \omega(d\mu/d\omega)$ is the group refractive index. For the ionosphere when Eq. (3.4) holds, Eqs. (3.7), (3.4), and the definitions of X and Y directly give

$$\mu_{\pm} \cong 1 + \frac{1}{2}X(1 \mp 2Y_L)$$

$$= 1 + \frac{1}{2}\frac{\omega_N^2}{\omega^2}\left(1 \mp 2\frac{\omega_H}{\omega}\cos\theta\right) \tag{3.8}$$

The group path length is

$$P'_{\pm} = \int_0^d \mu'_{\pm}\, d\ell \tag{3.9}$$

and the change $\Delta\ell'$ caused by the ionized regions is

$$\Delta\ell'_{\pm} = \int_0^d (\mu_{\pm} - 1)\, d\ell = \int_0^d \frac{1}{2}\frac{\omega_N^2}{\omega^2}\left(1 \mp 2\frac{\omega_H}{\omega}\cos\theta\right) d\ell \tag{3.10}$$

Then the extra time delay is

$$\Delta T_{\pm} = \frac{\Delta\ell'_{\pm}}{c} = \frac{1}{2c\omega^2}\int_0^d \omega_N^2\, d\ell \mp \frac{1}{c\omega^3}\int_0^d \omega_N^2\omega_H \cos\theta\, d\ell \tag{3.11}$$

which becomes, from the definitions of ω_N and ω_H,

$$\Delta T_{\pm} = \frac{1}{\omega^2}\frac{e^2}{2cm\epsilon_o}\int_0^d N\, d\ell \mp \frac{1}{\omega^3}\frac{e^3\mu_o}{cm^2\epsilon_o}\int_0^d NH\cos\theta\, d\ell$$

$$= \frac{1}{\omega^2}\frac{e^2}{2cm\epsilon_o}\int_0^d N\, d\ell \mp 2\frac{\Omega}{\omega} \tag{3.12}$$

The first term, which is the average extra delay, is generally considerably larger than the second term at frequencies used for transionospheric propagation. At 25 MHz, with a columnar content of 10^{17} m^{-2} and with $\Omega = 100$ rad, $\Delta T_{\pm} \cong 21 \mp 1.25$ μs. For a lunar radar experiment at this frequency, the component of the signal propagating in the ordinary mode would arrive 5 μs before the extraordinary component. Besides the dispersive broadening of a short pulse, this effect will cause considerable distortion, even to completely separating the original single pulse into two, unless the signal was transmitted with circular polarization. For initially linear polarization, note that the polarization of the received pulse first would be circular, then presumably more or less linear, and finally oppositively circular.

Alternatively, rather than separate the initially linearly polarized signal into circularly polarized components, one could find the amount of Faraday rotation for each frequency component, and then sum the components, each with its own phase shift, to determine the emergent signal. The Faraday rotation accounts for the differential phase shift between the magnetoionic components, but there is an additional larger amount corresponding to the average phase velocity of the components. Figure 24 is a qualitative illustration of the vector dispersion of the frequency components of a repetitive pulse signal. For a total Faraday rotation of 100 rad at 25 MHz, the change in rotation across the extent of the spectral components of a 10 μs pulse is about 100°, and twice that for a two-way passage.

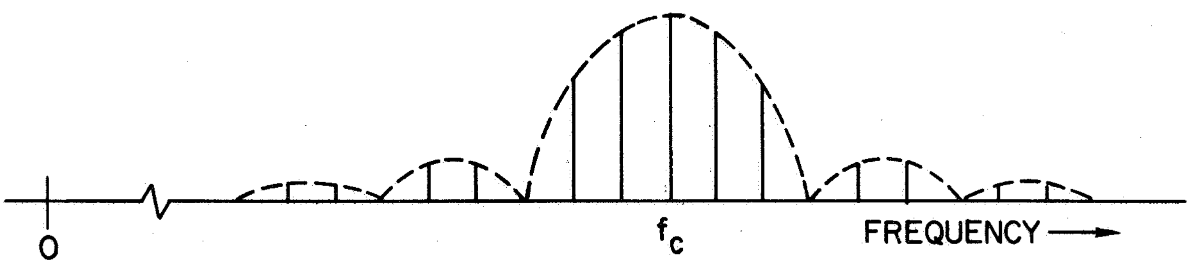

a. Magnitude of spectral components

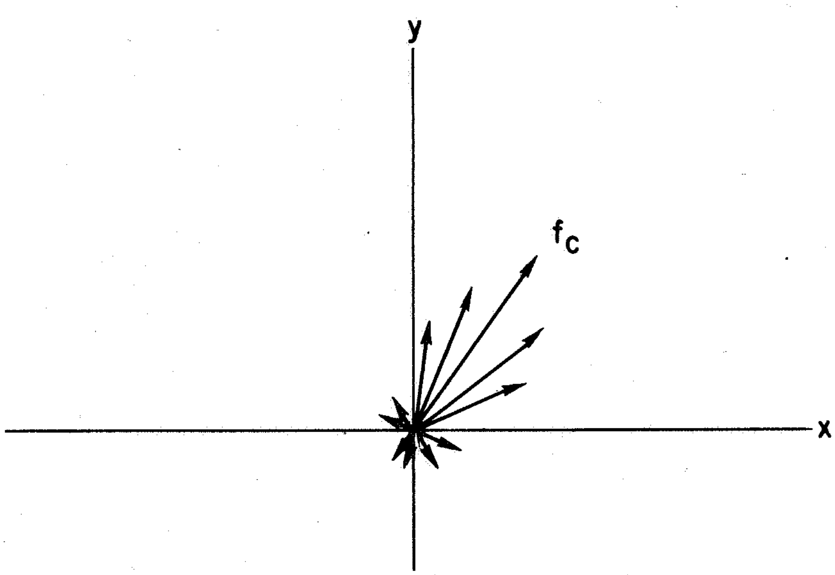

b. Directions of linearly polarized components

Fig. 24. POLARIZATION DISPERSION OF THE COMPONENTS OF A LINEARLY POLARIZED PULSE SIGNAL.

It is not really the polarization qualities of the radio signal which interest us here, but rather the effect of the combination of the polarization changes and the receiving antenna. Since an antenna can only respond to the component of the incident radiation having the same polarization as the antenna, it is necessary to find that component to determine the signal at the antenna terminals. For a linearly polarized antenna this can be done by taking the projection of the linearly polarized spectral components onto the polarization plane of the antenna.

For the linear FM signal a very simple approximate interpretation is possible. If the rate of frequency change is very small, the amount of Faraday rotation at any particular time will be the same as that of a CW wave having the same frequency as the chirp at that time. Thus, as the frequency changes, the amount of Faraday rotation changes, and the strength of the signal is multiplied by the cosine of the angular difference between the instantaneous incident and the antenna's polarization planes, which is just the Faraday rotation itself when the same antenna is used for transmitting and receiving. The Faraday rotation at frequencies f_o and $f_o + \Delta f$ are $\Omega_o = Q/f_o^2$ and $\Omega_o + \Delta\Omega = Q/(f_o + \Delta f)^2$ by Eq. (3.5), so the differential change $\Delta\Omega$ for $\Delta f \ll f_o$ is

$$\Delta\Omega = \frac{Q}{(f_o + \Delta f)^2} = - \frac{Q}{f_o^2} \cong -2\Omega_o \frac{\Delta f}{f_o} \tag{3.13}$$

The instantaneous frequency of the chirp signal is, from Eq. (2.2), $f_i = 2\psi t + f_o$, so that, because $f_o \gg 2\psi t$, the instantaneous Faraday rotation is

$$\Omega \cong \Omega_o - 4\Omega_o \frac{\psi}{f_o} t \tag{3.14}$$

Therefore the receiving antenna voltage varies as

$$\nu(t) = \cos\left(\Omega_o - 4\Omega_o \frac{\psi}{f_o} t\right) \cos 2\pi\left(\psi t^2 + f_o t\right) \tag{3.15}$$

and the mixed IF output has the same modulation factor. This applies to the expected polarization component of a lunar radar echo; but for the depolarized component, which is orthogonal to the expected one by definition, the cosine of the rotation angle is replaced by the sine. All range intervals on the moon are affected equally because there is no appreciable Faraday rotation at the moon. That this approximation gives the proper result has to be verified.

The combination of Faraday rotation and the antenna acts as a filter on the transmitted signal. Let $S(f)$ be the spectrum of the transmitted signal, $E(f)$ the spectrum at the receiving antenna terminals, and $C(f)$ the filter function. $S(f)$ is given by Eq. (3.3) and $C(f)$ from the considerations above is

$$C(f) = \cos \Omega(f) \cong \cos \frac{Q}{f^2} \tag{3.16}$$

and $E(f) = C(f)\ S(f)$. By the convolution theorem,

$$e(t) = \int_{-\infty}^{\infty} s(\tau)\ c(\tau - t)\ d\tau \tag{3.17}$$

where

$$s(\tau) = \begin{cases} \cos 2\pi(\psi\tau^2 + f_o\tau) & 0 \leqq \tau \leqq T \\ 0 & \text{elsewhere} \end{cases}$$

as before. Unfortunately $C(f)$ given by Eq. (3.16) does not have a Fourier transform because of the oscillatory discontinuity at the origin, so $C(t)$ cannot be obtained from it.

However, $C(f)$ derives from approximations which are only valid at high frequencies, and since $S(f)$ is only significant in a small band near $\pm f_o$, we can make some further approximations on $C(f)$ to simplify the computation considerably. Putting $f = f_o + \Delta f$, where $\Delta f \ll f_o$,

$$C(f) \cong \cos \frac{Q}{f_o^2\left(1 + \frac{\Delta f}{f_o}\right)} \cong \cos \frac{Q}{f_o^2}\left(1 - 2\frac{\Delta f}{f_o}\right)$$

$$= \cos \frac{Q}{f_o^2}\left(3 - 2\frac{f}{f_o}\right) .$$

For frequencies near $-f_o$, the equivalent expression is

$$C(f) \cong \cos \frac{Q}{f_o^2}\left(3 + 2\frac{f}{f_o}\right)$$

Combining these two yields the filtering function for the frequencies of interest,

$$C(f) \cong \cos \left[\frac{Q}{f_o}\left(3 - 2\frac{|f|}{f_o}\right)\right]$$

$$= \cos (3\Omega_o) \cos \left(2\Omega_o \frac{f}{f_o}\right) + \sin (3\Omega_o) \sin \left(2\Omega_o \frac{|f|}{f_o}\right) \qquad (3.18)$$

where $\Omega_o = Q/f_o^2$. The term involving $|f|$, $\sin [2\Omega_o(|f|/f_o)]$, is difficult to handle and is replaced with $\sin [2\Omega_o(f/f_o)] \sin (\pi/2)(f/f_o)]$, which is a very good approximation since $\Omega 2_o \gg \pi/2$ and the frequencies of interest are very close to $\pm f_o$. With this final approximation the filtering function becomes

$$C(f) = \cos (3\Omega_o) \cos \left(2\Omega_o \frac{f}{f_o}\right) + \frac{1}{2} \sin (3\Omega_o) \cos \left(2\Omega_o - \frac{\pi}{2}\right) \frac{f}{f_o}$$

$$- \frac{1}{2} \sin (3\Omega_o) \cos \left(2\Omega_o + \frac{\pi}{2}\right) \frac{f}{f_o} \qquad (3.19)$$

and the corresponding time function is

$$c(t) = \int_{-\infty}^{\infty} C(f)\, e^{j\omega t}\, df$$

$$= \frac{1}{2} \cos\,(3\Omega_o) \left[\delta\left(t - \frac{2\Omega_o}{\omega_o}\right) + \delta\left(t + \frac{2\Omega_o}{\omega_o}\right)\right]$$

$$+ \frac{1}{4} \sin\,(3\Omega_o) \left[\delta\left(t - \frac{2\Omega_o - \frac{\pi}{2}}{\omega_o}\right) + \delta\left(t + \frac{2\Omega_o - \frac{\pi}{2}}{\omega_o}\right)\right]$$

$$- \frac{1}{4} \sin\,(3\Omega_o) \left[\delta\left(t - \frac{2\Omega_o + \frac{\pi}{2}}{\omega_o}\right) + \delta\left(t + \frac{2\Omega_o + \frac{\pi}{2}}{\omega_o}\right)\right] \quad (3.20)$$

The delta functions make the convolution of Eq. (3.18) easy to perform, and except for an insignificantly small interval at each end of the chirp where some terms are beyond the limits of the integration, it yields after considerable manipulation,

$$e(t) = \cos\,(3\Omega_o)\cos\left[\xi\left(t^2 + t_o^2\right) + \omega_o t\right]\cos\,[2\xi t_o t + \omega_o t_o]$$

$$+ \frac{1}{2}\sin\,(3\Omega_o)\left\{\left\{\cos\left[\xi\left(t^2 + t_o^2\right) + \omega_o t\right]\cos\left[\frac{\pi\xi}{2\omega_o}\left(\frac{\pi}{2\omega_o} - 2t_o\right)\right]\right.\right.$$

$$\left. - \sin\left[\xi\left(t^2 + t_o^2\right) + \omega_o t\right]\sin\left[\frac{\pi\xi}{2\omega_o}\left(\frac{\pi}{2\omega_o} - 2t_o\right)\right]\right\}\sin\left[\left(2\xi t_o - \frac{\pi\xi}{\omega_o}\right)t + \omega_o t_o\right]$$

$$+ \left\{\cos\left[\xi\left(t^2 + t_o^2\right) + \omega_o t\right]\cos\left[\frac{\pi\xi}{2\omega_o}\left(\frac{\pi}{2\omega_o} - 2t_o\right)\right]\right.$$

$$\left.\left. - \sin\left[\xi\left(t^2 + t_o^2\right) + \omega_o t\right]\sin\left[\frac{\pi\xi}{2\omega_o}\left(\frac{\pi}{2\omega_o} + 2t_o\right)\right]\right\}\sin\left[\left(2\xi t_o + \frac{\pi\xi}{\omega_o}\right)t + \omega_o t_o\right]\right\}$$

(3.21)

where $\xi = 2\pi\psi$ and $t_o = 2(\Omega_o/\omega_o)$. This expression is valid for $t_o + \pi/2\omega_o < t < T - \pi/2\omega_o$, which is essentially the entire 1 sec sweep, since t_o, which represents the differential group delay between the magnetoionic components, is about 2.5 μs at 25 MHz with $\Omega_o = 200$ rad. Now since

$$\frac{\pi\xi}{2\omega_o}\left(\frac{\pi}{2\omega_o} - 2t_o\right) \sim 10^{-8} \lll 1$$

we have

$$e(t) \cong \cos\left(\xi t^2 + \omega_o t + \xi t_o^2\right)\left\{\cos\left(3\Omega_o\right)\cos\left(2\xi t_o t + \omega_o t_o\right)\right.$$

$$\left. + \frac{1}{2}\sin\left(3\Omega_o\right)\left[\sin\left(2\xi t_o t + \omega_o t - \frac{\xi\pi t}{\omega_o}\right) + \sin\left(2\xi t_o t + \omega_o t + \frac{\xi\pi t}{\omega_o}\right)\right]\right\}$$

$$= \cos\left(\xi t^2 + \omega_o t + \xi t_o^2\right)\left[\cos\left(3\Omega_o\right)\cos\left(2\xi t_o t + \omega_o t_o\right)\right.$$

$$\left. + \cos\left(\frac{\xi\pi t}{\omega_o}\right)\sin\left(3\Omega_o\right)\sin\left(2\xi t_o t + \omega_o t_o\right)\right] \tag{3.22}$$

Therefore, if $\xi\pi t/\omega_o \ll 1$, and since $\omega_o t_o = 2\Omega_o$,

$$e(t) \cong \cos\left(4\frac{\psi\Omega_o}{f_o}t - \Omega_o\right)\cos\left(2\pi\psi t^2 + \omega_o t + \psi t_o^2\right) \tag{3.23}$$

which is the same as Eq. (3.15) except for the small phase shift, $2\pi\psi t_o^2$. The important quantity in the approximation is $\xi\pi t/\omega_o = \psi\pi t/f_o$, which, since $\psi = 5.10^4$ and $t_{max} = T = 1$, is equal to $2\pi \times 10^{-3}$ at 25 MHz and half that at 50 MHz. This indeed satisfies the requirement of being very much less than 1. The important result is that we can treat the chirp signal at any instant as a CW signal having the same frequency as the instantaneous chirp frequency if $\psi\pi t \ll f_o$. For a two-way Faraday rotation of 200 rad, the frequency of the modulation is

$$f_m = \left(\frac{1}{2\pi}\right)\left(4\ \frac{\psi\Omega_o}{f_o}\right) \cong 0.25\ \text{Hz} \tag{3.24}$$

at 25 MHz, and one-eighth that, or 0.031 Hz, at 50 MHz.

This modulation can easily be seen in the receiver output signal; an example is shown in the three frames of Fig. 25 which are from the same run and a few minutes apart. The null corresponds to the time when the direction of expected polarization component of the echo is perpendicular to the antenna and is reduced in sharpness by the depolarized component and the background noise. As the amount of Faraday rotation changes, the phase and frequency of the modulation change proportionally but the phase change is much more evident. A 1 percent change in Ω_o causes an essentially immeasurable change of frequency, but for a Ω_o of about 200 rad the phase changes by 2 rad. Figure 26 illustrates the changing phase by the position of the null in the 1 sec sweep interval. The total amount of Faraday rotation could in principle be unambiguously measured by determining the modulating frequency f_m; but since f_m is a small number, the modulation generally does not even complete half a cycle (a value of Ω_o = 400 rad at 25 MHz would be necessary), which makes it hard to measure accurately. If two or more nulls were present, f_m could readily be measured. Any change in Ω_o can easily be measured by noting the change in position of the null.

When only a single null is visible and if Ω_o is changing at a constant rate, the motion of the null suggests a way to measure f_m fairly accurately. Figure 27 depicts the position of several nulls as a function of time for frequencies near those of the transmitted sweep, with the boundaries of the sweep indicated by the vertical lines which are, of course, 100 kHz apart or, alternatively, spaced by T_s = 1 sec. Since $f_m = 1/(2T_n)$, simple geometry shows that $f_m = (T_t - T_d)/2T_tT_s = (T_t - T_d)/2T_t$. The quantities T_t and T_d can readily be measured from the photographic strip record of Fig. 26, each cycle of the visible null's

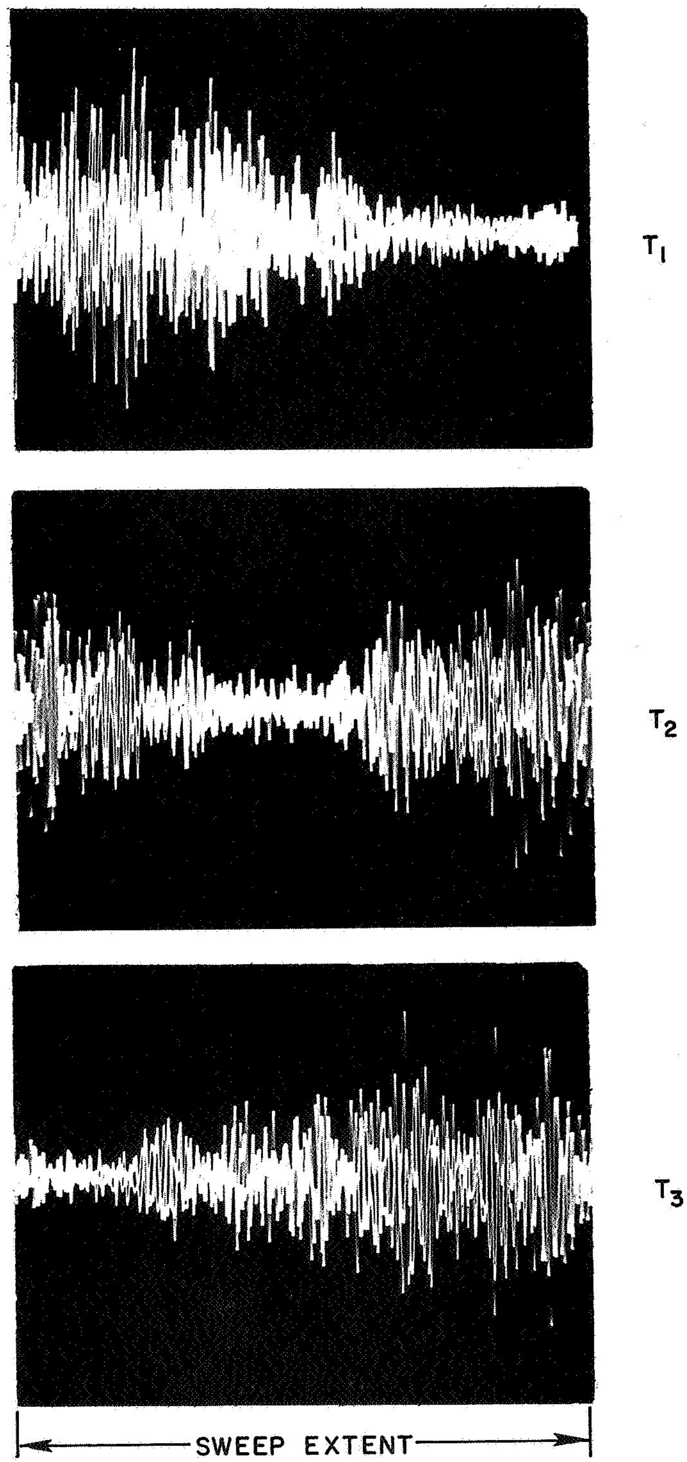

Fig. 25. RECEIVER OUTPUT SIGNAL PHOTOGRAPHED SEVERAL MINUTES APART. More than one sweep appears in each frame.

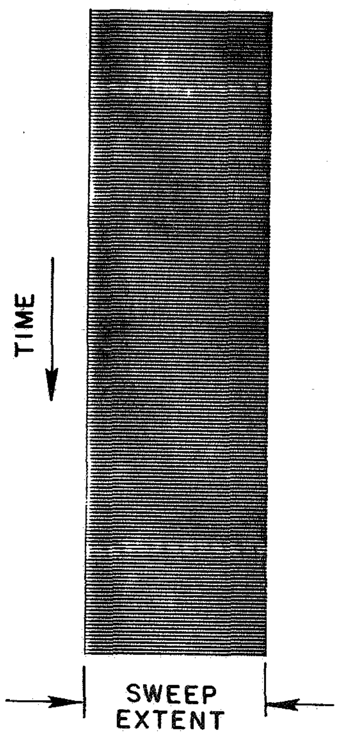

Fig. 26. INTENSITY ACROSS SWEEP INTERVAL OF RECEIVER OUTPUT SIGNAL. The light bands are time marks 10 min apart.

movement yielding a separate measurement, several of which can be averaged to reduce the error. The rate of motion of the nulls has to be extrapolated from their behavior before and after disappearance, but occasions when the rate changes considerably appear to be rare, and there seems to be only a small variance in the estimation of f_m if the obviously bad ones are not included.

Since f_m itself changes with the motion of the null, the applicability of this scheme is limited to times when the total rotation is rather large so that the error due to the changes is small. Also, the change of rotation should be sufficiently fast to allow several measurements to be made. For the two sets of data chosen for analysis, both these conditions exist. If the total rotation were small or unchanging, some other scheme would have to be used to measure f_m accurately, but that was not necessary here.

Because it is important to the scheme for separating the polarized components of the echoes (Chapter IV), the phase as well as the frequency of the modulation has to be measured for every echo. This was done by

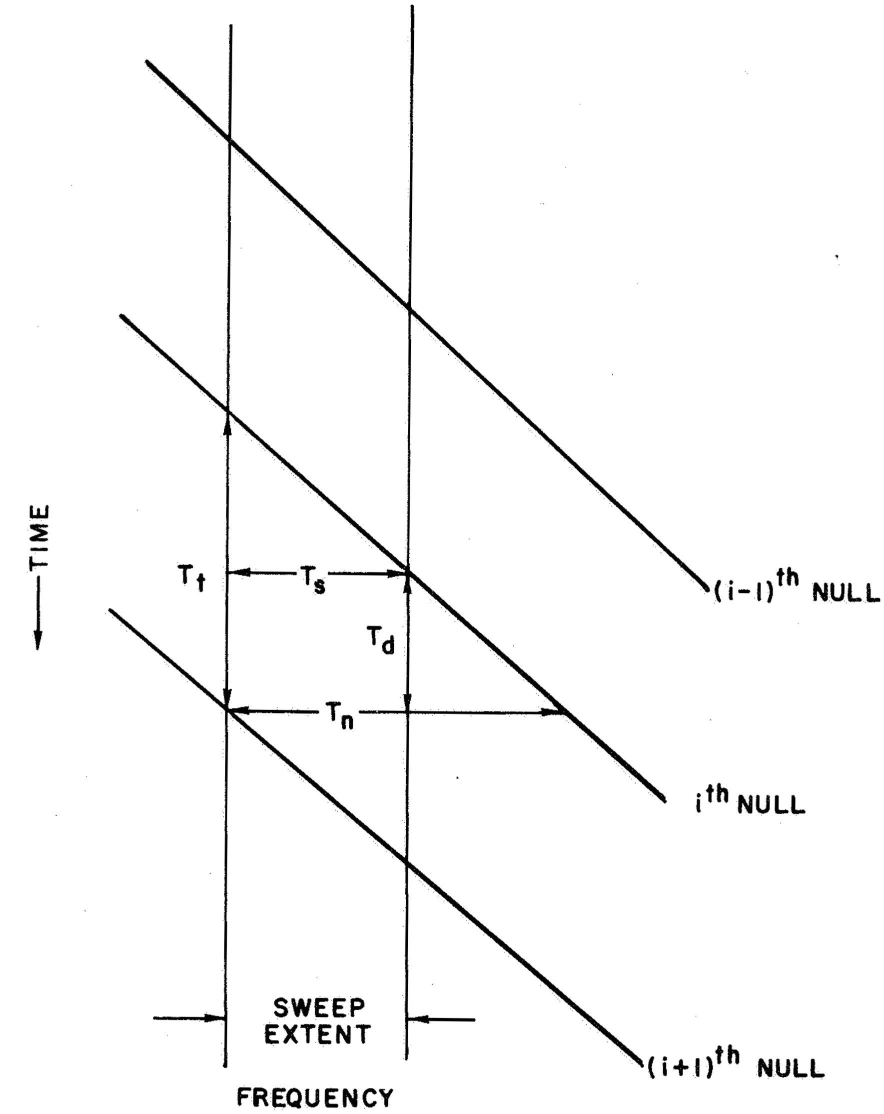

Fig. 27. POSITIONS OF SEVERAL NULLS AS A FUNCTION OF TIME.

determining the position of the null, not from the film strip of Fig. 26 but from the digitized data. Each echo is separated into 10 segments, the average of the magnitudes of the sample values in each segment is computed, and the smallest average located. The position of the smallest is the position of the null, at least when a null is in the sweep and if there are no difficulties with the background noise, the depolarized component, or the fading of the echo itself. The echo fading can be seen in Fig. 25, and is plotted to give essentially the same display as in Fig. 26. An example is shown in Fig. 28, where the smooth motion of the null can be easily followed even though there is scatter due to the fading

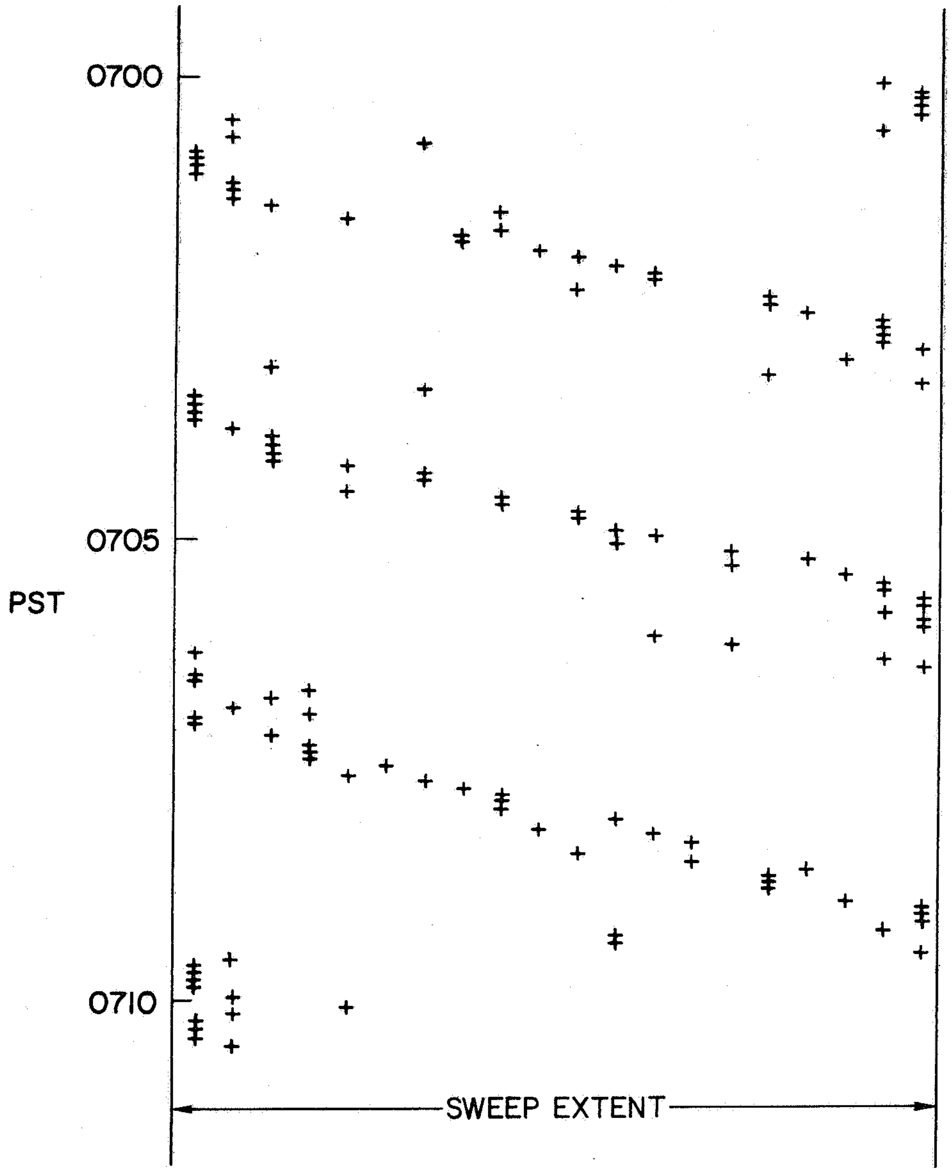

Fig. 28. POSITION OF NULL IN SWEEP FOR RUN OF 20 AUGUST 1965.

characteristics of the target, particularly at the edges of the sweep when no Faraday null is present. The advantage of using this method rather than the film strip is that the null can be more accurately located and associated with each echo.

Besides the polarization distortion and the group delay, there are other dispersive effects. In general, a pulse signal would also become distorted in shape and broaden in time as it progressed through the dispersive medium. The most important effect is the frequency-dependent differential phase shift between the two magnetoionic components that causes the rotation of the polarization direction during the sweep just discussed, but any overall frequency-dependent effect must be considered also. Using the same arguments as before about considering the linear FM signal at any particular time to have the same properties as a signal of limited bandwidth having a center frequency equal to the instantaneous frequency of the FM signal, it is easy to see that there will be a change in group delay from one end of the sweep to the other. If ΔT_o is the average extra time delay of the two polarization components at f_o, then the differential delay δT between f_o and $f_o + \Delta f$, where $\Delta f \ll f_o$, is found by applying Eq. (3.12),

$$\delta T \cong 2\Delta T_o \frac{\Delta f}{f_o} \tag{3.25}$$

With $f_o = 25$ MHz, $\Delta f = 100$ kHz, and $\Delta T_o = 50\ \mu s$, the differential delay across the sweep is -0.8 μs. Because the higher frequencies are less delayed than the lower ones, the instantaneous frequency-time track of the received echoes has a different slope than the transmitted signal and the mixing signal as shown in Fig. 29. This is a similar effect to that of the doppler shifts from the moon's motions. Since its magnitude is below the resolution obtainable, this effect is completely negligible, as it was with the doppler shifts.

C. Irregular Ionospheric Effects

Irregularities in the electron density distribution that cause amplitude and phase scintillations and introduce the irregular component of refraction previously discussed can cause great difficulties with lunar radar experiments at decameter wavelengths. The only way to compensate for the effects of the irregularities is by choosing data from those days when there is little or no echo fluctuation other than the

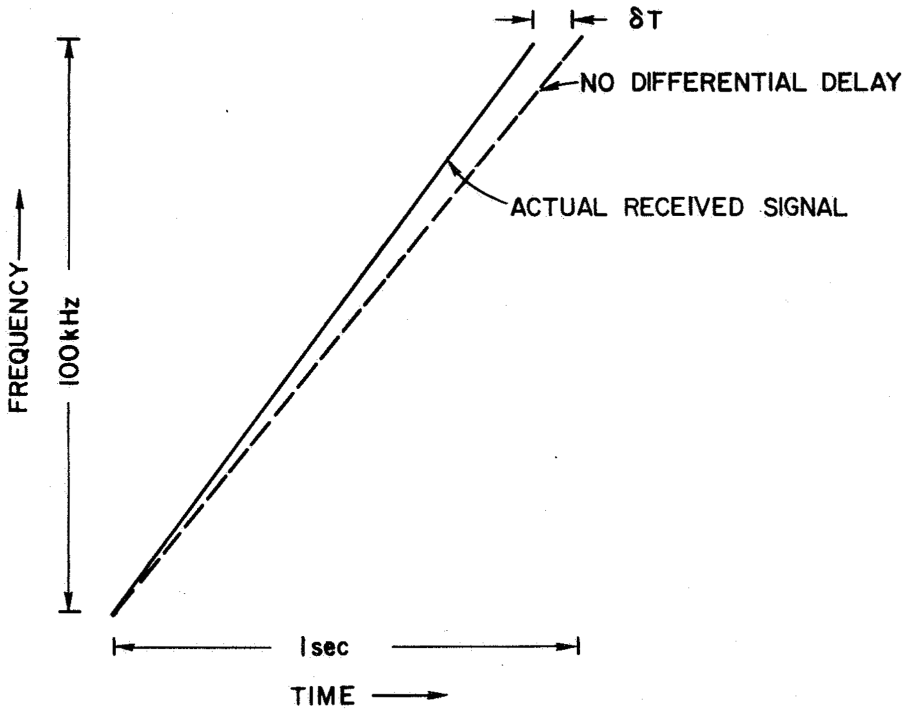

Fig. 29. FREQUENCY-TIME TRACK OF RECEIVED SIGNAL SHOWING SKEWING DUE TO DIFFERENTIAL GROUP DELAY.

Faraday or the libration fading. It must be stated, however, that what constitutes a "good" data run is a subjective impression based on inspecting the records of many runs, and that it is nearly impossible to isolate any specific phenomenon. It is significant that the "best" data comes from days when the elevation angle of the moon is large, say larger than 50°, because these effects are expected to be smaller at higher elevation angles [Lawrence et al, 1964] since the signals traverse a shorter distance through the ionosphere.

The previous short-pulse radar observations at decameter wavelengths were considerably handicapped by being limited by the antenna to low elevation angles [Davis et al, 1965]. Even in the worst records, the effects due to irregularities seen here were always less than an order of magnitude below those reported. In particular, a variation of 1 ms in the group delay was often noted in their results, but here such fluctuations were rarely noted and then only at a maximum magnitude of a few tens of microseconds. This effect cannot be seen at all when the data from high elevation angles is inspected; an illustration of this is the range-time plots of Figs. 19 and 20.

D. Summary

The values shown in Table 3 for some of the quantities discussed above are roughly typical for two-way daytime zenith propagation with equal columnar contents, 10^{17} m^{-2}, in the ionosphere and cislunar medium. The differential amounts refer to the end frequencies of the 100 kHz-wide chirps, and the doppler excess is based on a changing content of 10^{17} m^{-2} hr^{-1}.

Table 3

TYPICAL VALUES OF IONOSPHERIC PROPAGATION PARAMETERS

Wavelength (m)	6	12
Faraday rotation, Ω_o (rad)	50	200
Differential Faraday rotation, $\Delta\Omega$ (deg)	10.5	92
Group delay, $\Delta T_{o\pm}$ (μs)	21 ∓ 0.3	84 ∓ 2.5
Differential average group delay δT (μs)	0.17	1.35
Doppler excess, Δf (Hz)	0.075	0.15
Attenuation (dB)	0.5	3

For the main block of data analyzed, that of 24 August 1965, the measured amounts of Faraday rotation and group delay were 330 rad and 70 μs on 12 m. The differential amounts of rotation were 150° on 12 m and 19° on 6 m, so the polarization planes of the incident radiation at the moon rotated 75° and 9.5° for the two wavelengths.

Chapter IV

ESTIMATION OF LINEARLY POLARIZED ECHO COMPONENTS

A. Introduction

It was shown in Chapter III that the combination of the ionospheric Faraday rotation and the receiving antenna imposes a sinusoidal modulation on the echoes. Furthermore, the phase and frequency of this modulation could be accurately measured for each echo. Also, because the expected and depolarized components of the echo are perpendicular to each other in space, the phases of modulation on these two components differ by 90°. Thus, since it is the phase of the expected component that is measured (the depolarized part is very much weaker), the modulation function on the depolarized component can be easily determined. Finally, because there is essentially no Faraday rotation at the moon, all range intervals are affected equally.

The effect of this modulation on the spectral analysis shall now be considered, as well as the use of the difference between the modulation on the expected and depolarized components for separating them. The assumptions made, such as perfectly linearly polarized antennas and independence of the polarized components of the echoes, will also be discussed.

B. Effect of Faraday Modulation on the Spectral Analysis

The simplest way to look at this modulation is as part of the data and spectral window pair. Instead of just having a multiplicative data window such as the hamming or hanning windows, we now have the product of the data window function and the Faraday modulation function. By Eq. (3.23) the modulation functions for the expected and depolarized echoes are

$$f_E(t) = \cos (2\pi f_m t - \Omega_o)$$

and

$$f_D(t) = \sin (2\pi f_m t - \Omega_o)$$

so the data windows become

$$w_E(t) = [A-B \cos (2\pi/T)] \cos (2\pi f_m t - \Omega_o)$$

and

$$w_D(t) = [A-B \cos (2\pi t/T)] \sin (2\pi f_m t - \Omega_o)$$

where $A = B = 0.5$ for the hanning windows, and $A = 0.544$ and $B = 0.456$ for the hanning window. It is convenient to measure the phase of the modulation, which changes from echo to echo, from the center of the sweep to the position of the null, instead of using Ω_o. With this change the data windows become

$$w_E(t) = [A-B \cos (2\pi t/T) \sin [2\pi f_m(t-T/2) + \Phi]$$

and (4.1)

$$w_D(t) = [A-B \cos (2\pi t/T)] \cos [2\pi f_m(t-T/2) + \Phi]$$

over the interval $0 < t < T$.

Because the spectral windows are the squared magnitude of the Fourier transform of the data windows, these modified spectral windows are the result of the convolution of the hamming or hanning windows with δ-functions at $\pm f_m$. They have complicated shapes and depend strongly on Φ. In Fig. 30 these resultant windows when $T = 1$ sec are shown for $f_m = 0.425$ (25 MHz) and $f_m = 0.053$ (50 MHz), which are the 24 August 1965 values, along with the hamming window for comparison. The most important influence that the Faraday modulation has is to change the area under the $|W(f)|^2$'s, although their shapes can change considerably and they become slightly wider for the values of f_m usually encountered. Figure 31 shows the variation of $\Delta F = 1/T_e$, where T_e is the equivalent length defined by Eq. (2.20) as a function of Φ for the windows of Fig. 30. The shape of the spectral windows is symmetrical and periodic with Φ with a period of 180°; all parameters describing these windows therefore behave in this way with respect to Φ also. Since ΔF for the hamming window is 1.81 Hz, the modulation only changes ΔF significantly for Φ less than 20° at 50 MHz and only moderately increases ΔF

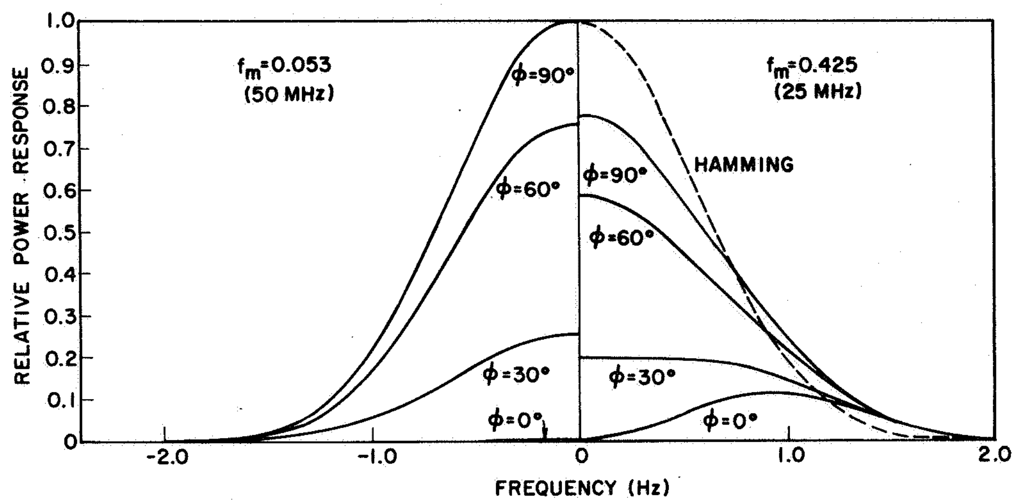

Fig. 30. SPECTRAL WINDOWS MODIFIED BY FARADAY MODULATION FOR TWO MODULATING FREQUENCIES AND SEVERAL PHASE ANGLES. The hamming window is shown for comparison.

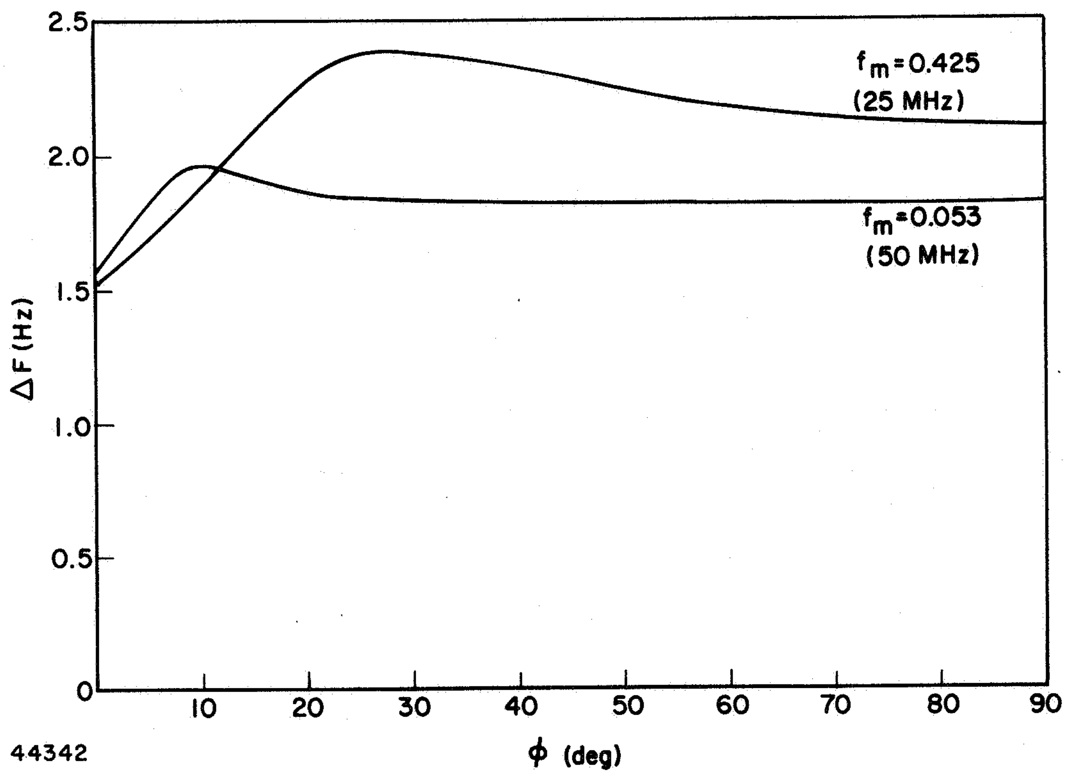

44342

Fig. 31. RESOLVING CAPABILITY FOR FARADAY-MODIFIED SPECTRAL WINDOWS AS A FUNCTION OF MODULATION PHASE ANGLE. For the underlying hamming window, ΔF is 1.81 Hz.

at 25 MHz. Therefore the Faraday modulation does not seriously decrease the range resolving capabilities of the system. The maximum amplitude of the sidelobes of these modified spectral windows is at most 6 dB above that of the underlying standard windows; this condition occurs when $2f_m$ is near the sidelobe spacing.

Since we have incorporated the Faraday modulation into the spectral analysis, the true power spectrum of the echoes will be considered unchanged. Thus the response of the estimator of the power spectrum is contained in the normalizing quantity U introduced in Eq. (2.14) and defined following Eq. (2.17):

$$U = \frac{1}{T}\int_{-F/2}^{F/2} |W_p(f)|^2 \, df \tag{4.2}$$

Now, because $W(f)$ is narrowly distributed about $f = 0$, aliasing is negligible and $W_p(f)$ can be accurately replaced by $W(f)$ in Eq. (4.3), so

$$U \cong \frac{1}{T}\int_{-\infty}^{\infty} |W(f)|^2 \, df = \frac{1}{T}\int_0^T w_m^2(t) \, dt$$

When this integration is performed with $w_E(t)$ and $w_D(t)$ given by Eqs. (4.1)

$$U_E = K - K' \cos (2\Phi)$$

and (4.3)

$$U_D = K + K' \cos (2\Phi)$$

K and K' are functions of f_m, T, A, and B:

$$K = \pi(A^2 + B^2/2)$$

$$K' = \left[\frac{A^2 + B^2/2}{2f_m T} - \frac{4f_m TB^2}{4f_m^2 T^2 - 1} + \frac{f_m TB^2}{4(f_m^2 T^2 - 1)}\right] \sin(2\pi f_m T)$$

K' is typically slightly smaller than K. It should be noted that K is independent of $f_m T$ and is exactly one-half the value of U for the standard window which depends on the choice of A and B. Thus, if U is the normalizing constant for the standard window, Eqs. (4.3) can be written as

$$U_E = \frac{1}{2} U[1 - V \cos(2\Phi)]$$

and (4.4)

$$U_D = \frac{1}{2} U[1 + V \cos(2\Phi)]$$

where $V = 2K'/U$. The background noise component is just normalized by U, of course, since the noise is unaffected by the Faraday rotation.

The U's represent the relative responses of the power spectral analysis to the two echo components and the noise. Let the true expected component power spectrum be denoted by Φ_E, the true depolarized spectrum by Φ_D, and the noise spectrum by Φ_N. Then, since the noise is independent of the echo components, and if we assume that the two echo components are uncorrelated, the spectral estimating procedure will yield the weighted sum of the independent estimates of the three signal components. In Eq. (2.15) the normalized spectral window was used, but now there are three windows with different normalizations. If the estimates are not normalized, the normalization quantities can be interpreted as the weights of the three components in spectral estimates. Extending Eq. (2.15) to this situation and removing the normalizations, we get for the mean value of the spectral estimate (see Appendix A)

$$\overline{\hat{P}(n\Delta f)} = \int_{-\infty}^{\infty} U_E H_E(f') \, \Phi_E(n\Delta f - f') \, df'$$

$$+ \int_{-\infty}^{\infty} U_D H_D(f') \, \Phi_D(n\Delta f - f') \, df'$$

$$+ \int_{-\infty}^{\infty} U_N H_N(f') \, \Phi_N(n\Delta f - f') \, df' \qquad (4.5)$$

where the H's are the normalized spectral windows. Therefore

$$\overline{\hat{P}_E(n\Delta f)} = \int_{-\infty}^{\infty} H_E(f') \, \Phi_E \, (n\Delta f - f') \, df'$$

$$\overline{\hat{P}_D(n\Delta f)} = \int_{-\infty}^{\infty} H_D(f') \, \Phi_D(n\Delta f - f') \, df'$$

and

$$\overline{\hat{P}_N(n\Delta f)} = \int_{-\infty}^{\infty} H_N(f') \, \Phi_N(n\Delta f - f') \, df'$$

are properly normalized, and the estimating procedure yields

$$\overline{\hat{P}(n\Delta f)} = U_E \overline{\hat{P}_E(n\Delta f)} + U_D \overline{\hat{P}_D(n\Delta f)} + U_N \overline{\hat{P}_N(n\Delta f)} \qquad (4.6)$$

as the mean value of the estimate. If we now normalize this to $U_N = U$ and use the expressions for U_E and U_D in Eqs. (4.4),

$$\overline{\hat{P}(n\Delta f)} = \frac{1}{2}[1 - V \cos (2\Phi)] \, \overline{\hat{P}_E(n\Delta f)}$$

$$+ \frac{1}{2}[1 + V \cos (2\Phi)] \, \overline{\hat{P}_D(n\Delta f)} + \overline{\hat{P}_N(n\Delta f)} \qquad (4.7)$$

All ranges of a particular echo have the same weights, but since Φ changes with time as the total Faraday rotation changes, each echo has its own distinct set of weights, which are known from measurement of Φ. Thus estimates of Φ_E, Φ_D, and Φ_N can presumably be made from the results of performing the analysis on several echoes. Unfortunately since U_E, U_D, and U are linearly related, this cannot be done, and the best one can do is to obtain estimates of such quantities as $\Phi_E - \Phi_D$, $\Phi_E + \Phi_N$, and $\Phi_D + \Phi_N$. This estimation will be considered fully in the next section. First, it is important to consider the assumptions of perfect linearly polarized antennas and of the uncorrelation between the expected and depolarized echo components.

If the expected and depolarized components of the echo were partially correlated, Eqs. (4.5) - (4.7) would have to be modified by the addition of another term involving the cospectrum of the two components. In Appendix A this term was found to be

$$\overline{\hat{P}_{ED}(f)} = \mathrm{Re}\left\{\int_{-\infty}^{\infty} \frac{2}{T} W_E(f') W_D^*(f') \Phi_{ED}(f' - f)\, df'\right\} \tag{4.8}$$

where

$$\Phi_{ED}(f) = \int_{-\infty}^{\infty} R_{ED}(\tau)\, e^{-j\omega\tau}\, d\tau$$

and $R_{ED}(\tau)$ is the crosscorrelation function between the expected and depolarized components. As before, the contribution from $\Phi_{ED}(f - f')$ to the estimate is concentrated at $f' = 0$, and if $\Phi_{ED}(f)$ changes slowly compared to $W_E(f') W_D^*(f')$, Eq. (4.8) becomes

$$\begin{aligned}\overline{\hat{P}_{ED}(f)} &\cong \mathrm{Re}\left\{\Phi_{ED}(f) \int_{-\infty}^{\infty} \frac{2}{T} W_E(f') W_D^*(f')\, df'\right\} \\ &= \mathrm{Re}\left\{U_{ED}\, \Phi_{ED}(f)\right\}\end{aligned} \tag{4.9}$$

This is the same type of quantity as in the terms of Eq. (4.6) and is directly comparable to them. By Parseval's theorem

$$U_{ED} = \frac{2}{T} \int_{-\infty}^{\infty} W_E(f') \; W_D^*(f') \; df' = \frac{2}{T} \int_0^T w_E(t) \; w_D(t) \; dt$$

which, when the expressions for $w_E(t)$ and $w_D(t)$ are inserted, is

$$U_{ED} = K' \sin (2\phi) = \frac{1}{2} UV \sin (2\phi) \tag{4.10}$$

This is the same as the variable terms in Eqs. (4.3) and (4.4) except for being 90° out of phase with them.

Because the average value of U_{ED} is zero it will be seen that the final estimation of the components of the scattering is insensitive by Φ_{ED}. This alone justifies ignoring it. However, it is also anticipated that the expected and depolarized components of the echoes are only slightly correlated, if at all, so Φ_{ED} is a negligibly small quantity compared to Φ_D.

This argument is based on the fact that the scattered field from any range interval is the sum of the fields from a large number of individual scatterers. Since each of these elements has a different shape and composition, they will depolarize the incident radiation in a different way. The total scattered field will then be the sum of randomly oriented vectors; the distribution of orientations will have a maximum since the scattered field has a preferred polarization. Even for smooth regions which have no sharp irregularities or small objects, the depolarization is expected to be different because the lunar surface is likely to be inhomogeneous and the orientation of the polarization plane with respect to the normal to the mean surface varies over all angles at any range. Thus the individual vector components will be independent. It is also reasonable to assume that the distribution of orientations will be symmetrical about the direction of the expected polarization component since there should be just as many elements that depolarize in one direction as in the other.

This vector sum is analogous to the sum of a large number of random phase and amplitude sine waves expressed as phasors. Even though the amplitudes of the individual vector components may be correlated with their phases, the orthogonal components of the sum will be uncorrelated so long as the orientation distribution is symmetrical about one of them and the individual vectors are independent [Beckmann and Spizzichino, 1963]. Thus, it is very unlikely that the expected and depolarized components are correlated at all.

The assumption of perfect linear polarization from the antennas was made to simplify the analysis of the ionospheric effects on the signals. The antennas undoubtedly had some cross-polarization, but unfortunately the degrees of polarization linearity have never been measured. They are estimated as being better than 20 dB.

The polarizations of the transmitted waves are undoubtedly elliptical, and can be resolved into two perpendicular linearly polarized waves. Choosing one of these to be along the major axis of the ellipse and normalizing it to unity, the other, or cross-polarized component will have an amplitude a and a phase shift of $\pm 90°$. Since it does not change the results we will choose $+90°$ for convenience here and write the ratio of the cross-polarized to major axis components as ja. Both the major and cross-polarized waves will be reflected and depolarized, so the echo will have four components, as shown in Fig. 32. The expected polarization components of the echoes are denoted by "E" and the depolarized components by "D"; the parts of the echo coming from the cross-polarized component of the transmitted signal are distinguished by the "c" subscript.

All four echo components will undergo the same amount of Faraday rotation Ω, so different amounts of each will be extracted by the antenna, whose response in the orthogonal linear polarization directions is the same as the amplitude and phase of the transmitted waves. Since it is very possible that there will be phase shifts between the echoes from major and cross-polarized transmitted waves, the four echo components should be written as E, D, $jaE_c = jabe^{j\phi}E$, and $jaD_c = jade^{j\theta}D$, where b and ϕ account for possible amplitude and phase differences

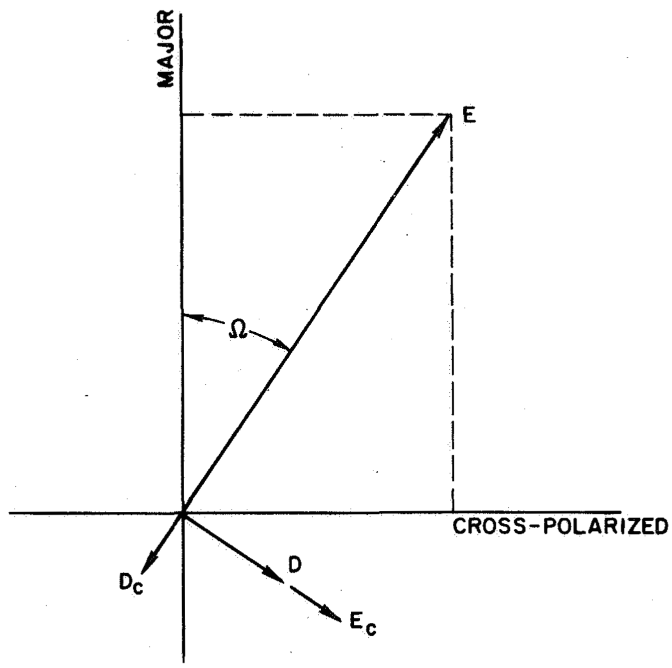

Fig. 32. THE FOUR COMPONENTS OF THE LUNAR ECHOES ARISING FROM AN IMPERFECTLY POLARIZED ANTENNA. E and D are from the major linearly polarized component of the transmitted wave, and E_c and D_c are from the cross-polarized component. They are shown projected onto the major and cross-polarized axes of the antenna after undergoing a Faraday rotation Ω.

the scattering between E and E_c, as do d and θ for D and D_c. Thus the overall response of the antenna is (see Fig. 32)

$$
\begin{aligned}
R &= E \cos \Omega - E_c \sin \Omega + jaE \sin \Omega + jaE_c \cos \Omega \\
&\quad - D \sin \Omega - D_c \cos \Omega + jaD \cos \Omega - jaD \sin \Omega \\
&= E \cos \Omega(1 - a^2be^{j\phi}) + jaE \sin \Omega(1 - be^{j\phi}) \\
&\quad - D \sin \Omega(1 - a^2de^{j\theta}) + jaD \cos \Omega(1 - de^{j\theta})
\end{aligned} \tag{4.11}
$$

Now, since $a^2 \ll 1$ because the cross-polarized component is small, this expression becomes

$$R = E \cos \Omega + jaD \cos \Omega(1 - de^{j\theta})$$

$$- D \sin \Omega + jaE \sin \Omega(1 - be^{j\phi}) \qquad (4.12)$$

The first and third terms are those of a perfectly linearly polarized antenna. Note that if there is no difference between the scattering of the major and cross-polarized transmitted waves, then $b = d = 1$ and $\phi = \theta = 0$, and the other two terms vanish. This is the situation for the quasi-specular component of the echoes, which is only slightly depolarized and is the source of high values of the E component. Therefore the measurement of the quasi-specular component is not affected by an imperfectly polarized antenna (as long as $a^2 \ll 1$); also, measurement of the diffuse D component is not affected by the high quasi-specular E component.

Because the amplitude of the echo should be independent of the orientation of the incident polarization plane, $b = d = 1$. This is so because a very large number of individual scatterers contribute to the total echo and their distribution over the surface is assumed to be homogeneous. The phase, however, does depend on the orientation. A good example of this is when circular polarization is used, for which $a = 1$. If the surface only causes circular depolarization, $\phi = 0$ but $\theta = \pi$, so Eq. (4.11) reduces to

$$R = -2D \sin \Omega + j2D \cos \Omega$$

and $|R| = 2D$. Thus the antenna responds only to the circular depolarization and not at all to the expected component, which even for a plane, perfectly conducting reflector has its sense of circular polarization reversed.

The measurements of depolarization of linearly polarized signals at 23 cm [Evans and Hagfors, 1966] showed that Φ_D/Φ_E was less than 0.2, and the preliminary results here also show that Φ_D is considerably less than Φ_E. Therefore, since a is probably less than 0.1, the second term in Eq. (4.12) is negligible compared to the first and third terms and can be ignored. The last term in Eq. (4.12) is then the important one in reducing the ability to measure Φ_D. Its magnitude is on the order of $a^2\Phi_E$, which may be equal to or greater than Φ_D. However, the problem is greatest when Φ_E/Φ_D is large, but that happens for the quasi-specular portion of the echo where the $(1 - be^{j\phi})$ factor is very small. It should finally be noted that the estimation of the power in each term of Eq. (4.12) can be done separately since the estimating procedure discriminates against the cross terms as pointed out above. The conclusion here is that the lack of perfectly linearly polarized antennas is not very damaging to these measurements.

There is one other subject that should be considered. This is the effect of the progressive rotation of the incident polarization plane due to the Faraday rotation. The amount of polarization rotation is half of the amount measured at the antenna and was about 75° at 25 MHz for the data analyzed here. Since the low resolution analysis only used one-tenth of the full sweep duration, the change was about 7.5° for those results. At 50 MHz, these quantities are reduced by a factor of 1/8. The data windows reduce the effective amount of rotation because the extremes of the rotation have low weights.

The assumption made is that this rotation does not affect the scattered field. Only for the high resolution 25 MHz echoes where the rotation is large would this assumption be invalid. However, the high resolution analysis was done to study the quasi-specular component of the echoes, which is very insensitive to the polarization of the incident waves. Also, the rotation does not cause any systematic changes because all orientations of the polarization plane to the mean surface are always present at any range interval. The main effect of the rotation is therefore to reduce the resolving ability of the spectral analysis because the effective signal durations are reduced for the polarization-orientation-sensitive echo components. Since high resolution is only needed at the leading edge of the expected polarization component where the scattering is mostly specular and not very sensitive to polarization orientation, this is a completely unimportant effect.

C. Separation of the Expected and Depolarized Echo Components

After the preliminary processing, the data consists of a large number of individual spectra, one for each echo or the portion of an echo analyzed. Each of these spectra is the sum of the noise, the expected component, and the depolarized component as described by Eq. (4.6). In particular, the i^{th} estimated spectrum when normalized by U is

$$\hat{P}_i(n\Delta f) = \frac{1}{2}[1 - V \cos (2\phi_i)] \hat{P}_{E_i}(n\Delta f)$$

$$+ \frac{1}{2}[1 + V \cos (2\phi_i)] \hat{P}_{D_i}(n\Delta f) + \hat{P}_{N_i}(n\Delta f)$$

$$= \frac{1}{2}[\hat{P}_{E_i}(n\Delta f) + \hat{P}_{D_i}(n\Delta f) + 2\hat{P}_{N_i}(n\Delta f)]$$

$$- \frac{V}{2} \cos (2\phi_i)[\hat{P}_{E_i}(n\Delta f) - \hat{P}_{D_i}(n\Delta f)] \tag{4.13}$$

Because the phase of the Faraday modulation can be measured for each echo, the weights in the sum are known. Therefore the estimates $\hat{P}_E(n\Delta f)$ and $\hat{P}_D(n\Delta f)$ can presumably be computed from a combination of three individual spectra, or from a combination of three (possibly weighted by the U's) averages of different spectra. Any of these lead to three equations with three unknowns, $\hat{P}_E(n\Delta f)$, $\hat{P}_D(n\Delta f)$, and $\hat{P}_N(n\Delta f)$, whose coefficients are functions of the U's. Unfortunately it is impossible to obtain these estimates because the weights U_E, U_D, and U_N are linearly related. Thus, for any set of three equations the determinant will have linearly related columns and will be zero. Combinations of the estimates $\widehat{P_E(n\Delta f) - P_D(n\Delta f)}$, and $\widehat{P_E(n\Delta f) + P_D(n\Delta f) + 2P_N(n\Delta f)}$ are the only ones that can be made from this data. It is therefore necessary that the background noise, which can be estimated from ranges not occupied by the moon, be subtracted from the latter estimate to obtain $\hat{P}_E(n\Delta f)$ and $\hat{P}_D(n\Delta f)$. In practice, this is difficult to do satisfactorily because small residual errors in $\hat{P}_N(n\Delta f)$ have a very large effect.

The simplest estimators of these two quantities involve the unweighted sums of the computed spectra, $P(n\Delta f)$, which are divided into two groups. Denoting one of the groups by the subscript i and the other j, these estimators are

$$\widehat{P_E - P_D} = \frac{2}{V} \frac{N\sum_{i=1}^{M} P_i - M\sum_{j=1}^{N} P_j}{M\sum_{j=1}^{N} \cos(2\phi_j) - N\sum_{i=1}^{M} \cos(2\phi_i)}$$

and (4.14)

$$\widehat{P_E + P_D + 2P_N} = 2\, \frac{\sum_{i=1}^{M} \hat{P}_i \sum_{j=1}^{N} \cos(2\phi_j) - \sum_{j=1}^{N} \hat{P}_j \sum_{i=1}^{M} \cos(2\phi_i)}{M\sum_{j=1}^{N} \cos(2\phi_j) - N\sum_{i=1}^{M} \cos(2\phi_i)}$$

where M is the number of spectra in the "i" group and N the number in the "j" group, V is given by Eq. (4.4), and ϕ is the phase of the Faraday modulation of the center of the echo relative to the null position. The arguments of the $\hat{P}$'s have been left out of these expressions for clarity. There are similar expressions for $\widehat{P_E + P_N}$ and $\widehat{P_D + P_N}$; but they can also be easily computed from the estimates of Eqs. (4.14).

These estimators are unbiased, and their variances can be found by substituting Eq. (4.13) with the proper subscripts into Eqs. (4.14). For example, with the assumption that all the $\hat{P}_i$'s and $\hat{P}_j$'s are mutually uncorrelated, the variance of $\widehat{P_E - P_D}$ is

$$\mathrm{Var}\left\{\widehat{P_E - P_D}\right\} = \overline{\widehat{P_E - P_D}^2} - \overline{\widehat{P_E - P_D}}^2$$

$$= \left\{V\left[M \sum_{j=1}^{N} \cos(2\phi_j) - N \sum_{i=1}^{M} \cos(2\phi_i)\right]\right\}^{-2}$$

$$\times \left\{\left[N^2 \sum_{i=1}^{M} [1 - V\cos(2\phi_i)]^2 + M^2 \sum_{j=1}^{N} [1 - V\cos(2\phi_j)]^2\right] \overline{\hat{P}_E^2}\right.$$

$$+ \left[N^2 \sum_{i=1}^{M} [1 + V\cos(2\phi_i)]^2 + M^2 \sum_{j=1}^{N} [1 + V\cos(2\phi_j)]^2\right] \overline{\hat{P}_D^2}$$

$$\left. + (N^2M + M^2N)\, \overline{\hat{P}_N^2}\right\} - \left(\overline{\hat{P}_E} - \overline{\hat{P}_D}\right)^2 \tag{4.15}$$

The expressions for the other variances are even more complicated, and also involve the quantities

$$\overline{\hat{P}_E^2},\quad \overline{\hat{P}_E},\quad \overline{\hat{P}_D^2},\quad \overline{\hat{P}_D},\quad \overline{\hat{P}_N^2},\quad \overline{\hat{P}_N}$$

which are for individual spectral estimates and are determined by the lunar scattering properties. The assumption of mutual uncorrelation between spectra is not damaging, although it is not true because there is some correlation between them. However, only the spectra from adjacent echoes are likely to be significantly correlated. Since adjacent echoes have nearly the same value of ϕ, Eq. (4.15), when modified to include the correlation function between echoes, essentially retains its form.

By properly dividing the entire set of raw spectra into the "i" and "j" groups, the variances of the estimates can be minimized. Because of the complexity of the variance expressions this is a difficult optimization to perform. One immediately apparent possibility is to maximize the denominator of Eq. (4.15), which is the denominator of all the variance expressions. An obvious starting point would be to place all the spectra with positive values of $\cos(2\Phi)$ into one group and the negatives into the other.

Using this as the starting point, a computerized procedure was developed to optimize the division. It tested the actual values of the Φ's from the data to see whether the corresponding spectrum belonged in the group it was already in, in the other, or in none at all. This was done iteratively, with the spectrum tested being the one with the smallest value of $\cos(2\Phi)$ remaining in the group, since it had the least effect. This heuristic approach was successful in optimizing the division in a reasonably short amount of time although the program was relatively complicated. The results of such trials showed that the reductions (typically less than 10 percent) in the variances from the starting point were not significant to justify the optimization, so the starting point was used for all divisions. Comparisons with other more complicated estimators showed that the one chosen here generally resulted in smaller variances although the differences were not large.

Actually, the expressions like Eq. (4.15) for the variances can be somewhat simplified by noting that

$$\overline{\hat{P}_D^2} \ll \overline{\hat{P}_E^2}$$

because $\overline{\hat{P}_E}$ is considerably larger than $\overline{\hat{P}_D}$, and $\overline{\hat{P}^2} \approx \overline{\hat{P}}^2$ for individual spectral estimates. Thus only the expected and noise components have to be considered in the optimization. Since there are three sections of each spectrum:

$$(1)\quad \overline{\hat{P}_E}^2 \gg \overline{\hat{P}_N}^2 \;; \qquad (2)\quad \overline{\hat{P}_E} \approx \overline{\hat{P}_D} \;; \qquad (3)\quad \overline{\hat{P}_N^2} \gg \overline{\hat{P}_E^2}$$

a different optimization should be used for each section. The minor improvements available with the optimization would not have justified all that effort.

This simple division of the spectra also insures that any cospectrum term between Φ_E and Φ_D will have zero average. Each summation in Eqs. (4.14) will span a zero-average half cycle of the weight function on Φ_{ED}.

Figures 33 through 36 show some of the high resolution results from the 24 August 1965 run. All these plots are normalized to the highest value in each set of data, and are consistent in the same wavelength and resolution groups. The normalizations are close for the same wavelength but different resolution because the analyses were done on the same data and the gains in the digitizing system were maintained to very nearly the same value. The gaps in the decibel plots are from negative estimate values. These estimates are based on 342 individual spectra spanning about 30 min of time. Figure 35 shows the $\widehat{P_E + P_N}$ and $\widehat{P_D + P_N}$ estimates on the same axes for both 6 and 12 m. The different values of $\hat{P}_N$ before the echo are partly due to power spectral analysis sidelobe response and partly to different average noise levels in the two groups of spectra. Both effects are more pronounced at 12 m than at 6 m because the background noise is lower relative to the echo, and is less stationary at 12 m. Even though the 6 m background noise is higher, as can be seen from the $\widehat{P_E + P_D + 2P_N}$ estimates, it is evidently more stationary because better cancellation was obtained at 6 m in the $\widehat{P_E - P_D}$ estimates than at 12 m. The success of this separating technique and of the entire analysis is evident from the comparison of the expected and depolarized components in Figs. 35 and 36, where they are plotted in terms of relative power to show part of the negative-valued estimates. The negative values are the result of the estimates being the small difference between large numbers. Although the variance of the depolarized estimates is large at the leading edge because it is proportional to $\hat{P}_E^2$ which is very large there, the mean level of $\widehat{P_D + P_N}$ does not appear to increase there.

The low resolution results are similar. Figure 37 shows the 12 m $\widehat{P_E - P_D}$ and $\widehat{P_E + P_D + 2P_N}$ estimates, which have been corrected for the frequency response of the receiver and the recording process, and are formed from about 1300 individual spectra spanning 20 min of echoes.

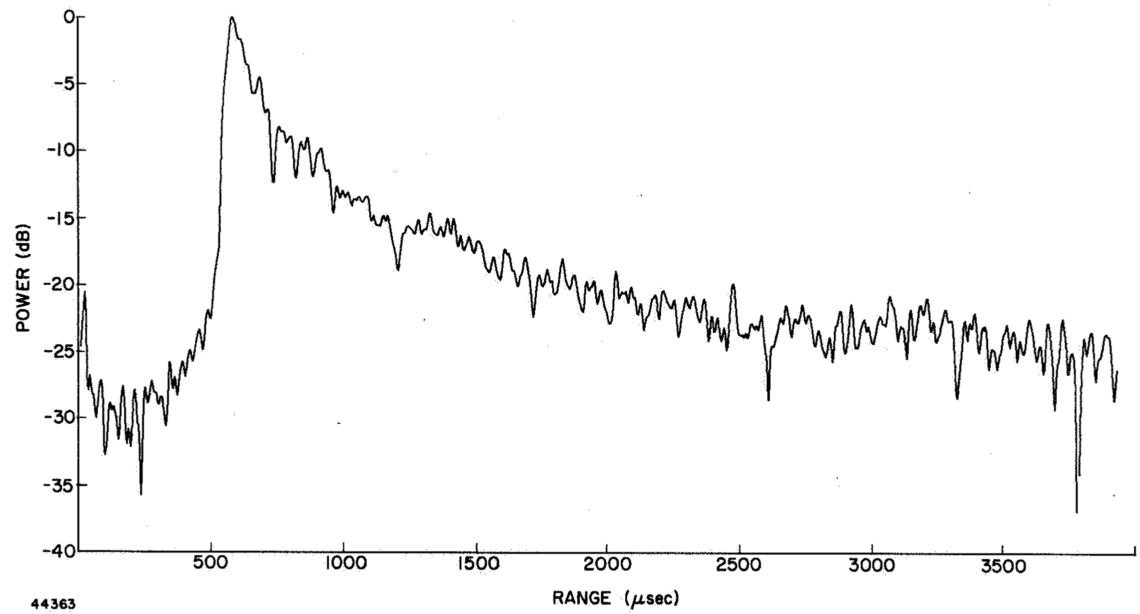

a. $\widehat{P_E - P_D}$ normalized to 510.2

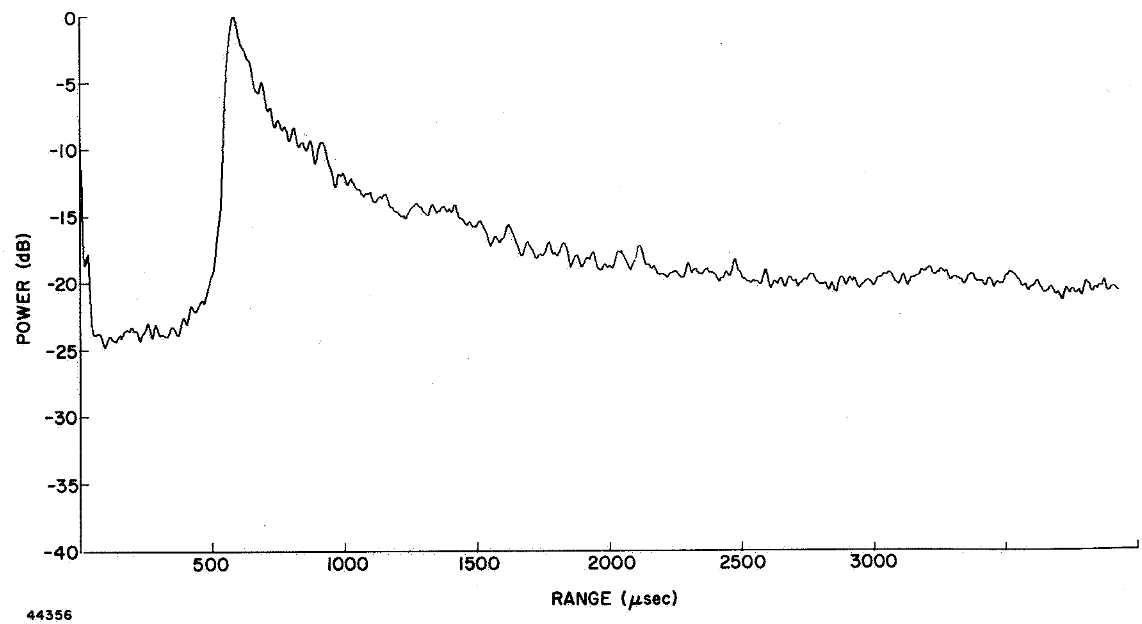

b. $\widehat{P_E + P_D + 2P_N}$ normalized to 453.7

Fig. 33. HIGH RESOLUTION 12 m ESTIMATES FROM RUN OF 24 AUGUST 1965.

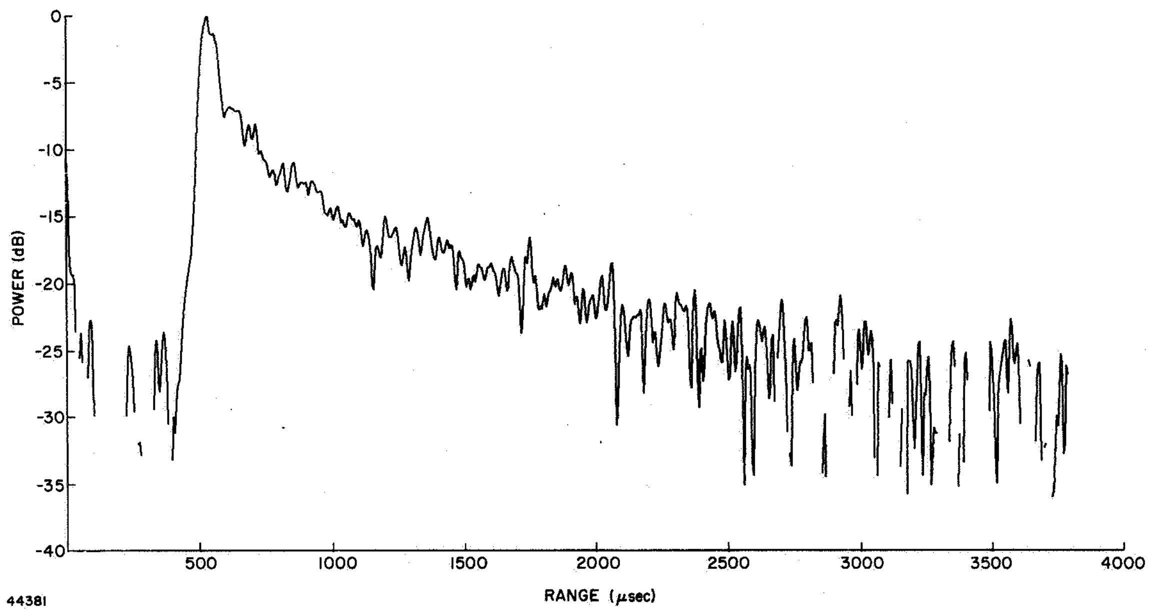

a. $\widehat{P_E - P_D}$ normalized to 369.6

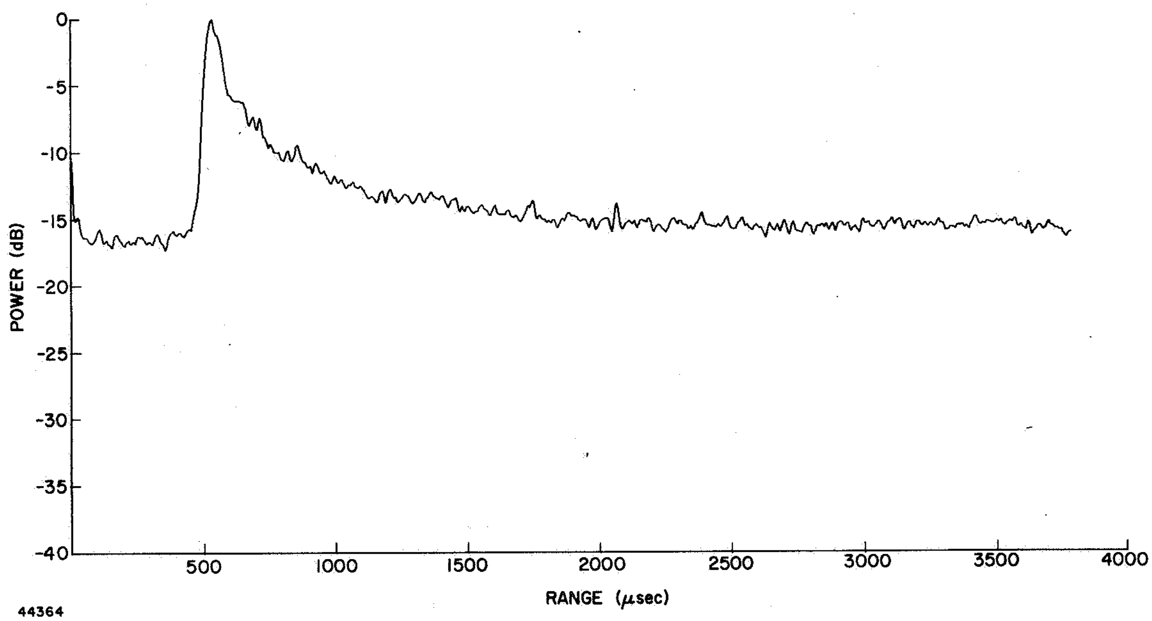

b. $\widehat{P_E + P_D + 2P_N}$ normalized to 326.5

Fig. 34. HIGH RESOLUTION 6 m ESTIMATES FROM RUN OF 24 AUGUST 1965.

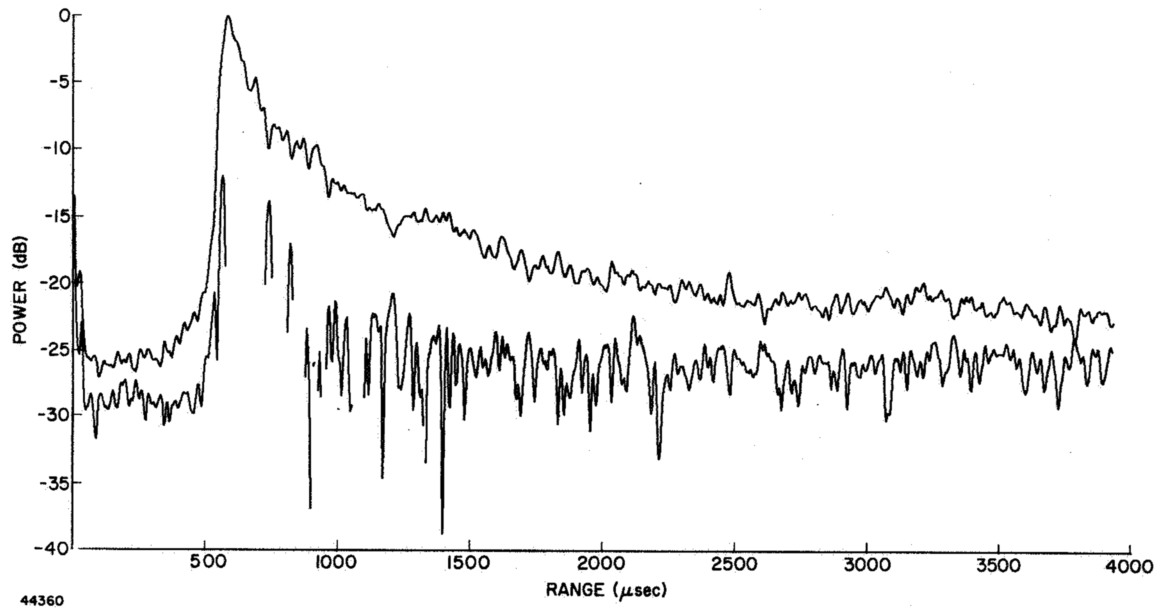

a. 12 m; normalized to 476.4

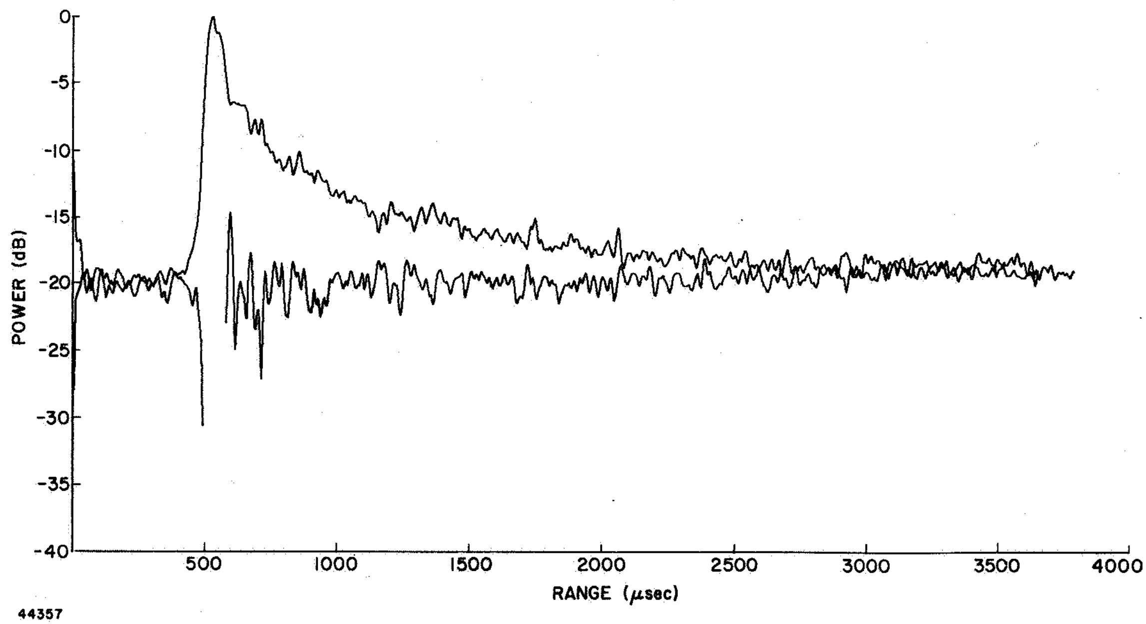

b. 6 m; normalized to 348.1

Fig. 35. SUPERIMPOSED $\widehat{P_E + P_N}$ AND $\widehat{P_D + P_N}$ HIGH RESOLUTION ESTIMATES FROM RUN OF 24 AUGUST 1965. Both curves normalized to $\widehat{P_E + P_N}$, the upper curve.

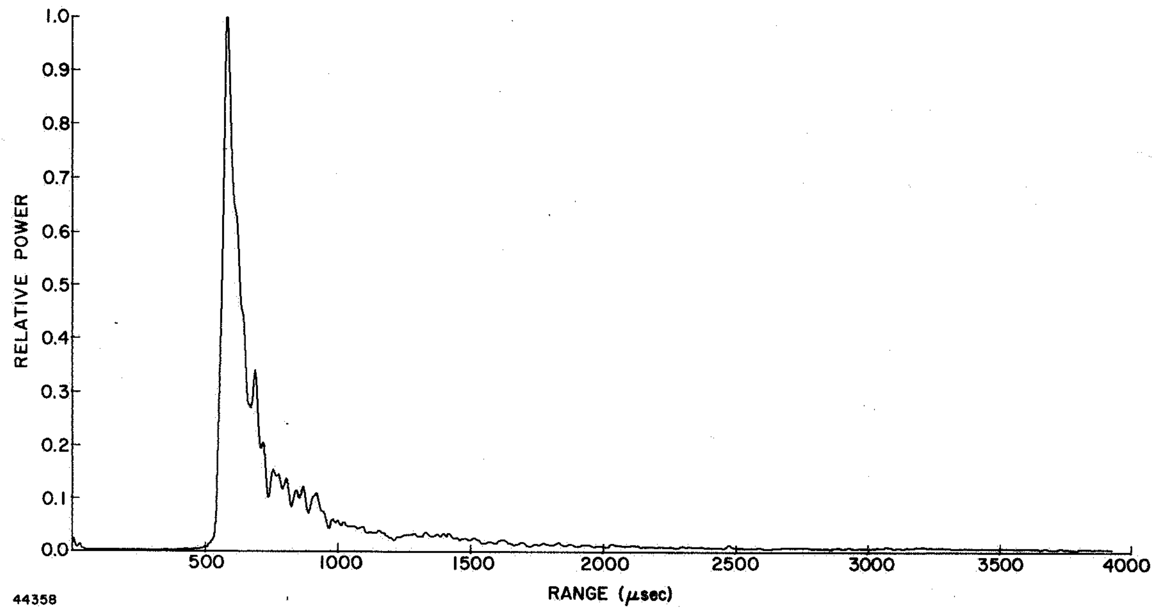

a. $\widehat{P_E + P_N}$ normalized to 476.4

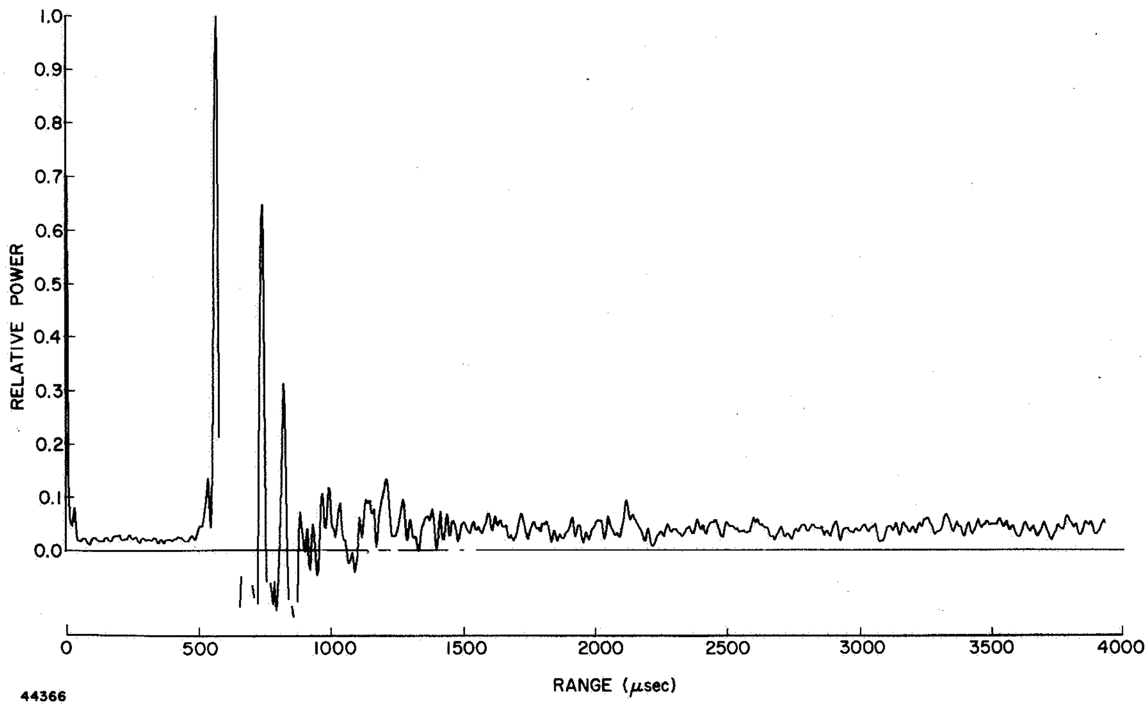

b. $\widehat{P_D + P_N}$ normalized to 30.00

Fig. 36. RELATIVE POWER PLOTS OF HIGH RESOLUTION 12 m ESTIMATES FROM RUN OF 24 AUGUST 1965.

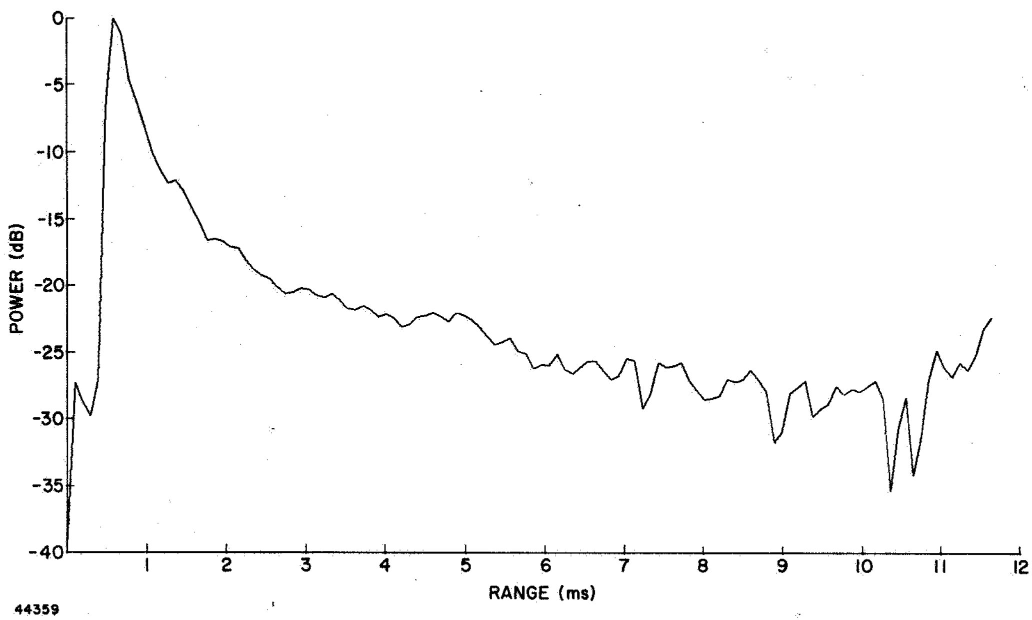

a. $\widehat{P_E - P_D}$ normalized to 218.5

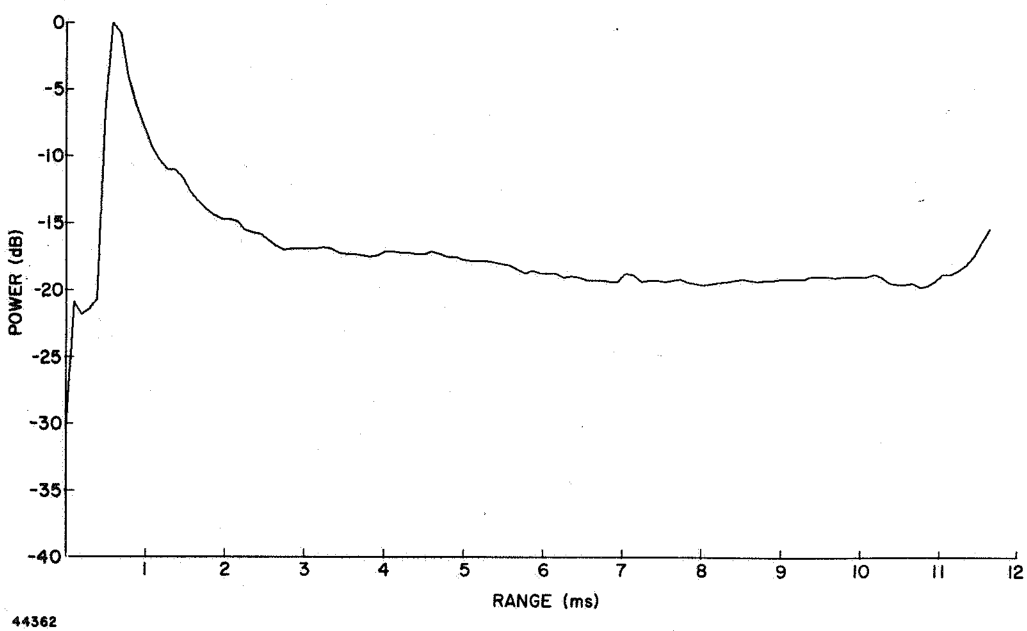

b. $\widehat{P_E + P_D + 2P_N}$ normalized to 219.8

Fig. 37. LOW RESOLUTION 12 m ESTIMATES FROM RUN OF 24 AUGUST 1965 COMPENSATED FOR FREQUENCY RESPONSE OF RECEIVER AND RECORDING PROCESS.

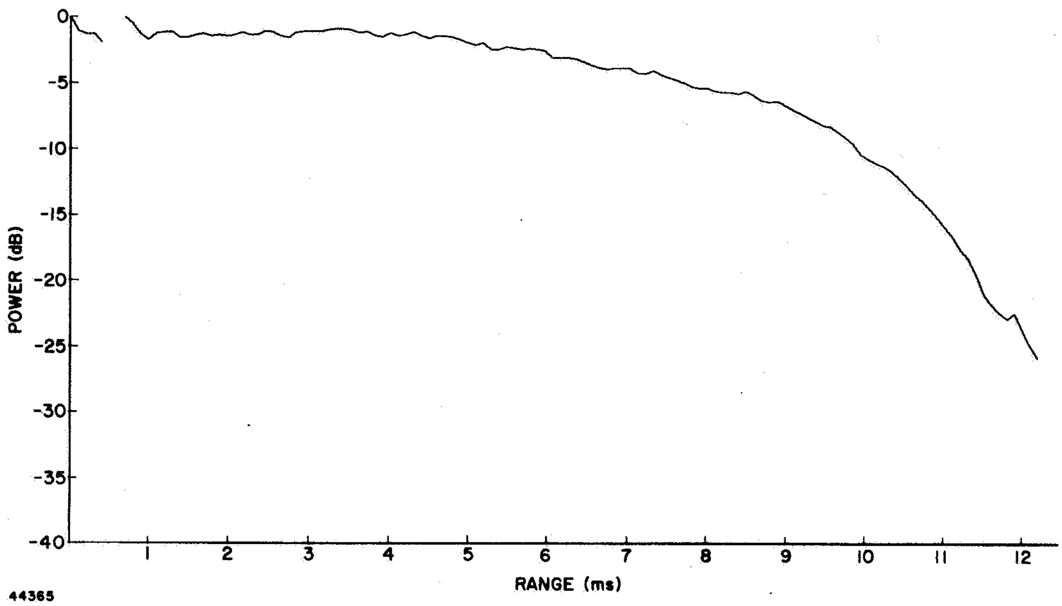

a. $\widehat{P_D + P_N}$ normalized to 4.40. This is essentially P_N alone.

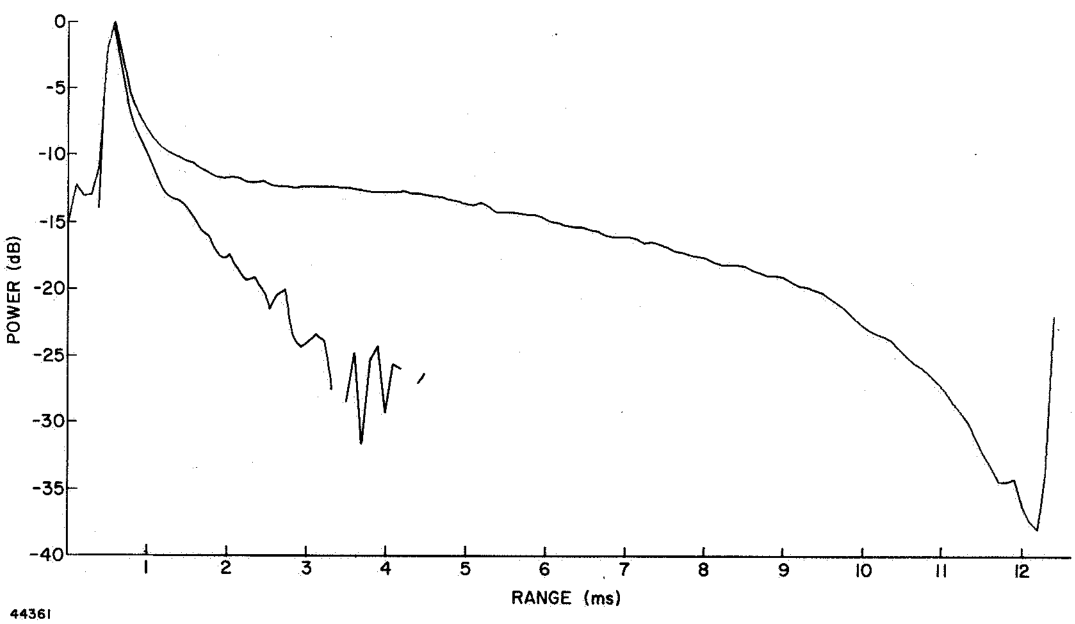

b. $\widehat{P_E - P_D}$ and $\widehat{P_E + P_D + P_N}$ superimposed and both normalized to 128.5. The lower plot is $\widehat{P_E - P_D}$.

Fig. 38. LOW RESOLUTION 6 m ESTIMATES FROM RUN OF 24 AUGUST 1965.

This response was measured by analyzing a series of noise-only records from a day when the 25 MHz transmitter failed, and therefore is not completely accurate since the receiver bandpass characteristic is not exactly symmetrical as noted in Chapter II. The rise at the extreme range is caused by a small component of the background noise which did not pass through the entire system but was introduced at later points, such as in the recording and playback processes or in the analog-to-digital conversion equipment. Since the frequency response compensation is large at the extreme range, this component becomes greatly exaggerated there. It is clear that there was not sufficient sensitivity to make good measurements beyond a range of 5 or 6 ms out of the moon's entire range depth of 11.6 ms.

Unfortunately, no noise-only section of data of sufficient duration was available at 6 m. The background noise, however, was much larger compared to the echo than at 12 m, so the depolarized component is completely masked, which is apparent in Fig. 35b. Thus an estimate $\widehat{P_D + P_N}$ is essentially an estimate of the noise alone. This estimate is shown in Fig. 38a; the 6 m low resolution uncompensated $\widehat{P_E - P_D}$ and $\widehat{P_E + P_D + 2P_N}$ estimates are superimposed in Fig. 38b.

The final step in the data analysis is the subtraction of the background noise. This is difficult to do very satisfactorily. Even for the $\widehat{P_E - P_D}$ estimates there is a small amount of residual noise, and for the 12 m spectra the sidelobe response confuses the background noise measurement. There is also the problem of noise components from different sources in the system. Since all the noise has not passed through the entire system, the output noise is a sum of components having different spectral characteristics. For the low resolution data the background noise level was estimated by performing a minimum mean square error fit on the extreme range end of the spectral estimates. The noise was assumed to come from two sources: the first passed through the entire system and the second entered just before the spectral analysis and had a flat spectral characteristic.

The noise level for the high resolution spectra was estimated from the $\widehat{P_D + P_N}$ curve before the peak since sidelobe response is not apparent there inasmuch as it is associated with the high expected echo component. Since the high resolution data is mainly used to correct the behavior of the low resolution $\hat{P}_E$ estimate at the peak and to compare the behavior of $\hat{P}_E$ at the peak for different subradar points, the background level is usually negligible because it is very much smaller than $\hat{P}_E$. For the high resolution $\hat{P}_D$ estimate where the background noise is significant, its measurement can be performed more accurately.

Chapter V

RESULTS, INTERPRETATIONS, AND CONCLUSIONS

A. Introduction

Although the lack of sufficient sensitivity prevented measurements of the backscattering behavior of the moon over its entire range depth, useful and accurate measurements have been made of the leading edge behavior at both wavelengths. The measurements encompass the quasi-specular region and extend to a range of 5 or 6 ms, which is about one-half the entire range depth. The behavior of the depolarized component of the echoes could only be estimated at 12 m because the sensitivity of the 6 m radar was less than that of the 12 m radar. Since the quantities which specify the signal-to-noise ratio of the receiver output signal are the same for both radars (except for the cosmic noise level and the transmitted power, which have approximately the same ratio at the two wavelengths and therefore cancel), their sensitivities should be nearly equal. The observed difference must be due to a difference in the interference noise level or to an increase in the radar cross section at the longer wavelength.

Several important results have been obtained from these measurements. First, no essential difference between the quasi-specular component at the two wavelengths could be seen. Both appear to follow the 68 cm [Evans and Pettengill, 1963] results more closely than they do the previous 6 m [Klemperer, 1965] results, and are considerably different than the 11.3 m [Davis and Rohlfs, 1964] curve. Second, the strength of the echo at the leading edge is very sensitive to the location of the sub-radar point. A difference of nearly 5 dB was seen between the results from the 20 August and 24 August runs. Third, the ratio of the depolarized to expected echo components is considerably higher at 12 m than it is reported to be at 23 cm [Evans and Hagfors, 1966].

B. Results

A composite plot of the high and low resolution 12 m, 24 August results is shown in Fig. 39. The upper set of lines is the expected

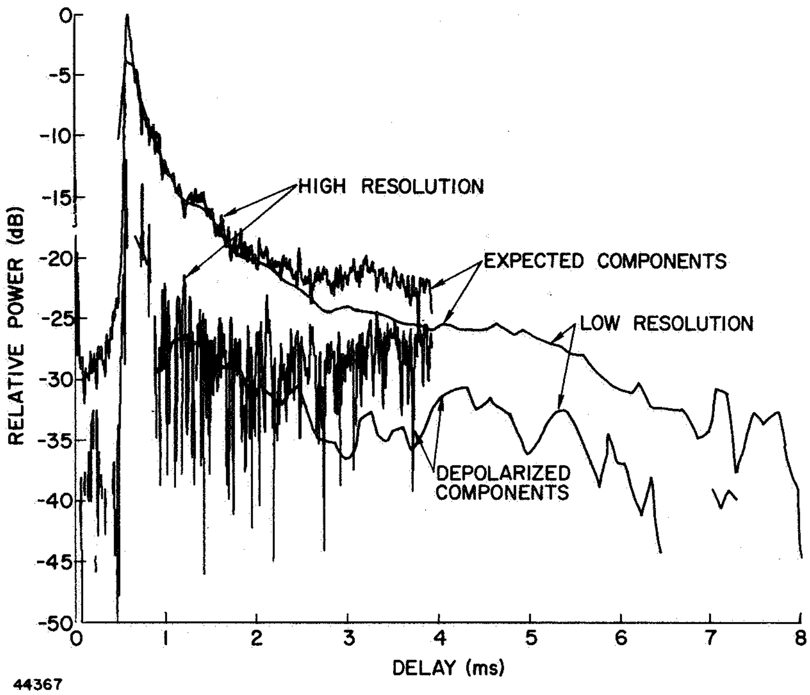

Fig. 39. SUPERIMPOSED HIGH AND LOW RESOLUTION 12 m RESULTS FROM THE RUN OF 24 AUGUST 1965. The resolutions are approximately 22 and 200 μs.

component and the lower set is the depolarized component. The disagreement between the high and low resolution plots in both components around 3 to 4 ms delay is probably due to differences in the playback and filtering responses before the data were digitized. In Fig. 40 is a similar plot of the 6 m results excluding the depolarized component which could not be separated from the background noise. The curves of Figs. 41 and 42 were obtained by drawing smooth lines through the raw results of Figs. 39 and 40. In the 12 m case the lines were drawn approximately between the high and low resolution results because the former appears to be too high and the latter seems equally too low in the range around a delay of 2.5 to 3.0 ms.

The ratio of the depolarized to expected components was obtained directly from the raw results; this ratio for the high resolution data is plotted in Fig. 43a, and a running mean of it is shown in Fig. 43b. It is apparent from Fig. 44, which is a superimposed plot of the high

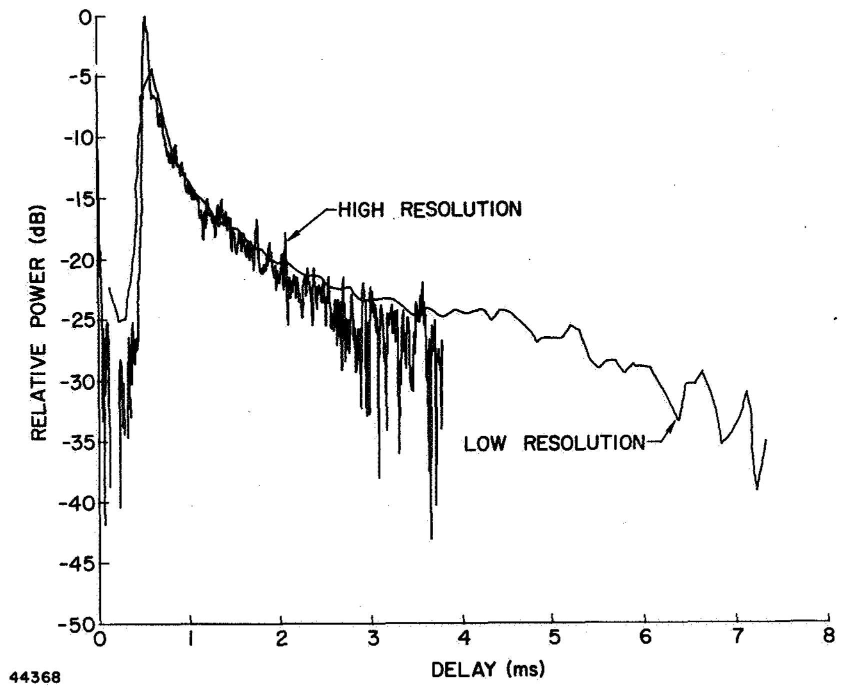

Fig. 40. SUPERIMPOSED HIGH AND LOW RESOLUTION 6 m RESULTS FROM THE RUN OF 24 AUGUST 1965. The resolutions are approximately 20 and 200 μs.

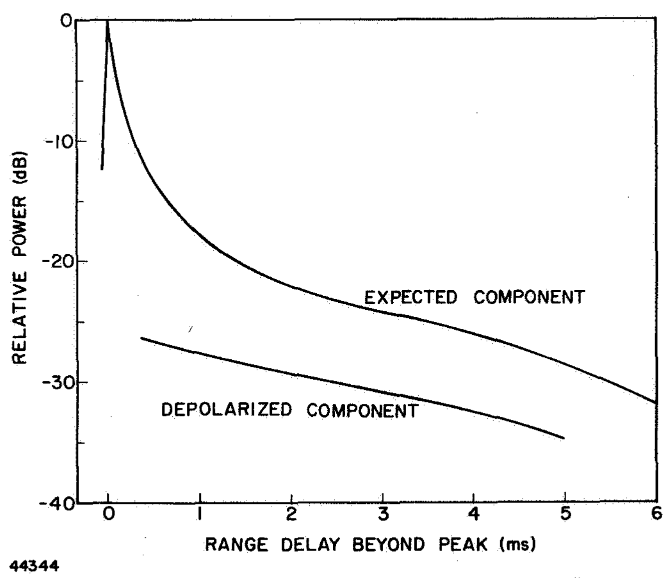

Fig. 41. THE SMOOTHED 12 m RESULTS FROM THE RUN OF 24 AUGUST 1965. The curves are a composite of the high and low resolution results of Fig. 39 and effectively have a resolution of about 22 μs.

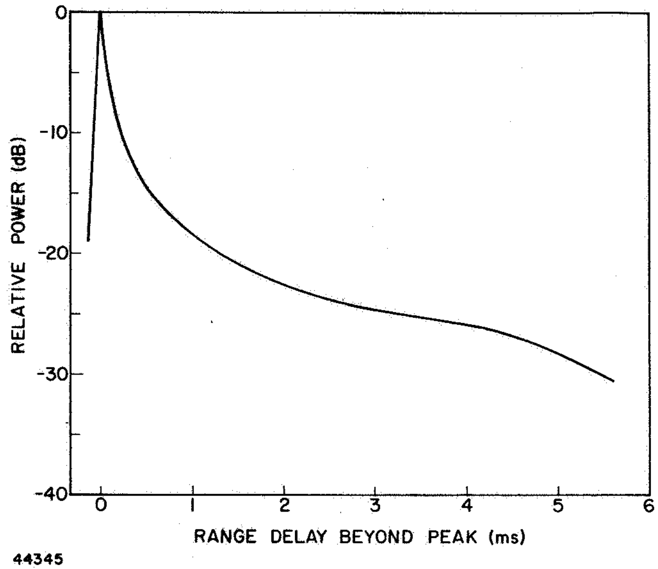

Fig. 42. THE SMOOTHED 6 m RESULTS FROM THE RUN OF 24 AUGUST 1965. Only the expected component is shown. The curve is a composite of the high and low resolution results of Fig. 40 and has an effective resolution of about 20 μs.

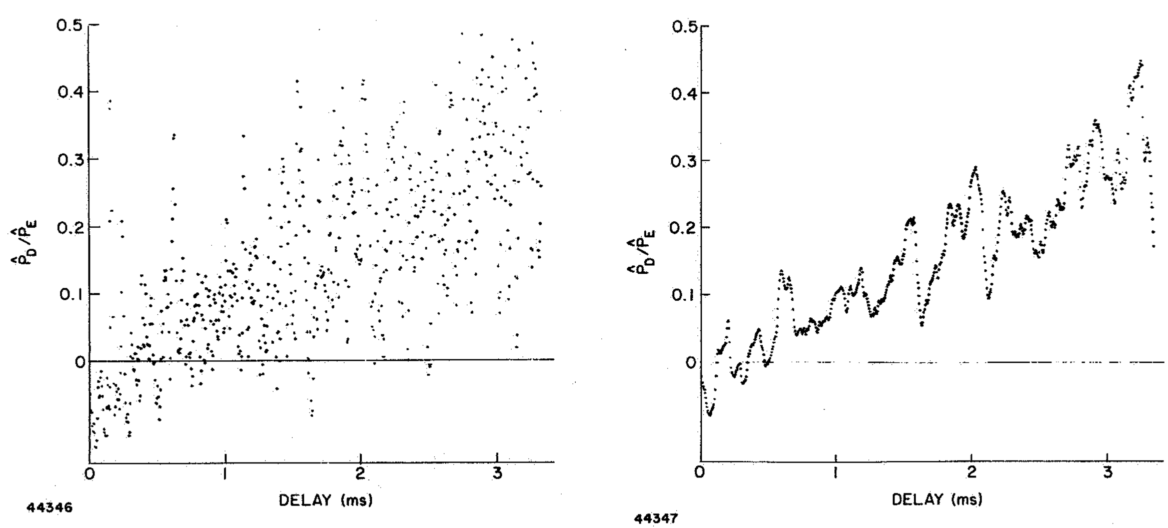

a. The ratio of the raw estimates

b. A running mean (of 21 points) of the data shown in part (a)

Fig. 43. THE RATIO OF THE DEPOLARIZED TO EXPECTED LINEARLY POLARIZED ECHO COMPONENTS AT 12 m FOR THE HIGH RESOLUTION DATA OF 24 AUGUST.

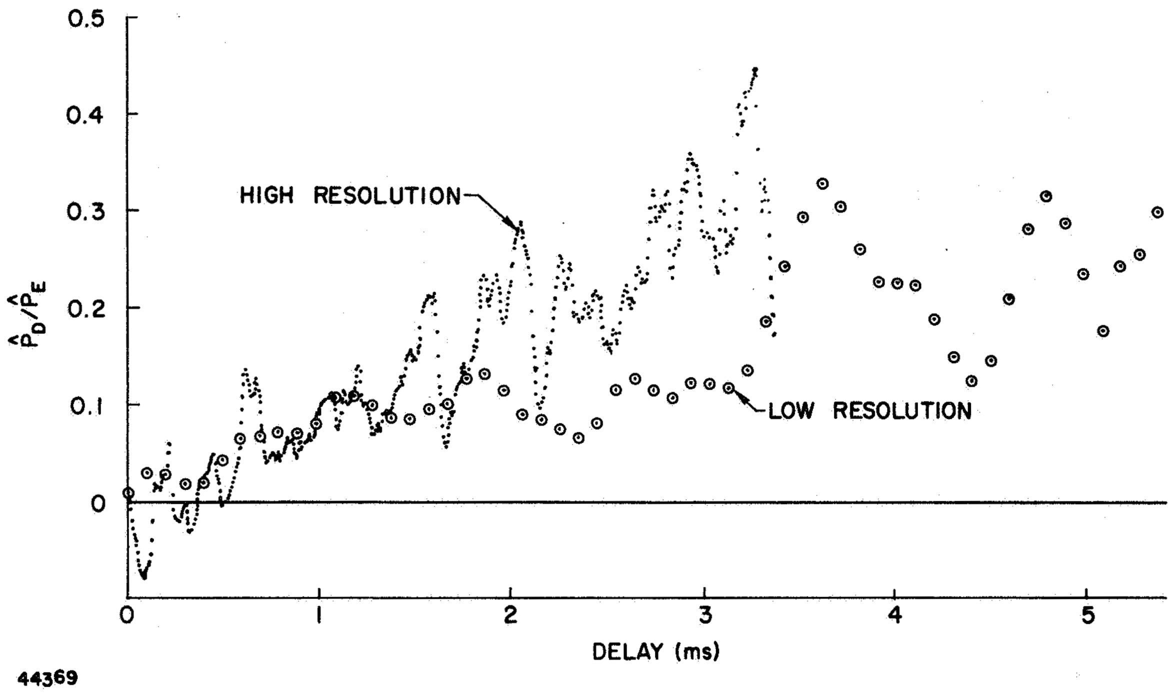

Fig. 44. THE RATIO OF THE DEPOLARIZED TO EXPECTED ECHO COMPONENTS AT 12 m FOR THE RUN OF 24 AUGUST. Both a 21-point running mean of the high resolution ratio and a 3-point running mean of the low resolution ratio are shown.

resolution and low resolution depolarized to expected component ratios, that the ratio increases approximately linearly from the leading edge. The difference between the high and low resolution data around 2.5 ms delay is again noticeable in this figure, making an accurate measurement of the ratio impossible there. It appears that after increasing linearly, the ratio levels off at a delay of about 2.5 ms and maintains a value of approximately 0.2 after that.

The final results are shown in Fig. 45, which presents the $\widehat{P_E - P_D}$ estimates for both 6 and 12 m for the two days analyzed. Because the depolarized component is small near the leading edge, these quantities are essentially the quasi-specular expected component alone. The 6 m results for the 20 August run have poor quality because of a great deal of nonstationary background noise which did not properly cancel in the estimates. These particular estimates (i.e., $\widehat{P_E - P_D}$) were chosen for

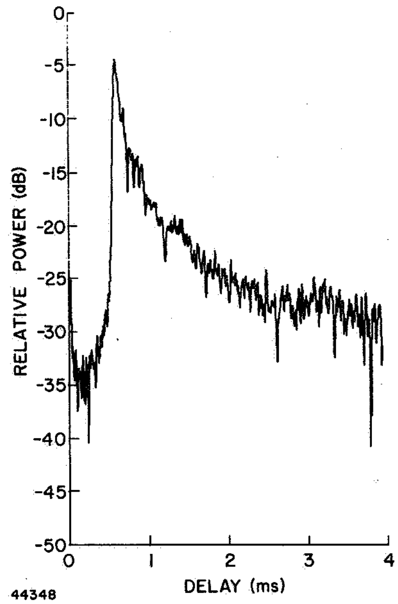

a. From the 12 m, 24 August run

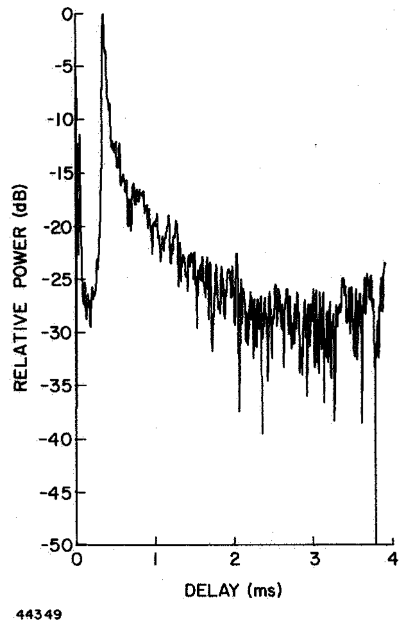

b. From the 12 m, 20 August run

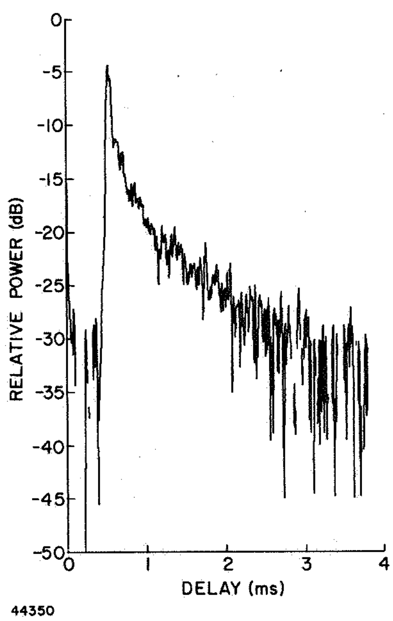

c. From the 6 m, 24 August run

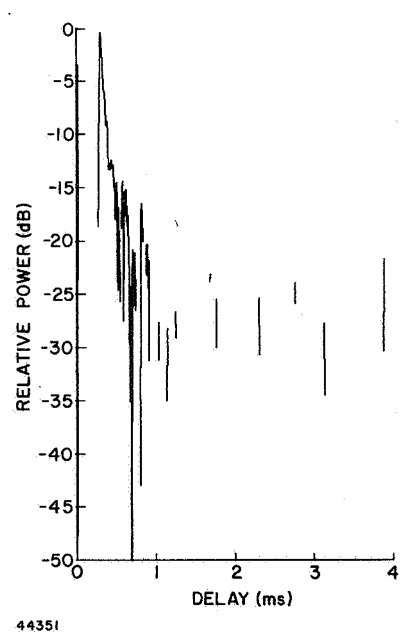

d. From the 6 m, 20 August run

Fig. 45. THE RAW $\widehat{P_E - P_D}$ ESTIMATES FROM TWO DAYS. The similarities between the 6 and 12 m results on the same days are evident. The 24 August points have been moved down 4.5 dB, resulting in a very close match with the 20 August curves beyond the peak.

this comparison because of their inherent noise suppression; this choice eliminated any errors in removing the background noise that would be necessary with the other estimates. Furthermore, if the depolarized component is associated with the diffuse component of the echoes, this estimate partially removes the latter, leaving mainly the quasi-specular component for comparison between the various cases. This technique of subtracting some amount of the depolarized component has been used to compute the surface slope distribution and dielectric constant [Rea, Hetherington, and Mifflin, 1964].

Since the position of the subradar point was different on the two days analyzed, the plots are expected to be different only at the leading edge. At other ranges no difference is expected since each range ring encompasses such a wide variety of lunar terrain that the returned power average should only depend on the range. The curves for each wavelength in Fig. 45 do match very closely except at the leading edge, and the 12 m, 24 August results have been scaled down 4.5 dB in Fig. 45 to the level where they match the 20 August results in the region just beyond the peak.

There is also a very close fit over the entire curve between the 6 and 12 m results on the same days. Although this conclusion is based more strongly on the 24 August results because the 20 August, 6 m results are relatively poor, the fit is apparent for the 20 August data even though it has to be based on a much smaller range interval and is less accurate than the 12 m fit.

C. Comparisons to Previous Results and Conclusions

The results obtained here are compared in Fig. 46 to several previously reported observations at various wavelengths. For the 3.6 cm, 23 cm, and 68 cm curves the pulse lengths were approximately 30 μs [Evans and Hagfors, 1966], while for the 6 m curve the pulse length was 100 μs. Since the equivalent pulse length used here was about 20 μs, our results are comparable in resolution to the shorter wavelength results. The 6 and 12 m results obtained here are so similar that they have been plotted as a single curve.

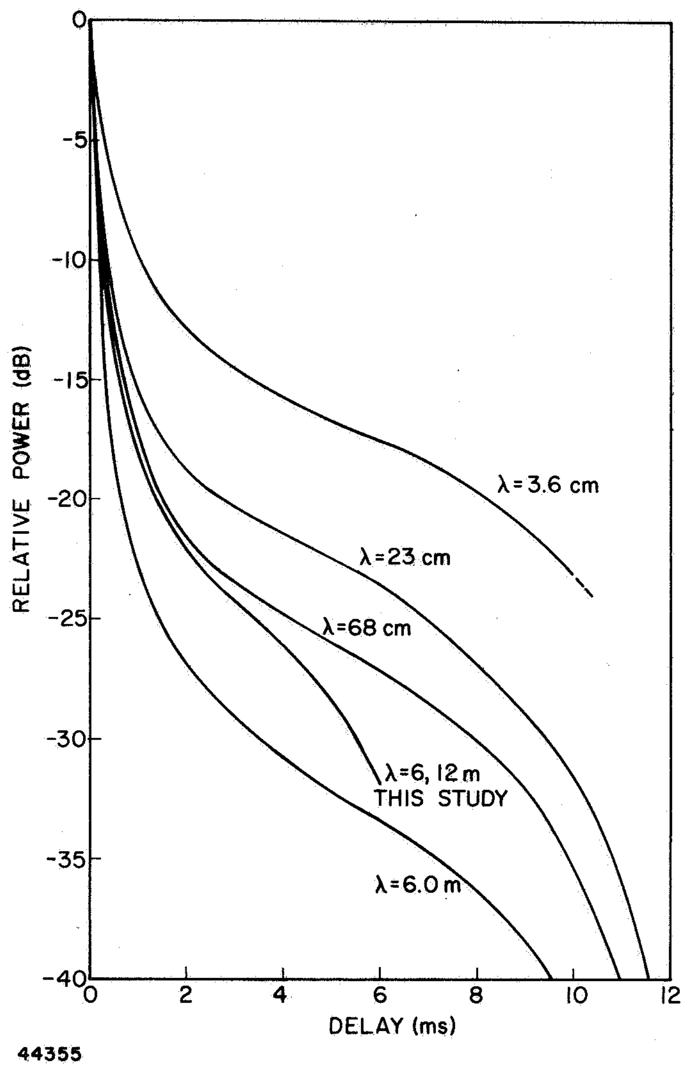

Fig. 46. THE RESULTS OF THE SHORT-PULSE RADAR OBSERVATIONS OF THE MOON AT SEVERAL WAVELENGTHS. All have been normalized to their peak value so the relative positions of the curves for the radar cross section vs delay are likely to be different.

It is apparent that our results do not agree very well with the other observations, particularly beyond a delay of 4 ms. The cause of the anomalous drop at that point is not known, but is possibly a combination of inaccurate background noise subtraction and uncompensated frequency response due to asymmetry in the receiver IF bandpass characteristic. Since both wavelengths are equally affected, it does not seem likely that it could be caused by problems such as antenna misalignment.

The mismatch between these results and Klemperer's [1965] results in the 0 to 4 ms range is more serious. Our results follow the 68 cm curve much more closely than they do Klemperer's 6.0 m curve. Since all the curves of Fig. 46 have been normalized to their peaks, our results should actually lie below Klemperer's because of our shorter pulse length. It should also be pointed out that the 11.3 m observations [Davis and Rohlfs, 1964], which used a pulse length of 250 μs, fall essentially on the 6.0 m curve, the same way that our 6 and 12 m results coincide. Thus our results are even more at variance with the previous observations.

The explanation for this is of fundamental importance for the study of the radio reflecting properties of the moon. First, one should note that the 68 cm, 6.0 m, and 11.3 m curves are the same in the 0 to 3 ms range interval except at the leading edge itself. Thus, if just the peaks of the previous 6.0 and 11.3 m results were 5 dB smaller, those curves would match our results and those for 68 cm; conversely, if our results were 5 dB higher at the peak, they would match the other long wavelength results. As illustrated in Fig. 45, the latter condition occurred for the 20 August run. The peak was 4.5 dB higher that day, so if that data had been plotted in Fig. 46 instead of the 24 August data, these observations would agree with the other long wavelength observations.

The locations of the subradar points for the observations plotted in Fig. 46 are extremely significant. For the 11.3 m results, which were obtained on 29 November 1963 [Davis and Rohlfs, 1964], the subradar point was approximately 6.0°N 3.0°W,† near the crater Murchison. Although the year is not stated for the 6.0 m observations, the leading edge data were apparently collected on 14 November 1964 [Klemperer, 1965], which would put the subradar point slightly to the west of that for the 11.3 m results. The approximate coordinates for the 6.0 m case are 6.5°N 6.5°W, which is a relatively smooth area between the Sinus Medii and the Sinus Aestuum. On the other hand, the leading edge results for the 68 cm data are based on observations made on 6 December 1961 and 26 January 1962 [Evans and Pettengill, 1963] for which the subradar points were 6.6°S 5.3°W and

† These values are of the Earth's Selenographic coordinates at 0^h Universal Time obtained from The American Ephemeris and Nautical Almanac, and are sufficiently accurate for this study.

4.8°S 3.5°W, which is the rough area near the subradar point for our 24 August 1965 run (5.0°S 1.5°W). (There is a discrepancy in the Evans and Pettengill report between the date reported in the text and that in Fig. 8, where the dates 7 December and 25 January are given; the text dates are used here, but since the subradar point does not move an important amount from day to day and accurate computations of the subradar point have not been considered necessary, it makes no difference here.) Although different pulse lengths (30 and 12 μs, respectively) were used on those two days, the results were apparently the same. The 23 cm curve is based on observations made on 26 February 1965 [Evans and Hagfors, 1966] for which the location of the subradar point was about 2.0°N 1.4°E in the Sinus Medii.

Thus the 6.0 m, the 11.3 m, and our 20 August results for both wavelengths, all of which closely agree, have subradar points in generally the same area. Similarly, the 68 cm and our 24 August results, which also closely agree, have subradar points very near each other. The disposition of the various subradar points is shown in Fig. 47. While the 20 August subradar point is not really very close to the 11.3 and 6.0 m subradar points, the terrains are somewhat similar, and the comparison of these results is probably valid. Indeed, it is likely that our results would show an even higher peak if the 20 August subradar point had been closer to that of the others because our equivalent pulse length was shorter.

The difference in the echo power at the peak due to different resolutions for the 24 August run is seen from Figs. 39 and 40 to be about 3 dB. This difference would be greater for the 20 August results since the peak is somewhat sharper. Therefore there is more than 3 dB extra difference between the 20 August results and the 6.0 and 11.3 m results. Part of this difference is probably due to the fact that the subradar points were not really very close. Differences in the topography or the local reflection coefficients could easily account for this discrepancy, but this possibility would have to be tested experimentally. The discrepancy may also be due to measurement errors. At the leading edge, the estimated error limit for the 6.0 m results is ±2 dB. The 11.3 m

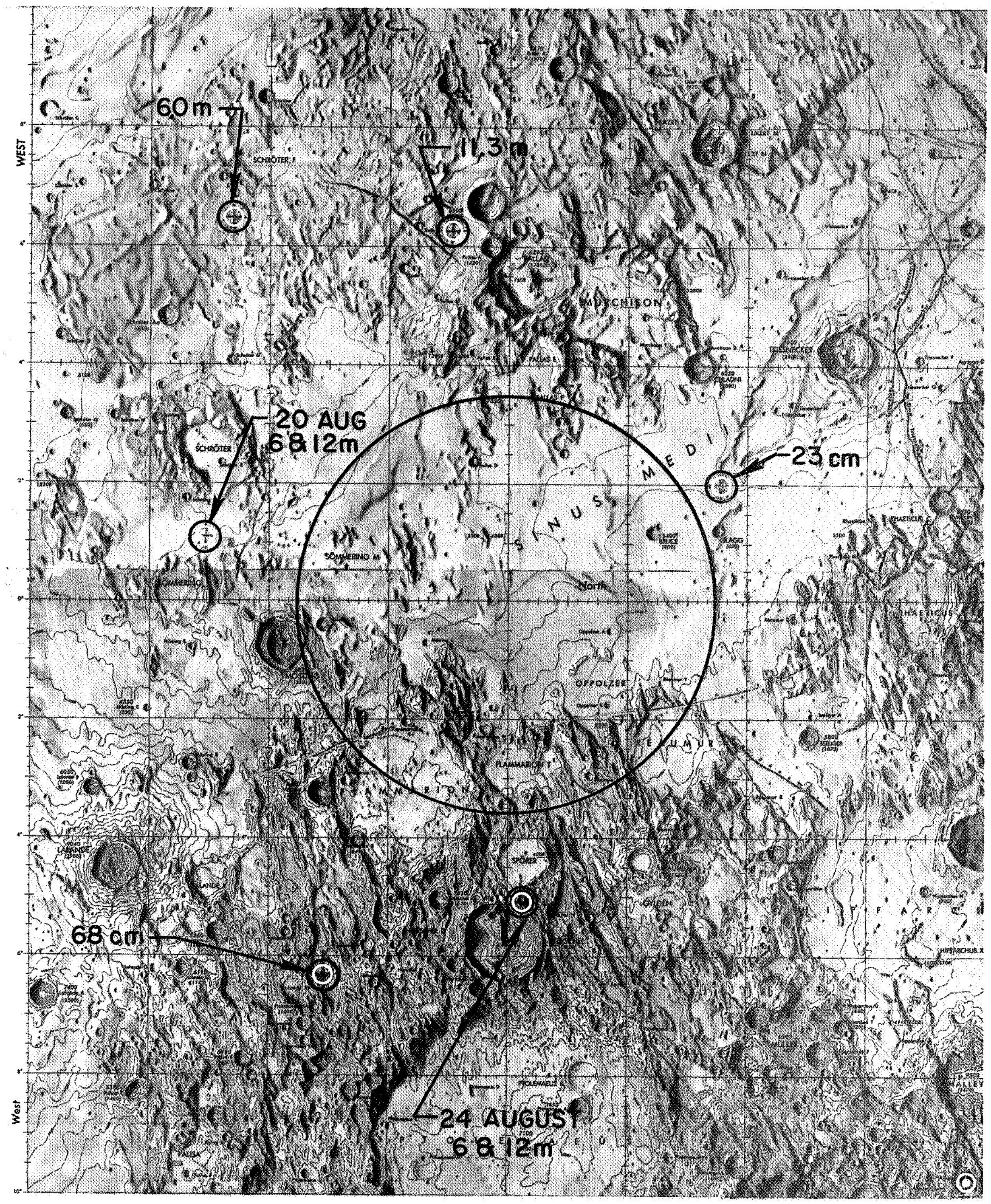

Fig. 47. THE POSITIONS OF THE SUBRADAR POINTS FOR THE VARIOUS OBSERVATIONS. The large circle at the origin encloses the first 20 μs range interval for a perfectly spherical moon.

results also have a ±2 dB error limit. The results are better than that, having an estimated error limit of ±1.5 dB. Even though it is possible to explain this final amount of discrepancy from error considerations, it is felt here that it is actually due to different reflecting properties at the various subradar points.

The conclusion drawn from this evidence is that the quasi-specular scattering properties of the moon are nearly independent of wavelength except possibly for a factor affecting all ranges equally for wavelengths greater than 23 cm. In Fig. 48 the curves of Fig. 46 have been normalized at a delay of 1 ms and replotted. The similarity between the 23 cm and 68 cm quasi-specular components has already been noted [Evans and Hagfors, 1966]. This comparison was based on 10 μs pulse length observations whose subradar points were very near one another (2.2°S 2.6°W at 23 cm and 4.8°S

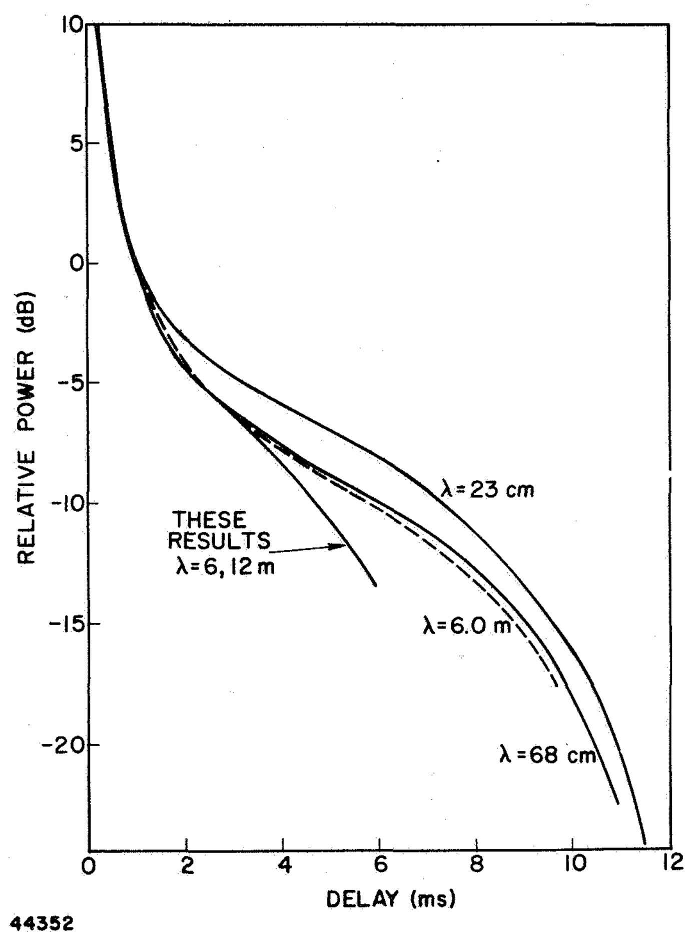

Fig. 48. THE RESULTS SHOWN IN FIG. 46 NORMALIZED TO THEIR VALUES AT A DELAY OF 1 MS.

3.5°W at 68 cm). The 3.6, 23, and 68 cm quasi-specular component obtained by subtracting the diffuse component from the echoes is plotted in Fig. 49 along with the $P_E - P_D$ 6 and 12 m estimates from 24 August. The remarkable agreement between these curves proves that the shape of quasi-specular scattering is nearly independent of the wavelength above 23 cm for delays up to 1 ms. The agreement between the 68 cm and 6.0 m results shown in Fig. 48 indicates that this is true over the entire range interval and that the relative amount of diffuse component is also nearly the same, at least over that smaller wavelength interval. It should be made clear that the data presented in these figures are relative and that there may be considerable difference in the radar cross section per unit surface area, σ, to which the echo power vs delay data are proportional.

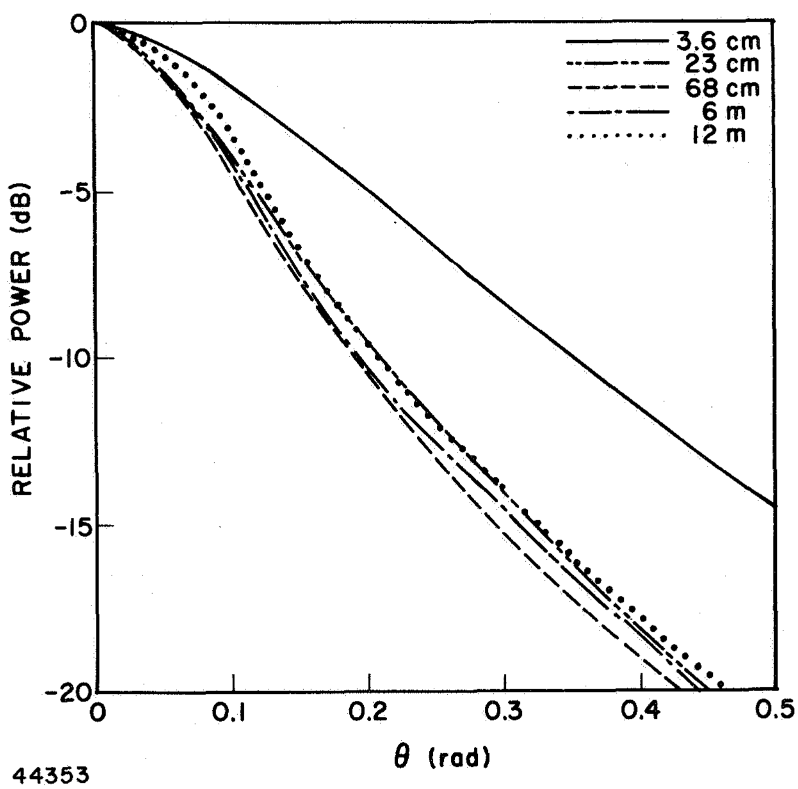

Fig. 49. THE QUASI-SPECULAR ECHO COMPONENTS FOR SEVERAL WAVELENGTHS NORMALIZED AT A ZERO DELAY AS A FUNCTION OF THE ANGLE OF INCIDENCE θ. There is no significant difference over the range of wavelengths from 23 cm to 12 m.

Only at 23 cm has the total radar cross section been measured accurately [Evans and Hagfors, 1966]. If the total cross section is assumed to be constant (there is considerable evidence for this), the quasi-specular component of σ is found to have a fairly strong wavelength dependence over the range of 3.8 to 68 cm [Hagfors, 1967]. This quantity was computed from the expression

$$\sigma = \frac{aRP(\tau)}{c\int P(\tau)\, d\tau}$$

where the measured total radar cross section, σ_o, is a fraction R of the moon's geometrical cross section, c is the velocity of light, a is the radius of the moon, and $P(\tau)$ is the received power vs delay. If a composite 6 m power vs delay curve is formed by using our 24 August results for the 0 to 1 ms delay interval and Klemperer's results over the rest of the range depth, it very closely matches the 68 cm curve everywhere. This is a particularly valid comparison because the resolutions at the leading edge are equivalent and because circular polarization was used for both the 68 cm and Klemperer's 6.0 m work. (The diffuse, expected component of the echoes may be sensitive to the incident polarization, while the quasi-specular response is equal for all polarizations.) Thus, if the total cross section is independent of wavelength below 68 cm, there will be no general shift between the curves and σ will be independent of the wavelength.

The measured values of σ_o are presented in Fig. 50. Except for the three longest wavelength measurements, the total cross section is nearly constant. Those three measurements were made with the same equipment used to obtain the 11.3 m echo power vs delay curve [Davis and Rohlfs, 1964]. Since the position of the subradar point basically only affects the value of P(0), the value of σ_o is not appreciably changed by different subradar points, so the high values are not due to this effect. Although σ_o appears to increase at the lower wavelengths, this conclusion cannot be drawn because the error limits are so large.

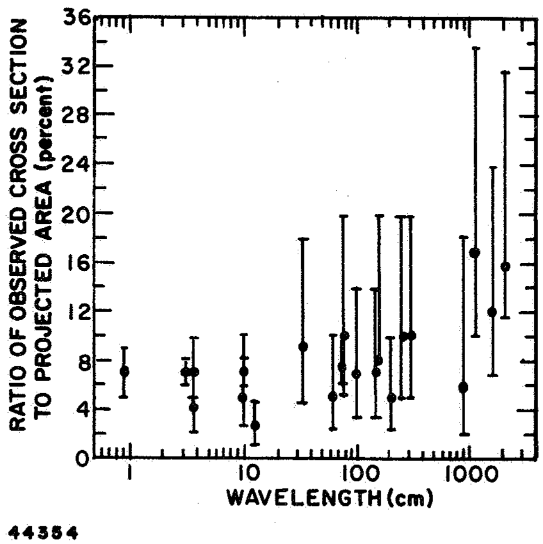

Fig. 50. THE REPORTED VALUES OF THE TOTAL RADAR CROSS SECTION OF THE MOON VS WAVELENGTH. [From Evans and Hagfors, 1966.]

The total radar cross section could not be measured from the echoes obtained here because no calibration of the absolute echo intensity was made during the runs. In principle, the echoes could be compared to the background noise level since the sky temperature is known; but other sources of noise, particularly from interference, make this scheme impossible. Attempts to make this comparison resulted in values for σ_o that were considerably less than any of the other measurements, particularly at 6 m.

There is general agreement about the interpretation of the echoes for the nearer ranges where the angle of incidence is small, but the nature of the scattering at the greater angles of incidence has not been explained theoretically. At the smaller angles of incidence the echoes predominantly come from nearly flat regions which are normal to the incident radiation, and it has been argued that the entire power vs delay curve can be explained by this mechanism if shadowing is accounted for [Beckmann, 1965a]. The depolarized component of the echoes has also been explained by scattering from smooth surfaces whose normals are not aligned with the direction of the incident radiation. The other view [Hagfors, 1967; Hagfors, 1964] is that the backscattering from the more distant regions is from the small scale structure, having dimensions comparable to the wavelength.

The general problem of the scattering of electromagnetic waves from random rough surfaces has not been solved. Only for the case of a perfectly conducting smoothly undulating surface (whose local radius of curvature is much larger than the wavelength) have any results been obtained. In applying these to the interpretation of moon echoes, the assumption is made that the scattering behavior is the same as for the perfect conductivity case except that the returned power is reduced proportionally by the normal incidence reflection coefficient of the dielectric.

Using the Helmholtz integral approach and essentially making the above approximations [Beckmann and Spizzichino, 1963], Hagfors [1964] showed that for a zero mean gaussian random surface of rms height fluctuations h_o and an exponential autocorrelation function governing adjacent height deviations, the backscattered power vs angle characteristic is

$$P(\theta) \propto [\cos^4(\theta) + C_o \sin^2(\theta)]^{-3/2} \tag{5.1}$$

Later it was shown that the same result could be obtained from geometric optics if the surface introduces a deep phase modulation on the incident wave [Hagfors, 1966]. A similar result was obtained by Beckmann [1965a] for a composite surface of independent stationary gaussian height deviations, each with its own standard deviation and exponential correlation function. Ignoring the multiplicative shadowing function, his result is

$$P(\theta) = \frac{P_s \lambda^2 C}{8\pi A} [\cos^4(\theta) + C \sin^2(\theta)]^{-3/2} \tag{5.2}$$

where P_s is the power backscattered at normal incidence by a smooth surface of equal area A at the same distance, λ is the wavelength, and C is given by

$$C = \lambda^2 \left[4\pi \sum_j (h_j^2/d_j) \right]^{-2} \tag{5.3}$$

Here, h_j is the rms height deviation and d_j the correlation distance (at which the autocorrelation function falls to e^{-1}) for the j^{th} component of the surface. The parameter C_o is given by Eq. (5.3) when only the first term in the summation is included. With the inclusion of the shadowing term, Eq. (5.2) can be made to closely fit the observed results by adjusting the parameter C and a shadowing parameter. It has not yet been possible to interpret the measured values of $C(\lambda)$ in terms of the h's and the d's.

For the quasi-specular component, the values for C that match the experimental results are $C = 30$ at $\lambda = 3.6$ cm, $C = 95$ at $\lambda = 23$ cm, and $C = 100$ at $\lambda = 68$ cm. Our results indicate that a value for C of about 100 is correct for $\lambda = 6$ m and $\lambda = 12$ m as well. Since these values are obtained from the shape of the curves, and noting that P_s varies as λ^{-2} [Beckmann, 1965a,b], Eq. (5.2) predicts that the backscattered power will be independent of wavelength. Therefore, the constancy of the parameter C with wavelength in this generally accepted, rather simplified model leads to the conclusion that the total radar cross section, which is proportional to the integral of Eq. (5.2), is a constant independent of wavelength, for which there is strong evidence.

The wavelength independence of C is certainly not in agreement with Eq. (5.3). Because of the rms slope for each component is $s_j = h_j/d_j$, Eq. (5.3) can be written as

$$C = \lambda^2 \left[4\pi \sum_j (s_j^2 \; d_j) \right]^{-2}$$

The observed values of the parameter C do not have the proper wavelength dependence. Beckmann [1965a] has argued that as the wavelength becomes shorter, more terms in the summation will come into play since smaller structure with greater slopes will contribute to the quasi-specular scattering. This is contrary to our observation that C is independent of wavelength, since the summation would have to become larger with increasing wavelength.

Although the choice of an exponential surface autocorrelation function yields a $P(\theta)$ which matches the observations, it is interesting to consider the result of using an analytic autocorrelation function. (One of the objections to the exponential autocorrelation function is that it has an unphysical discontinuous derivative even though it closely matches the measured terrestrial function.) For the composite surface, Beckmann [1965b], gives instead of Eq. (5.2), for any analytic autocorrelation function,

$$P(\theta) = \frac{P_s \lambda^2 Q}{4\pi A} \exp(-Q \tan^2\theta) \cos^{-4} \theta \qquad (5.4)$$

where

$$Q = 2 \sum_j s_j^2 = 4 \sum_j (h_j/d_j)^2$$

Hagfors [1964] presents the same expression, but limits its applicability to gaussian autocorrelation functions and incorporates only the first term in the summation. Although it has been shown that Eq. (5.4) does not fit the observations nearly as well as does Eq. (5.2) [Evans, 1965], the multiplicative factor Q is independent of wavelength.

For this second model of the surface the total cross section and the shape of $P(\theta)$ will be independent of wavelength. This is in contrast to the prediction of the exponential autocorrelation function model which matches the shape better. For the first model the shape does vary with wavelength, although σ_o will remain constant [Fjeldbo, 1964]. Experimentally, the shape is seen to be constant for wavelengths greater than 23 cm (Fig. 49), but σ_o may be increasing with wavelength (Fig. 50).

More accurate values for σ_o, particularly at decameter wavelengths, are needed to fully understand the scattering in terms of the surface parameters.

These contradictions indicate that even the quasi-specular backscatter from the moon is not sufficiently explained. It appears that more complicated types of surfaces will be needed to explain the results. Some work has already been reported in the area of surface statistics [Marcus, 1967] and in multilayered surfaces [Ward and Jiracek, 1968; Hagfors, 1967]. Also, more general solutions to the rough surface scattering problem are needed.

An extension [Beckmann, 1968] to the vector analog of the Helmholtz-Kirchhoff theory has resulted in some theoretical predictions about the depolarization of the incident radiation. It is shown, for a finitely conducting or dielectric surface, that even a gently undulating surface can cause depolarization. The surface elements whose normals are parallel to the direction of the incident waves do not contribute to the depolarization, but the other elements do. The former elements are those that contribute to the quasi-specular component and that are included in any application of the method of stationary phase or geometric optics. Thus Eqs. (5.2) and (5.4) are accurate expressions, assuming their respective surface statistics, for the quasi-specular component. Unfortunately, it is impossible to isolate this component from the echoes although attempts using various criteria have been made. Beckmann predicts the ratio of the linear depolarized to expected components of the echoes in terms of the dielectric constant and the rms surface slopes. The 23 cm data was found to correspond to values of $\epsilon \approx 2$ and $s \approx 15°$.

Our results, however, do not agree very closely with those at 23 cm. Our measured ratio at 12 m (Fig. 43) has the same range variation but is about twice as high as the 23 cm ratio. This measurement, it should be pointed out, does not suffer as badly from frequency response difficulties as the estimation of the depolarized component alone does, because part of the response factor divides out; there is always the response asymmetry problem which distorts the background noise subtraction. The difference in the ratio moves the curve in the direction of a lower dielectric constant and/or a higher rms slope. Since these changes are unlikely with increasing wavelength, it is apparent that the depolarization is not entirely explained by the smooth structure, but that the small scale structure contributes a considerable part of the depolarization.

The fact that the 68 cm and 6 m expected power vs delay curves closely coincide over the entire range depth of the moon, however, indicates that the scattering at high incidence angles is also independent of the wavelength. This supports the idea that the scattering is mainly quasi-specular at all ranges. Since scattering from smooth areas cannot account for the increase of the depolarized to expected component ratio at larger wavelengths, the small scale structure must be included in any explanation of the observations.

D. Conclusion and Suggestions for Further Study

The analysis of radar echoes from the moon has been described in this work. Particular attention has been devoted to possible and actual sources of error and distortions of the signals. The effect of ionospheric Faraday rotation was found to be of prime significance, and was eventually used to separate the polarized echo components. Thus, accurate measurements of the backscattering behavior were made at considerably greater resolution than was previously obtainable, although sensitivity limitations did not allow a measurement of the scattering properties over the moon's entire range depth.

The most important conclusion reached was that the scattering properties of the moon are only slightly, if at all, wavelength-dependent below 68 cm. The erroneous wavelength dependence attributed previously to the echoes was shown to be due to an extreme sensitivity to the position of the subradar point. It was further noted that there are insufficient theoretical results to properly explain the observed behavior. More work needs to be done in this area.

Because of the considerable computing effort required, only a comparatively small amount of the available data has been reduced. This work should be continued both to improve the quality of the low resolution data and to investigate the influence of the subradar point on the echoes. Only two of the four or five resolvable positions have been looked at so far. One interesting possibility is the effect of the age of the surface at various locations. At the easternmost positions that the subradar point may attain, the age of the surface is thought to be very great compared to the other areas near the moon's nose. Presumably the reflections from that region will be relatively weak because the surface will be more churned up by the continuous meteor bombardment from space, which lowers its dielectric constant.

Measurements hould also be made of the effect of the subradar point at other wavelengths. It is also very important to make accurate measurements of the total lunar cross section, which is best done by comparing the lunar echoes to those from an object of accurately known cross section. This has already been done at 23 cm with an artificial spherical satellite of 1 m^2 cross section [Evans and Hagfors, 1966]. A much larger one would be needed for adequate sensitivity at long wavelengths, of course; a synchronous orbit would also be desirable to eliminate tracking problems.

Investigation of some of these questions has already begun. It is planned to analyze data collected on other days to make a complete determination of the effect of the subradar point on the echoes. An attempt to increase the range interval over which accurate results can be obtained from our data is also planned.

PRECEDING PAGE BLANK NOT FILMED.

APPENDIX A

POWER SPECTRAL ESTIMATION

The power spectral estimation using the periodogram is considered here when the signal to be estimated is composed of two correlated signals with different modulating functions. For simplicity, this will be done for continuous signals only; however, the analysis will also be made for the sampled data case for a single signal, which leads to Eq. (2.15).

Let $x(t)$ and $y(t)$ be the two parts of the signal $z(t)$. Each will have its own weighting function, $u(t)$ and $v(t)$, respectively, composed of the product of their modulating functions and the imposed data window. Thus the periodogram is made from

$$z'(t) = u(t)\ x(t) + v(t)\ y(t)$$

The periodogram is

$$P = \frac{1}{T} \left| Z'(f) \right|^2 = \frac{1}{T} Z'(f)\ Z'^*(f)$$

$$= \frac{1}{T} \left\{ \int_{-\infty}^{\infty} [U(f')\ X(f-f') + V(f')\ Y(f-f')]\ df' \right\}$$

$$\times \left\{ \int_{-\infty}^{\infty} [U(f'')\ X(f-f'') + V(f'')\ Y(f-f'')]\ df'' \right\} \tag{A.1}$$

where T is the duration of the signal. So,

$$P = \frac{1}{T} \left\{ \int_{-\infty}^{\infty} u(\sigma)\ x(\sigma)\ e^{-j\omega\sigma}\ d\sigma + \int_{-\infty}^{\infty} v(\xi)\ y(\xi)\ e^{-j\omega\xi}\ d\xi \right\}$$

$$\times \left\{ \int_{-\infty}^{\infty} u(\rho)\ x(\rho)\ e^{j\omega\rho}\ d\rho + \int_{-\infty}^{\infty} v(\zeta)\ y(\zeta)\ e^{j\omega\zeta}\ d\zeta \right\}$$

$$= \frac{1}{T}\left\{\iint_{-\infty}^{\infty} u(\sigma)\ u(\rho)\ x(\sigma)\ x(\rho)\ e^{-j\omega(\sigma-\rho)}\ d\rho\ d\sigma\right.$$

$$+ \iint_{-\infty}^{\infty} v(\xi)\ v(\zeta)\ y(\xi)\ y(\zeta)\ e^{-j\omega(\xi-\zeta)}\ d\zeta\ d\xi$$

$$+ \iint_{-\infty}^{\infty} u(\sigma)\ v(\zeta)\ x(\sigma)\ y(\zeta)\ e^{-j\omega(\sigma-\zeta)}\ d\zeta\ d\sigma$$

$$\left. + \iint_{-\infty}^{\infty} u(\rho)\ v(\xi)\ x(\rho)\ y(\xi)\ e^{-j\omega(\xi-\rho)}\ d\rho\ d\xi\right\}$$

The mean value of the estimate P is

$$\overline{P} = \frac{1}{T}\iint_{-\infty}^{\infty} u(\rho)\ u(\rho+\tau)\ R_x(\tau)\ e^{-j\omega\tau}\ d\tau\ d\rho$$

$$+ \frac{1}{T}\iint_{-\infty}^{\infty} v(\zeta)\ v(\zeta+\tau)\ R_y(\tau)\ e^{-j\omega\tau}\ d\tau\ d\zeta$$

$$+ \frac{1}{T}\iint_{-\infty}^{\infty} v(\zeta)\ u(\zeta+\tau)\ R_{xy}(-\tau)\ e^{-j\omega\tau}\ d\tau\ d\zeta$$

$$+ \frac{1}{T}\iint_{-\infty}^{\infty} u(\rho)\ v(\rho+\tau)\ R_{xy}(\tau)\ e^{-j\omega\tau}\ d\tau\ d\rho \qquad \text{(A.2)}$$

where

$$R_x = \overline{x(t)\ x(t+\tau)}$$

$$R_y = \overline{y(t)\ y(t+\tau)}$$

$$R_{xy} = \overline{x(t)\ y(t+\tau)}$$

The first two terms are the response to x and y separately, and each leads to the continuous signal equivalent of Eq. (2.15) when transformed back to the frequency domain. The last two terms represent the response to the cospectrum of x and y. Inasmuch as all four terms transform to the frequency domain in the same way, we will perform the computation only for the first term.

First, performing the integration with respect to τ:

$$\int_{-\infty}^{\infty} u(\rho+\tau)\, R_x(\tau)\, e^{-j\omega\tau}\, d\tau$$

$$= \iint_{\infty}^{\infty} U(f'')\, e^{j\omega''(\rho+\tau)}\, df'' \int_{-\infty}^{\infty} \Phi_x(f'')\, e^{j\omega'\tau}\, df'\, e^{-j\omega\tau}\, d\tau$$

$$= e^{j\omega''\rho} \int_{-\infty}^{\infty} U(f'')\, \Phi_x(f-f'')df''$$

where $\Phi_x(f)$ is the power spectral density of x. Then the first term becomes

$$\overline{P}_1(f) = \frac{1}{T} \int_{-\infty}^{\infty} u(\rho)\, e^{j\omega''\rho} \int_{-\infty}^{\infty} U(f'')\, \Phi_x(f-f'')\, df''\, d\rho$$

$$= \frac{1}{T} \int_{-\infty}^{\infty} |U(f'')|^2\, \Phi_x(f-f'')\, df'' \qquad (A.3)$$

Thus (A.2) becomes

$$\overline{P}(f) = \frac{1}{T} \int_{-\infty}^{\infty} |U(f')|^2\, \Phi_x(f-f')\, df'$$

$$+ \frac{1}{T} \int_{-\infty}^{\infty} |V(f')|^2\, \Phi_y(f-f')\, df'$$

$$+ \frac{1}{T} \int_{-\infty}^{\infty} U(f') \; V^*(f') \; \Phi^*_{xy}(f-f') \; df'$$

$$+ \frac{1}{T} \int_{-\infty}^{\infty} U^*(f') \; V(f') \; \Phi_{xy}(f-f') \; df'$$

where $\Phi_{xy}(f) = \mathfrak{F}\{R_{xy}(\tau)\}$.

Combining the last two terms, and noting that Φ_x and Φ_y are even functions, we get

$$\overline{P}(f) = \frac{1}{T} \int_{-\infty}^{\infty} |U(f')|^2 \; \Phi_x(f'-f) \; df' + \frac{1}{T} \int_{-\infty}^{\infty} |V(f')|^2 \; \Phi_y(f'-f) \; df'$$

$$+ \frac{1}{T} \int_{-\infty}^{\infty} 2 \, \mathrm{Re}\Big[U(f') \; V^*(f') \; \Phi_{xy}(f'-f)\Big] \; df' \qquad (A.4)$$

If x and y are uncorrelated, then $\Phi_{xy}(f) = 0$ and the last term disappears. If they are completely correlated but have different amplitudes,

$$\Phi_{xy} = \Phi_x \Phi_y = a\Phi_x^2$$

where a is the amplitude ratio and is real, so the spectral window for the third term becomes

$$\frac{2}{T} \mathrm{Re}[U(f) \; V^*(f)]$$

When sampled data rather than continuous data is used, the situation is only slightly different. We noted that each term in (A.2) behaves the same way so let's just consider one such term now. Further, suppose that the pediodogram is formed from the finite Fourier transform of the modified data, which is aliased. Then

$$Z_p(n\Delta f) = \frac{1}{T} \sum_{\ell=-\infty}^{\infty} Z(n\Delta f + \ell F)$$

and instead of (A.1) we have

$$P_p(n\Delta f) = T\left| Z_p(n\Delta f)\right|^2 = T\left|\frac{1}{T} \sum_{\ell=-\infty}^{\infty} Z(n\Delta f + \ell F\right|^2 .$$

Since only one term is being included, $z(t) = u(t)\ x(t)$. The mean value of the estimate is

$$\overline{P_p}(n\Delta f) = \frac{1}{T}\overline{\left| Z_p(n\Delta f\right|^2}$$

$$= \frac{1}{T} \sum_{\ell=-\infty}^{\infty} \sum_{m=-\infty}^{\infty} \overline{Z(n\Delta f) + \ell F)\ Z^*(n\Delta f + mF)} \qquad \text{(A.5)}$$

Each term in this summation is similar to (A.3):

$$\overline{Z(n\Delta f + \ell F)\ Z^*(n\Delta f + mF)} = \int_{-\infty}^{\infty} \overline{U(f'')\ U[f'' - (\ell - m)F]\ \Phi(f + \ell F - f'')\ df''}$$

So (A.5) becomes

$$\overline{P_p}(n\Delta f) = \int_{-\infty}^{\infty} \left[\frac{1}{T} \sum_{\ell=-\infty}^{\infty} \sum_{m=-\infty}^{\infty} U(f' + \ell F)\ U(f' + mF)\right] \Phi(n\Delta f - f')\ df'$$

and the bracketed term is recognized as

$$\frac{1}{T}\left| \sum_{\ell=-\infty}^{\infty} U(f' + \ell F)\right|^2 = \frac{1}{T}\left| U_p(f')\right|^2$$

which is the aliased spectral window. Then

$$\overline{P_p}(n\Delta f) = \int_{-\infty}^{\infty} \frac{1}{T}\left| U_p(f') \right|^2 \Phi(n\Delta f - f')\ df'$$

The inclusion of the normalizing constant yields Eq. (2.15).

BIBLIOGRAPHY

Bay, Z., Hung. Phys. Acta, 1, 1946, p. 1.

Beckmann, P., "Radar Backscatter from the Surface of the Moon," J. Geophys. Res., 70, 10, 1965a, pp. 2345-2350.

Beckmann, P., "Scattering by Composite Rough Surfaces," Proc. IEEE, 53, 1965b, pp. 1012-1015.

Beckmann, P., "Depolarization of Electromagnetic Waves Backscattered from the Lunar Surface," J. Geophys. Res., 73, 2, 1968, pp. 649-656.

Berkowitz, Raymond S. (ed.), Modern Radar, John Wiley & Sons, New York, 1965.

Blackman, R. B., and J. W. Tukey, The Measurement of Power Spectra, Dover Publications, New York, 1958.

Browne, I. C., et al, "Radar Echoes from the Moon," Proc. Phys. Soc. London, B69, 1956, pp. 901-920.

Cooley, J. W., P. A. W. Lewis, and P. D. Welch, "Application of the East Fourier Transform to Computation of Fourier Integrals," Fourier Series and Convolution Integrals, Trans. IEEE on Audio and Electroacoustics, AU-15, 2, 1967, pp. 79-84.

Davis, J. R., and D. C. Rohlfs, "Lunar Radio-Reflection Properties at Decameter Wavelengths," J. Geophys. Res., 69, 15, 1964, pp. 3257-3262.

Davis, J. R., et al, "Decameter-Wave Radar Studies of the Lunar Surface," Radio Science, 69D, 1, Dec 1965, pp. 1659-1669.

De Witt, J. H., Jr., and E. K. Stodola, "Detection of Radio Signals Reflected from the Moon," Proc. IRE, 37, 1949, pp. 229-242.

Eshleman, V. R., "Radar Astronomy," Science, 158, 1967, pp. 585-597.

Eshleman, V. R., A. B. Gallagher, and R. C. Barthle, "Radar Methods of Measuring the Cislunar Electron Density," J. Geophys. Res., 65, 10, 1960, pp. 3079-3086.

Evans, J. V., "The Electron Content of the Ionosphere," J. Atmos. Terr. Phys., 11, 1957, pp. 259-271.

Evans, J. V., "Radio Echo Studies of the Moon," Physics and Astronomy of the Moon, Z. Kopal (ed.), Chapter 12, Academic Press, London, 1962.

Evans, J. V., "Radar Studies of the Moon," Radio Science, J. NBS, 69D, 1965, pp. 1637-1659.

Evans, J. V., and T. Hagfors, "Study of Radio Echoes from the Moon at 23 Centimeters Wavelength," J. Geophys. Res., 71, 20, 1966, pp. 4871-4889.

Evans, J. V., and G. H. Pettengill, "The Scattering Properties of the Lunar Surface at Radio Wavelengths," The Solar System, Vol. 4, "The Moon Meteorites and Comets," G. P. Kuiper and B. M. Middlehurst (eds.), Chapter 5, University of Chicago Press, 1963.

Fenwick, R. B., and G. H. Barry, "HF Measurements Using Extended Chirp-Radar Techniques," Rept. SEL-65-058, TR No. 103, Contract Nonr-225(64), Stanford Electronics Laboratories, Stanford, Calif., Jun 1965.

Fjeldbo, G., "Bistatic-Radar Methods for Studying Planetary Ionospheres and Surfaces," Final Rept., NSF Grant NSF G-21543 and Scientific Rept. No. 2, NASA Grant NsG-377, Stanford Electronics Laboratories, Stanford, Calif., Apr 1964.

Garriott, O. K., "The Determination of Ionospheric Electron Content and Distribution from Satellite Observations, Part 2: Results of the Analysis," J. Geophys. Res., 65, 1960, pp. 1151-1157.

Hagfors, T., "Some Properties of Radio Waves Reflected from the Moon and Their Relation to the Lunar Surface," J. Geophys. Res., 66, 3, 1961, pp. 777-785.

Hagfors, T., "Backscattering from an Undulating Surface with Applications to Radar Returns from the Moon," J. Geophys. Res., 69, 18, 1964, pp. 3779-3783.

Hagfors, T., "Relationship of Geometric Optics and Autocorrelation Approaches to the Analysis of Lunar and Planetary Radar," J. Geophys. Res., 71, 2, 1966, pp. 379-383.

Hagfors, T., "A Study of the Depolarization of Lunar Radar Echoes," Radio Science, 2, 5 (New Series), 1967, pp. 445-465.

Helstrom, Carl W., Statistical Theory of Signal Detection, Pergamon Press, New York, 1960.

Howard, H. T., "An Antenna Array for Radar Astronomy Studies in the 20 to 50 Mc Range," Trans. IEEE, AP-13, 3, 1965, pp. 365-368.

Howard, H. T., "Cislunar Electron Content as Determined by Radar Group Delay Measurements," Rept. SEL-66-113, Scientific Rept. No. 17, NASA Grant NsG-377, Nov 1966. Also in J. Geophys. Res., 72, 11, 1967, pp. 2729-2735.

Howard, H. T., et al, "Radar Measurements of the Cislunar Electron Content," J. Geophys. Res., 70, 1965, pp. 4357-4363.

Hughes, V. A., "Radio Wave Scattering from the Lunar Surface," Proc. Phys. Soc. London, 78, 1961, pp. 988-997.

Kerr, F. J., and C. A. Shain, "Moon Echoes and Transmission through the Ionosphere," Proc. IRE, 39, 1951, pp. 230-242.

Kerr, F. J., C. A. Shain, and C. S. Higgins, "Moon Echoes and Penetration in the Ionosphere," Nature, 163, 1949, pp. 310-313.

Klemperer, W. K., "Angular Scattering Law for the Moon at 6-Meter Wave-Length," J. Geophys. Res., 70, 15, 1965, pp. 3798-3800.

Lawrence, R. S., C. G. Little, and H. J. A. Chivers, "A Survey of Ionospheric Effects upon Earth-Space Radio Propagation," Proc. IEEE, Jan 1964, pp. 4-27.

Lynn, V. L., M. D. Sohigian, and E. A. Crocker, "Radar Observations of the Moon at a Wavelength of 8.6 Millimeters," J. Geophys. Res., 69, 4, 1964, pp. 781-783.

Marcus, A. H., "Statistical Model of a Flooded Random Surface and Applications to Lunar Terrain," J. Geophys. Res., 72, 6, 1967, pp. 1721-1726.

Millman, G. H., "Radar-Lunar Measurements of the Electron Content of the Ionosphere," J. Geophys. Res., 69, 3, 1964, pp. 429-440.

Mlodnosky, R. F., and R. A. Helliwell, "Graphic Data on the Earth's Main Magnetic Field in Space," J. Geophys. Res., 67, 6, 1962, pp. 2207-2214.

Murray, W. A. S., and J. K. Hargreaves, "Lunar Radio Echoes and the Faraday Effect in the Ionosphere," Nature, 173, 1954, p. 944.

Pettengill, G. H., "Measurements of Lunar Reflectivity Using the Millstone Radar," Proc. IRE, 46, 1960, pp. 286-292.

Ratcliffe, J. A., The Magneto-ionic Theory and Its Applications to the Ionosphere, Cambridge University Press, Cambridge, England, 1959.

Ruffine, R. S., "On the Time Average Radar Cross Section of the Moon," J. Geophys. Res., 72, 16, 1967, pp. 4073-4096.

Thompson, T. W., and R. B. Dyce, "Mapping of Lunar Radar Reflectivity at 70 Centimeters," J. Geophys. Res., 71, 20, 1966, pp. 4843-4853.

Trexler, J. H., "Lunar Radio Echoes," Proc. IRE, 46, 1958, pp. 286-292.

Tyler, G. L., "Bistatic-Radar Imaging and Measurement Techniques for the Study of Planetary Surfaces," Rept. SEL-67-042, Scientific Rept. No. 19, NASA Grant NsG-377, Stanford Electronics Laboratories, Stanford, Calif., May 1967.

Ward, S. H., and G. R. Jiracek, "Electromagnetic Reflection from a Plane-Layered Lunar Model," J. Geophys. Res., 73, 4, 1967, pp. 1355-1372.

Welch, P. D., "The Use of Fast Fourier Transform for the Estimation of Power Spectra: A Method Based on Time Averaging over Short, Modified Periodograms," Trans. IEEE on Audio and Electroacoustics, AU-15, 2, 1967, pp. 70-73.

Yoh, P., "Radar Studies of the Cislunar Medium," Rept. SEL-65-091, Scientific Rept. No. 12, NASA Grant NsG-377, Stanford Electronics Laboratories, Stanford, Calif., Dec 1965.

Yoh, P., et al, "Lunar Radar Measurements of the Earth's Magnetospheric Wake," J. Geophys. Res., 71, 1, 1966, pp. 189-193.